2017

Modeling of Two & Three Phases Bubble Column

Modélisation d'une Colonne à bulles Biphasique et Triphasique

ALIZEB HUSSAIN SYED

UDES | 2500 boul. de l'Université, Sherbrooke, J1K 2R1, Québec, Canada.

Université de Sherbrooke
Faculté de Génie
Département de Génie Chimique et de Génie Biotechnologique

Modélisation d'une Colonne à bulles Biphasique et Triphasique

Modeling of Two & Three Phases Bubble Column

PHD THÉSÉ

Directeur de Thése: Jean-Michel Lavoie

October 2017

Alizeb Hussain Syed
Sherbrooke, Québec, Canada.

RÉSUMÉ

Le partenaire industriel de ce projet utilise un réacteur à suspension à trois phases pour la production de méthanol biogénique. Dans celui-ci, le gaz de synthèse est diffusé par barbotement dans la phase à suspension qui contient à la fois les phases liquide et solide. Les bulles en ascension présentent un large spectre de tailles et interagissent avec la phase à suspension en échangeant de la quantité de mouvement via leurs surfaces. Cet échange comprend les forces de trainé, de portance, de lubrification en proche parois et de dispersion par turbulence; lesquelles requièrent notamment le calcul de la taille moyenne des bulles. Une façon de prédire numériquement cette taille moyenne est de recourir à un modèle de bilan de population (PBM, de l'anglais Population Balance Model), qui peut être couplé avec un model multiphasique eulérien. Un tel PBM a requière des modèles de fermetures pour la coalescence et la rupture des bulles.

Dans la présente étude, l'influence des modèles noyaux de coalescence et de rupture des bulles a été étudiée pour des systèmes à deux et à trois phases en utilisant l'approche eulérienne. L'influence de la taille du maillage, du nombre de classes de bulles, du schéma numérique, de la force de lubrification en proche parois et de la force de dispersion par turbulence sont également incluses. Dans un système bi-phasique, les résultats montrent que le modèle de coalescence Luo doit être ajusté lorsqu'il est utilisé en combinaison avec le noyau de rupture Luo. La combinaison des noyaux de coalescence Luo et de rupture Lehr (Luo-Lehr) montrent des profils radiaux moyennés dans le temps qui sont valides pour la concentration de gaz et la vitesse axiale du liquide par rapport aux mesures expérimentales. Dans le système triphasé, la combinaison des modèles noyaux de coalescence de Luo et de rupture de Lehr (Luo-Lehr) et de la coalescence de Luo et de rupture de Luo (Luo-Luo) prédisent des profils radiaux moyennés dans le temps qui sont valides pour la vitesse axiale moyenné dans le temps par rapport aux expériences. Cependant, à une vitesse de gaz superficielle élevée, ces profils prédisent un comportement non réaliste par rapport aux observations empiriques.

Les résultats de l'analyse de sensibilité du maillage montrent qu'avec des cellules de 3 mm, le model prédit une tendance similaire aux valeurs empiriques pour les profils radiaux de concentration du gaz, de vitesse axiale du liquide et de vitesse axiale solide. Le nombre de classes

de bulles influe sur les distributions prédites de taille de bulle dans le système triphasé alors que les schémas de discrétisation numériques n'ont aucune influence sur les résultats. Les résultats des simulations d’un banc d’essai avec diffuseur à bulles poreux montrent que tenir compte du terme de dispersion influence le comportement hydrodynamique de la colonne à bulles.

SUMMARY

The industrial partner of this project uses a slurry bubble reactor for the production of biogenic methanol. In the latter syngas is dispersed into the slurry continuous phase containing both liquid and solid phases. The rising bubbles containing a wide spectrum of the bubbles sizes, interact with the continuous phase due to the interface momentum transfer. The latter includes the drag, lift, wall lubrication and turbulent dispersion terms that require average bubble size, which needs to be calculated. One way to predict this average bubble size is by using population balance model (PBM), which can be coupled with the Eulerian framework. PBM also needs closure kernels for the bubble coalescence and bubble breakup.

In this study, the influence of bubble coalescence and bubble breakup kernels have been studied in two- and three-phase system using eulerian approach, which solves momentum equation for each phase. The influence of the mesh sizes, number of bubble classes, numerical schemes, wall lubrication force and turbulent dispersion force are also included. In the two-phase system, results show that the Luo coalescence model needs to be tuned when used in combination with the Luo breakup kernel. The combination of the Luo coalescence and the Lehr breakup kernels (Luo-Lehr) show promising time-averaged radial profiles of gas holdup and axial liquid velocity as compared to empirical values. In the three-phase system, the combination of the Luo coalescence and the Lehr breakup kernels (Luo-Lehr) and the Luo coalescence and the Luo breakup kernels (Luo-Luo) predict convincing time-averaged radial profile of axial solid velocity as compared to experiments. However, at an elevated superficial gas velocity, a non-realistic behavior was predicted when compared to empirical observations.

The sensitivity analysis results show that the 3 mm mesh size depicts a trend similar to the empirical values of the radial profiles of the gas holdup, axial liquid velocity, and solid axial velocity. The number of bubble classes influence the predicted bubble size distribution in the three-phase system while the numerical discretizing schemes have no influence on the results. The bench simulation results show that the inclusion of the turbulent dispersion term using a single porous tubular sparger influences the hydrodynamic behavior of the bubble column.

TABLE OF CONTENTS

LIST OF FIGURES

LIST OF TABLES

NOMENCLATURE

Notation

a_i	Constant
B_B	Bubbles birth due to breakup phenomena
B_C	Bubbles birth due to coalescence phenomena
c_0	Coalescence parameter
C_1	Constant equals 1.44
C_2	Constant equals 1.92
c_2	Constant equals 0.841
c_3	Constant equals 0.923
C_μ	Constant equals 0.09
C_D	Drag coefficient
C_f	Increase coefficient of surface area
C_L	Lift coefficient
C_{wl}	Wall lubrication coefficient
C_{w1}, C_{w2}	Constant values -0.01 and 0.05
C_{wc}, C_{wd}	Constant values 10.0 and 6.8
C_{TD}	User modifiable constant equals 1
D	Column/pipe diameter, m
D_B	Bubbles death due to breakup phenomena
D_C	Bubbles death due to coalescence phenomena
$D_{t,pq}$	Scalar fluid particulate dispersion tensor
d	Mean diameter, m
d_i, d_j	Diameter of bubble of size i and j, m
d_h	Maximum horizontal length of the deformed bubble, m
d_{max}, d_{min}	Maximum/Minimum diameter of bubble, m
Eo, Eo'	Eotvos and modified Eotvos numbers

e_{ss}	Coefficient of restitution, equals =0.9
e_s	Bubble surface energy
$\bar{e}_s$	Arrival Eddies energy
$\boldsymbol{F}$	Inter-phase momentum exchange term, kg/m^2.s^2
$\boldsymbol{F}_D$	Drag force, kg/m^2.s^2
$\boldsymbol{F}_L$	Lift force, kg/m^2.s^2
$\boldsymbol{F}_{TD}$	Turbulent dispersion force, kg/m^2.s^2
Fr	Froude number
f	Volume fraction of daughter bubble
G	Production term of turbulent model
$g_{0,ss}$	Radial distribution function
g	Gravitational force, m/s^2
H_D	Heterogeneity index
I_{2D}	Second invariance of the deviatoric stress tensor
$\bar{\bar{I}}$	Unit tensor
I_{2D}	Second invariance of the deviatoric stress tensor
K	Interphase momentum exchange coefficient, kg/m^3.s
k_{Θ_s}	Diffusion coefficient
k	Mean turbulent kinetic energy per unit mass, m^2/s^2
m	Fitted parameter equals 1.7
$m(v')$	Number of daughter bubbles equal 2
Mo	Morton number
n_i, N_i	Number density of bubble size i, #/m^3
n_w	Normal vector
$\dot{n}_\lambda$	Number density of eddy size
p, P	Pressure, Pa
p_B	Breakup efficiency
p_C	Coalescence efficiency
r	External coordinates, ratio factor for bubble volume
Re	Reynolds number

S	Source term
S_b	Bubble breakup source term
S_c	Bubble coalescence source term
t_c	Bubble contact time, s
t_I	Film drainage time, s
U	Velocity, m/s
$\boldsymbol{u}$	Phase velocity, m/s
$\bar{\boldsymbol{u}}$	Mean phase velocity, m/
$\tilde{\boldsymbol{u}}$	Instantaneous velocity, m/s
$\boldsymbol{u_{dr}}$	Drift velocity, m/s
$\boldsymbol{u'}$	Fluctuation velocity component, m/s
$\boldsymbol{V_x}$	Infinitesimal volume of internal coordinate, m^3
$\boldsymbol{V_r}$	Infinitesimal volume of external coordinate, m^3
v	Kinematic viscosity, kg/m .s
v, v'	Bubble volume, m^3
v_i	Volume of ith bubble class, m^3
We	Weber number
We_{crit}	Critical Weber number
x	Internal coordinate, bubble volume m^3
y_w	Distance to the wall
y^+	Dimensionless wall distance

Greek letters

α	Phase fraction
$\beta(v,v')$	Daughter size distribution
β	Constant equals 2
ε	Energy dissipation rate, m^2/s^3
ξ	Ratio of eddy size to parent bubble
$\boldsymbol{\lambda}$	Bulk viscosity, kg/m.s or Eddy size, m
ρ	Density, kg/m^3

$\Delta\rho_{pq}$	Absolute value of the density difference between disperse phase p and continuous phase q
η	Function of coefficient of restitution or conservation of numbers and mass
σ	Surface tension, N/m
σ_{pq}	Prandtl number
σ_k	Constant equals 1
σ_ε	Constant equals 1.3
Ω_B	Breakup rate, $1/m^3 s$
Ω_C	coalescence rate, $1/m^3 s$
π	Pi, equals 3.14159
θ	Test function used in the bubble class method
Θ	Granular temperature, m^2/s^2
μ	Shear viscosity of phase, kg/m.s
$\mu_{s,c}$	Solid viscosity due to collision, kg/m.s
$\mu_{s,fr}$	Solid viscosity due to friction, kg/m.s
$\mu_{s,k}$	Solid viscosity due to kinetic, kg/m.s
μ_t	Turbulent viscosity, kg/m.s
ω_C	Collision frequency
ω_B	Eddy-bubble collision
$\bar{\bar{\tau}}$	Shear stress
γ	Virtual mass constant equals 0.5
$\delta_{j,k}$	Kronecker delta function
γ_{Θ_s}	Collision dissipation energy
χ_c	Ratio of increase of bubble surface energy to arrival eddies energy (critical dimensionless energy ratio)
∅	Energy exchange between phases
ϕ	Phi, representation for other transport equations

Subscripts

b	Bubble
Dis	Distorted regime
Cap	Capped regime
i	Index for bubble classes
J	Index for bubble classes
k	Index for bubble classes
L	Liquid
m	Mixture phase
Min	Minimum
Max	Maximum
p	Disperse phase
q	Continuous phase
s	Solid phase
Vis	Viscous regime

ACKNOWLEDGEMENTS

Bismillahirrahmanirrahim,

I would like to express my gratitude to Professor Jean-Michel Lavoie for his kind support, advances, guidelines, and cooperation during this research. I would like to thank the jury members Professor Jean-Michel Lavoie, Professor Pierre Proulx, Professor José Luis Sánchez, Dr. Micael Boulet and Dr. Tommaso for reviewing the thesis and providing the valuable comments.

I would like to thank the Industrial Research Chair on Cellulosic Ethanol and Biocommodities of the Université de Sherbrooke and especially its sponsors: The Ministère de l'Énergie et des Ressources Naturelles du Québec (MERNQ), CRB Innovations, Enerkem and Éthanol GreenFIeld Québec Inc. I am grateful to MITACS for the grant and finally Compute Canada for having made possible to perform most of the simulations throughout high-performance computing (HPC) machines at the Université de Sherbrooke (Mammouth Parallel 2).

I am thankful to my research supervisors Dr. Micael Boulet and Dr. Tommaso for providing the continuous help in the development of the models, lectures and weekly meetings. They were always available with a smiling face and I really appreciate their patience and kindness.

I am thankful to the members of the University of Sherbrooke especially Brian Driscoll, Sonia Gougeon and Sylvie Lebrun for helping me with the VPN-connection and paperwork. I am thankful to technicians Aca of Enerkem Inc. as well as Eric of CRIEC-B and Simon of CRIEC-B for assisting me to install the bench.

Last but not the least, I express my greatest gratitude to my family for their kind support. I dedicate this work to my mother and my wife.

It was a great honor working with such a dynamic team. I wish Jean-Michel and his team good future ahead.

Alizeb Hussain Syed

1 INTRODUCTION

1.1 Research Motivation

Under the intense temperature and pressure of Earth's core and prolong decaying of diatoms, the organic compounds are formed. These compounds involve hydrogen and carbon that are linked by chemical bonding to form hydrocarbon chains and ultimately the fossil fuels (Simon 2007). The former includes coal, oil, natural gas, plastics, polymers, etc. The reserves of fossil fuels are depleting in time due to increase in human population and their needs (Olah 2005). Another challenge with conventional fuel is related to environmental issues, especially the emission of the greenhouse gases (Brilman et al. 2013). To overcome these issues, alternative source of fuels are being considered. The latter at this point includes hydrogen, ethanol, bio-diesel, methanol, etc. Details about these fuels were abundantly reported in the literature (Olah et al. 2009).

Methanol synthesis is mature and accessible since the 1920s. Researchers over the last decades developed new catalyst in order to minimize the intense operating condition while optimizing the efficiency. Also, efforts toward the alternative source of raw materials (such as syngas from biomass) have been made. Methanol and its derivatives are fascinated by industries, governments, and academia. The 'methanol economy' has been proposed as a future economy, aiming to replace fossil fuel by methanol and its derivatives. One of the challenges with methanol production is related to the cost of infrastructure, conversion cleanness, process efficiency, distribution and storage (Lee et al. 2007). These limitations have open new opportunities for academic and industrial research and development.

One of the most commonly used methods to produce methanol is via conversion of synthetic gas (syngas). The latter involves a mixture of hydrogen, carbon monoxide, and carbon dioxide as a feedstock and it is produced by steam reforming, auto-thermal reforming, partial oxidation, gasification, and water-gas-shift (Liu et al. 2010). Typical methanol production involves the following steps: (a) Purification of the feed (b) formation and compression of the syngas; (c) conversion of the syngas into methanol; (d) distillation of the effluent from the reactor (e) lastly, recovery and recycling of the methanol.

Methanol synthesis was first reported in 1923 by the Badische Anilin- und Soda-Fabrik company (BASF) and was based on ZnO/Cr_2O_3 catalyst using the temperature and pressure of 350-450 ^{0}C and 250-350 atm, respectively. This technology was used for over 50 years after which Imperial Chemical Industries (ICI), proposed the low-pressure technology that was operated at 225-275 ^{0}C and 50-100 atm using a $Cu/ZnO/Al_2O_3$ catalyst. The pressurized reactor consisted of single fixed bed catalyst. The Lurgi process used similar Cu-based (CuO/ZnO) catalyst, although the reactor consisted of tubes and shells system. The tubes were filled with catalyst while the shell was filled with hot water to control temperature. The other methanol synthesis is based on the Kellogg, Mitsubishi and Topsoe technologies and the key difference in each technology is often the type of catalyst used. The previously discussed technologies use hydrogen-rich syngas as a feed stream, which is commonly driven from natural gas source. However, coal-based syngas, which is low in H-to-C ratio typically produces a CO-rich syngas (Lee et al. 2007). The liquid phase methanol synthesis technology (LPMEOH) targets such CO-rich syngas feedstock and is being demonstrated on a commercial scale using a slurry bubble column (Heydorn et al. 2003).

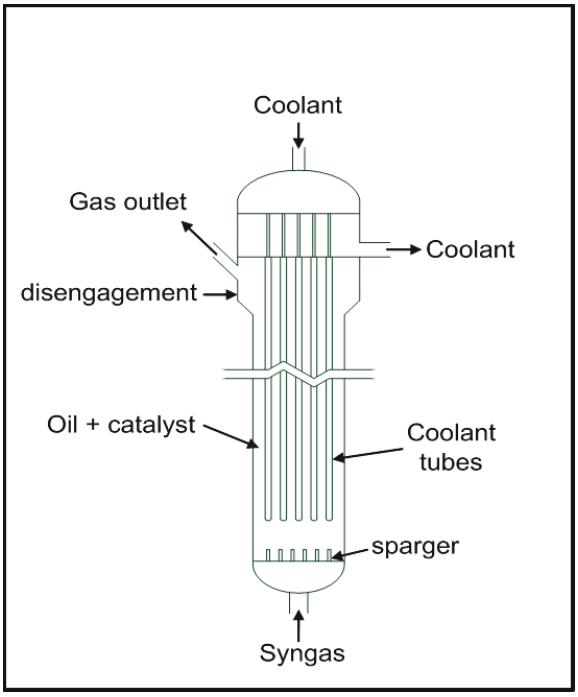

Fig. 1-1 Illustration of industrial scaled bubble column for the production of methanol

Bubble columns have been reported in the chemical, petrochemical, bioprocesses, and pharmaceutical industries. In the chemical and petrochemical industries, the major processes include partial oxidation of ethylene to acetaldehyde, isobutene hydration (Deckwer 1992) and the

Fischer-Tropsch synthesis of hydrocarbons (Wender 1996). In the bio-processes and pharmaceutical industries, the major processes are the waste-water treatment (Smith et al. 1996) and the single cell protein (Lee & Liang-Shin 2002). The Bubble columns have numerous advantages, for instance, the ease of construction due to the absence of moving parts inside the reactor, high heat transfer rate that provides uniform temperature distribution through the column even when operating with exothermic reactions and easy removal of slurry for catalyst regeneration as compared to the fixed bed. Bubble columns have some disadvantages, for instance, back-mixing, foaming, and short residence time that depend on the bubble rise velocity and phase separation (Deckwer 1992). In simple bubble column reactors (see Fig. 1-1), the gas phase is dispersed into the continuous phase, consisting liquid and solid-particles (catalyst). In most cases, the inlet flow includes a gas phase, however, the possibility to re-circulate the liquid do exist. Superficial gas velocity varies usually from 0.02 to 0.2 m/s and lower liquid superficial velocity (0 to 0.05 m/s). Hence, the gas flow rate mainly contributes in the hydrodynamics of the bubble column reactors and dictates the overall efficiency (Shaikh & Al-Dahhan 2013). Some of the fundamental parameters of bubble column are the flow regime, gas holdup, and mass transfer.

The flow regime inside the bubble column is either homogeneous, heterogeneous or slug, which mainly depends on the superficial velocities and the column diameter. In homogeneous regime, the bubble size is assumed to be constant and bubble coalescence do not occur. With an increase of the gas flow rate, large bubbles are formed due to bubble coalescence and called heterogeneous regime. This regime is industrial favorable, however, the physics is very complex, which is related to bubble-bubble and bubble-particle interactions. These interactions are not well developed and open literature is limited. If the column diameter is less than 15 cm, the heterogeneous regime becomes a slug flow. Fig. 1-2, shows the possible flow regimes in the bubble column as a function of superficial gas velocity and column diameter. The transition area lies between the flow regimes and depends on the gas distributor and material properties.

The gas holdup is the most important design criteria in the bubble column and it is related to bubble size to determine the interfacial area and ultimately defines the heat and mass transfer phenomena (Deckwer 1992). The gas holdup depends on the gas and liquid velocities, operating conditions (temperature and pressure), gas distributor, column diameter and loading height, continuous phase property, and solid particles. Liquid phase properties influence the formation of bubble size. An

increase in the liquid viscosity promotes the bubble coalescence and hence decreasing the gas holdup. The presence of solid generally decreases the gas holdup, especially when using the fine particles ($< 100\ \mu m$). This behavior is not universal and opposite trends (increase in holdup) also were reported. One of the possible reasons for a decrease in holdup is that the presence of solid increases the pseudo-viscosity of the suspension that forms the large bubbles. The overall mass transfer or volumetric mass transfer rate with respect to disperse volume in a bubble column is the product of liquid-side mass transfer coefficient (k_l) and specific interfacial area (a). The latter is a function of gas holdup and bubble size (Yang 2003).

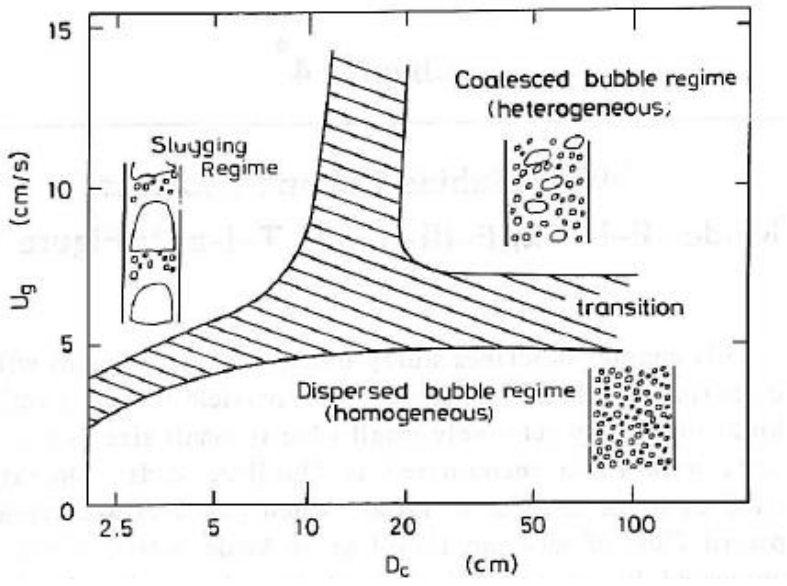

Fig. 1-2. Typical flow regimes as a function of column diameter and superficial gas velocity in the bubble column using porous sparger (Deckwer 1992)

Slurry bubble columns are still in the developing stage because of the complexity related to fluid dynamics, which includes the phase fractions, bubble size distribution, bubble coalescence, bubble breakup, phase velocities, interphase momentum transfer, mass transfer coefficient, and turbulence. One way to understand the behavior of the fluid locally inside the column is with the aid of Computational Fluid Dynamics (CFD). The latter takes into account the bubble size distribution using a population-balance model (PBM) and predicts the Sauter-mean bubble size locally along with other important parameters, for instance, the phase fractions, velocity profiles and turbulence intensity. PBM needs closure models for the bubble coalescence and breakup phenomena. In open literature, the influence of these models are limited especially in case of three phase slurry column. In this study, the focus is made on the PBM closure models using different

operating conditions. This provides an insight look of the column and assists in improving the current understanding of industrial-scale slurry column, hence, providing a step head towards the optimization.

1.2 Research Objectives

The main objectives of this work are to contribute to the understanding of the hydrodynamics of gas-liquid and gas-liquid-solid bubble columns operated both in the homogeneous and heterogeneous regimes (industrial favorable). As discussed earlier that the fluid dynamics influence the bubble size, which defines the heat and mass transfer coefficient. Hence, the performance of the bubble column depends on the bubble size. The slurry bubble column involves a large spectrum of the bubble sizes and prediction of correct bubble size inside the system is yet an open question. Due to the complexity of the system, this study focuses on hydrodynamics as a starting point and involves no mass/heat transfer and kinetic phenomena. The experiments and simulations will be operated at ambient temperature and pressure and the three major research goals are mentioned below:

- Installation of a laboratory-scale cold bench and perform experiments using air and water.
- Develop a model for two and three phase systems, which include the influence of interphase momentum transfer forces, numerical scheme, mesh size and population balance kernels. The latter kernels involve the bubble coalescence and bubble breakup phenomena.
- A validation of the developed models with the published data by Hills (1974) and Sannaes (1997).

2 STATE OF THE ART

Bubble columns are extensively modeled by computational fluid dynamics (CFD), which solves the transport equations locally for each phase and takes into account the interaction between phases in 2-dimensional or 3-dimensional systems. These interactions need a closure equations, which are provided by additional sub-models in the momentum interphase terms. Furthermore, the real system is often chaotic in nature, CFD includes this behavior by solving turbulence equations in which the fluctuating components of velocity are predicted. Another advantage of CFD is that it could be coupled with other models for instance population balance, which solves the bubble size distribution. For bubble columns, modeling approaches in CFD are divided into three categories which are the direct numerical simulations (DNS), the Euler-Lagrangian and the Euler-Euler approaches.

2.1 Direct Numerical Simulations (DNS)

DNS is the most desirable approach since it solves a wide range of spatial and time scales without undergoing any averaging process such as in the case of Reynolds-Average-Navier-Stokes equations (RANS). For gas-liquid bubbly flow, the time-dependent Navier-Stokes equation is solved for each phase and needs no turbulence model. This approach tracks the fluid interface and requires very fine mesh in order to capture all time and spatial scales. The interface can be classified into fixed and moving grids. The former involves pre-defined and stationary grid, which could be either structured or non-structured mesh. The algorithm applied on the mesh to track interface is based on volume-of-fluid (VOF) approach, which uses marker technique to identify each phase. The other techniques involve surface tension, level set, and interpolation. The details of all these techniques were well discussed in Scardovelli & Zaleski's (1999) work. The latter moving grid involves a non-stationary grid, which moves along the fluid. This approach is called a Lagrangian method, and the details could be found in the published data of Johnson & Tezduyar (1997).

Baten (2000) simulated a single bubble of different sizes using the VOF approach in Direct Numerical Simulations (DNS). The authors studied the behavior of bubble in which the bubble

rise velocity and interaction of bubble with the continuous phase were included. Based on their observations, the author proposed the drag coefficient. Bunner & Tryggvason (1999 and 2002) studied the influence of different bubble sizes on the bubble rise velocity. They considered a low gas hold of 6% and Reynolds number (< 30) in two and three dimensional systems. The authors concluded that the bubbles deformation were not significant, and bubbles dispersed homogeneously inside the system. Deen et al. (2004) studied the movement of a single bubble in a stagnant liquid using front tracking model which later used to obtain the drag, lift and virtual mass coefficients.

As discussed above, DNS generally works at a low Reynolds number and is limited to a single or a very few cluster of bubbles due to an intense computational cost. Furthermore, the bubble-bubble interactions, for instance, coalescence and breakup are also limited (Tryggvason et al. 2006). These limitations restrict DNS to be used for industrial applications, which are operated at elevated superficial velocities with a large spectrum of bubble sizes. Many authors have used alternative approaches, for instance, Euler-Lagrangian and Euler-Euler models to simulate the multiphase systems. These approaches involve the detail interactions between phases, which are defined by interface exchange terms and other closure correlations. Depending on the application and operating condition, each model has its own limitations.

2.2 Euler-Lagrangian Approach

In this approach, the continuous phase is solved by a single set of governing equation. Whereas the disperse phase, involving bubble or clusters of bubbles, is tracked by Newton's equation of motion. The interactions (drag and non-drag forces) between the phases are defined by additional models. The volume-averaged mass and momentum equations for the continuous phase is described by:

$$\frac{\partial(\alpha_q \rho_q)}{\partial t} + \nabla.\left(\alpha_q \rho_q \boldsymbol{u_q}\right) = 0 \tag{2-1}$$

$$\frac{\partial(\alpha_q \rho_q \boldsymbol{u}_q)}{\partial t} + \nabla.\left(\alpha_q \rho_q \boldsymbol{u_q} \boldsymbol{u_q}\right) = -\alpha_q \nabla p + \nabla \overline{\overline{\tau_q}} + \alpha_q \rho_q \boldsymbol{g} + \boldsymbol{F}_{qp} \tag{2-2}$$

Where $\alpha_q, \rho_q, \boldsymbol{u}_q, p, \overline{\overline{\tau_q}}, \ and \ \boldsymbol{g}$ represent the volume fraction, density, velocity, stress tensor and gravitational acceleration, respectively. The last term $\boldsymbol{F}_{qp}$ is referred to the interface momentum transfer for the continuous phase due to the motion of bubbles. This momentum transfer from

bubbles to liquid phase is simulated by one-way, two-way, or four-way coupling depending on the concentration of disperse phase. One-way coupling considers a very low void fraction of disperse phase and the movement of the bubbles do not influence the flow field of the continuous phase. Hence, the latter phase is independent of the presence of bubbles ($\boldsymbol{F}_{qp} = 0$). In two-way coupling, each phase influences the flow field of the other phase and vice versa ($\boldsymbol{F}_{qp} \neq 0$).

Four-way coupling deals with the higher void fraction of disperse phase in which the particle-particle interaction is inevitable and the additional momentum transfer between particles are included along with the two-way coupling. The particle-particle collision and particle-fluid interaction need turbulence closure, which is often based on the k-epsilon model. Keeping in mind that without the inclusion of turbulence model, the four-way coupling reduces to two-way coupling. Depending on the Stokes number one could determine the type of coupling is needed to simulate the multiphase system (see Fig. 2-1). The further details of coupling, derivations and interface forces in the Lagrangian approach, are reported in the work of Brennen (2005) and Yeoh et al. (2014).

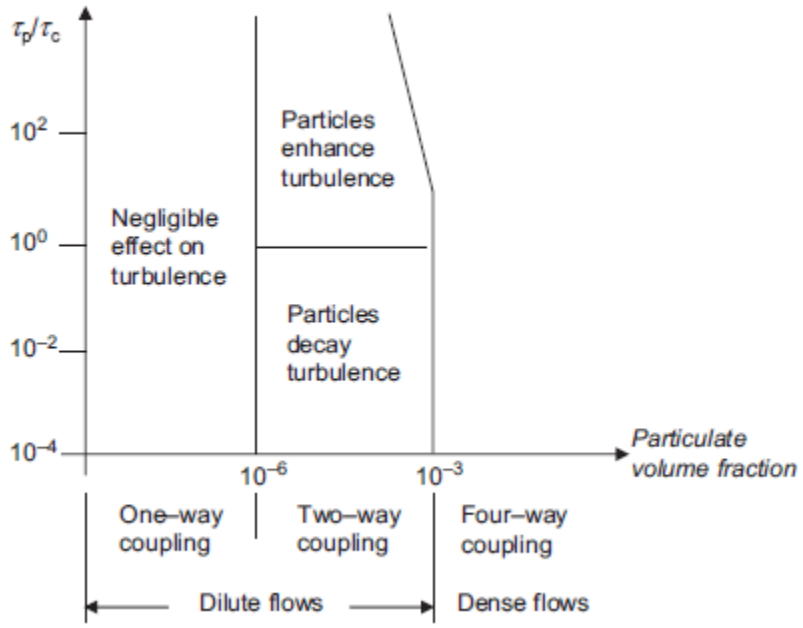

Fig. 2-1. Interaction between disperse and continuous phase as a function of volume fraction and stoke number (Yeoh et al. 2014)

Many authors have used Euler-Lagrangian approach to investigate the flow fields inside a bubble column (Delnoij et al. 1997; Delnoij et al. 1999; Lain et al. 2002; Bunner & Tryggvason 2002; Farzpourmachiani et al. 2011). The continuous phase generally acts as a carrier in which the

bubbles are tracked. Commonly, the particle-particle interaction includes the random movement, dispersion, and collision whereas the particle-fluid interaction involves the drag, virtual mass, lift, basset history forces and Brownian forces.

Lain et al. (2002) studied the hydrodynamics and turbulence behavior of a two-phase bubble column with the Euler-Lagrangian approach using axis-symmetric geometry. The gas void fraction of the diluted system was between 0.37 and 1.31%. Authors considered a narrow bubble size distribution that was in the range of 0.2 and 0.9 mm with an average bubble diameter of 0.5mm. They concluded that bubble-induced turbulence is required in order to correctly predict the velocity profiles of liquid and gas. Buwa et al. (2006) used similar Euler-Lagrangian approach and studied the influence of lift force on the gas-liquid flow fields using rectangular bubble column. The superficial gas velocity was in the range of 0.0014 m/s and 0.0073 m/s and the total gas holdup was under 2.5%. A constant bubble size of 5 mm was considered for all simulations while the bubble coalescence and breakup were ignored. Authors suggested that with the inclusion of the lift force the predicted results were close to experimental values. Bannari et al. (2008) simulated the same experimental setup used by Buwa et al. (2006) using a population-balance method that considered bubble coalescence and bubble breakup. The authors reported a presence of bubble size distribution instead of a constant bubble size.

Zhang & Ahmadi (2005) simulated a three-phase slurry column and studied the oscillation of the bubble plume. The gas and particle phases were investigated using a Lagrangian approach whereas the liquid was treated using the Eulerian framework. They concluded that the plume was S-shape and influenced by the bubble rise velocity. Authors also reported that the bubble size influenced the liquid and solid flow fields. Hu & Celik (2008) studied the partially aerated bubble column using two different turbulence model, the Reynold-Average Navier-Stoke equations (RANS) and Large-Eddy Simulation (LES). The author reported that the latter shows improvement in the results in term of bubble plume, mean velocity, and velocity fields. Sungkorn et al. (2011) also simulated the diluted system (gas fraction $\leq 2\%$) using a Lattice-Boltzmann scheme for the continuous phase and improved equation of the dispersed phase. The latter involves modified bubble-bubble collision model, which was based on the kinetic theory. They reported that the modified-collision model improves the trajectory of the bubbles along with a lower computational cost. Mattson & Mahesh (2012) considered only the bubble coalescence phenomenon and ignored the bubble

breakup. The former was depended on the probability function which is a ratio of fluid drainage and bubble-bubble contact timescale. The results showed that the number of bubbles decreased as the bubble coalescence increased. The author reported that the predicted bubble size distribution was in good agreement with empirical values.

The Euler-Lagrangian has many advantages including an accurate description of interphase forces, particle tracking, four-way coupling, and transport phenomena of the individual bubble (Kitagawa et al. 2001; Buwa et al. 2006). However one of the major drawbacks is the computational time, which is mainly due to particle-particle and particle-wall interactions (Deen et al. 2004; Wiemann & Mewes 2005; Chiesa et al. 2005). This limits the Euler-Lagrangian approach to be used in an industrial bubble column with elevated superficial velocities, gas holdup, and solid loading.

2.3 Eulerian-Eulerian Approach

The industrial scale bubble columns are extensively simulated by the Eulerian-Eulerian approach. The Eulerian framework is based on interpenetrating media and assumes that the fluids are in motion, however, the grid is fixed. The interaction between phases is defined using interphase exchange terms in the conservation equations. Generally, in three-phase system, the liquid is considered as a continuous phase while the gas and solids as a disperse phases. The conservation equations in this framework are ensemble-averaged and predict the macroscopic behavior of the flow patterns.

2.4 Interface Forces in Multiphase Flow

2.4.1 Drag Force

The drag force, see Fig. 2-2, was initially developed by Newton's in 1710 for high relative velocities, in which only the inertial effect is accounted. However, Stokes in 1850, suggested that for low relative velocities the inertial effect could be neglected and proposed a drag force involving the viscous effect (Soo 1990). The Stokes drag force (F_D) on a single rigid spherical bubble in a steady state is defined as:

$$\boldsymbol{F}_D = -\frac{1}{2} C_D \rho_q \left(\frac{\pi}{4} d_b^2\right) |\boldsymbol{u}_p - \boldsymbol{u}_q| (\boldsymbol{u}_p - \boldsymbol{u}_q) \tag{2-3}$$

Where p, q, C_D, ρ_q, d_b and $(\boldsymbol{u}_p - \boldsymbol{u}_q)$ repesent the index for the disperse phase, index for the continous phase, drag cofficent, liquid phase density, bubble diameter and slip velocity, respectively. The drag force for a swarm of bubbles in a multiphase system is given by:

$$\boldsymbol{F}_D = -\frac{3}{4}\alpha_p \rho_q \frac{C_D}{d_b}|\boldsymbol{u}_p - \boldsymbol{u}_q|(\boldsymbol{u}_p - \boldsymbol{u}_q) \tag{2-4}$$

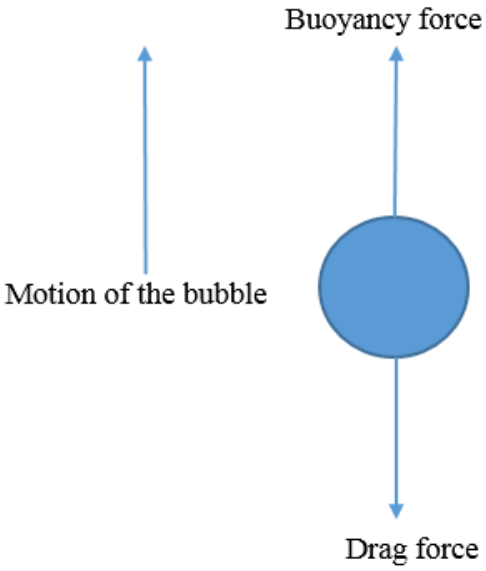

Fig. 2-2. Drag force applied on a single spherical bubble

Schiller & Naumann (1933) developed the drag coefficient (C_D) using a single rising bubble and correlated C_D with Reynolds number. Depending on the flow regime, the drag coefficient formulation changes. For a bubbly regime (Re <1000), the bubbles are assumed spherical while for higher Reynolds number, C_D is a constant. The drag coefficient is described as:

$$C_D = \begin{cases} 24(1 + 0.15Re^{0.687})/Re & Re \leq 1000 \\ 0.44 & Re > 1000 \end{cases} \tag{2-5}$$

The Reynolds number (Re) is defined as follows:

$$Re = \frac{\rho_q |\boldsymbol{u}_p - \boldsymbol{u}_q| d_b}{\mu_q} \tag{2-6}$$

Where μ_q is the viscosity of the continuous phase.

Morsi & Alexander (1972) also defines C_D as a function of the Reynolds number, however they divided the range of Reynolds numbers into 8 regions, covering wide range of Reynolds number

from 0.1 to 10000. The authors correlation was developed for a spherical bubble and it is defined as:

$$C_D = a_1 + \frac{a_2}{Re} + \frac{a_3}{Re^2} \tag{2-7}$$

Here the constants a_i are given by:

$$a_1, a_2, a_3 = \begin{cases} 0{,}24{,}0 & 0 < Re < 0.1 \\ 3.69{,}22.73{,}0.0903 & 0.1 < Re < 1 \\ 1.222{,}29.1667{,}-3.8889 & 1 < Re < 10 \\ 0.6167{,}46.50{,}-116.67 & 10 < Re < 100 \\ 0.3644.98.33.-2778 & 100 < Re < 1000 \\ 0.357{,}148.62{,}-47500 & 1000 < Re < 5000 \\ 0.46{,}-490.546{,}578700 & 5000 < Re < 10000 \\ 0.5191{,}-1662.5{,}5416700 & Re > 10000 \end{cases} \tag{2-8}$$

Ishii & Zuber (1979) correlation includes the shape of the bubble using the Eotvos number. The bubble shapes consist of the sphere (viscous regime), ellipse (distorted regime) and cap (capped regime). The correlation switches depend on the local Reynolds number in the viscous regime ($0 \leq Re < 1000$) and for distorted and cap regime ($Re \geq 1000$). The drag force and the Ishii drag coefficient are given by:

For viscous regime [$C_{D,dis} < C_{D,vis}$]

$$C_{D,sph} = \frac{24}{Re}(1 + 0.1Re^{0.75}) \tag{2-9}$$

For distorted regime [$C_{D,vis} < C_{D,dis} < C_{D,cap}$]

$$C_{D,dis} = \frac{2}{3} d_p \sqrt{\frac{g\Delta\rho}{\sigma}} \left(\frac{1 + 17.67 f^{*\frac{6}{7}}}{18.67 f^*} \right), \qquad f^* = (1 - \alpha_p)^{1.5} \tag{2-10}$$

For capped regime [$C_{D,dis} > C_{D,cap}$]

$$C_{D,cap} = \frac{8}{3}(1 - \alpha_p)^2 \tag{2-11}$$

Where $d_p, g, \Delta\rho, \sigma$ and α_p represent the bubble diameter, gravitational force, density difference, surface tension and disperse phase fraction, respectively.

In fluid-solid systems, the main drag coefficient involves the Schiller & Naumann (1933), Wen & Yu (1966), Gidaspow et al. (1992) and Energy-Minimization Multi-Scale (Li et al. 1999; Ge & Li

2002) models. All these correlations (except Naumann et. al) were originally developed for the fluidized bed containing gas and solid phases. However, these correlations are often used in slurry bubble column to define the liquid and solid drag coefficient. The Wen & Yu formulation is similar to the Naumann et. al and it is given as:

$$C_D = \frac{24}{\alpha_l Re_s}(1 + 0.15(\alpha_l Re_s)^{0.687}) \tag{2-12}$$

Where $\alpha_l \; and \; Re_s$ are the liquid phase fraction and particle Reynolds number. The latter is calculated by equation (2-6).

Gidaspow et al. (1992) formulation covers a wide range of volume fraction and depending on the flow regime, different drag coefficients are used. The Gidaspow correlation is the combination of the Wen & Yu model and the Ergun equation. If the volume fraction of the solid phase is less than 20%, the Wen & Yu formulation is considered which is based on Stokes drag coefficient using particle Reynolds number. If the phase fraction is above 20%, the Ergun equation is utilized which is derived from packed-bed pressure drop expression.

$$\boldsymbol{F}_{D,qs} = K_{q,s}\left(\boldsymbol{u}_q - \boldsymbol{u}_s\right) \tag{2-13}$$

$$K_{q,s} = \frac{3}{4}\alpha_s \alpha_q \rho_q \frac{C_{D,qs}}{d_s}\left|\boldsymbol{u}_q - \boldsymbol{u}_s\right|\alpha_q^{-2.65}, \qquad \alpha_q > 0.8 \tag{2-14}$$

$$K_{q,s} = 150\frac{\alpha_s(1-\alpha_q)\mu_q}{\alpha_q d_s^2} + 1.75\frac{\alpha_s \rho_q \left|\boldsymbol{u}_q - \boldsymbol{u}_s\right|}{d_s}, \qquad \alpha_q \leq 0.8 \tag{2-15}$$

Where $K_{q,s}, \boldsymbol{u}_q - \boldsymbol{u}_s, \alpha_s, \alpha_q, \rho_q, C_{D,qs}, d_s$ and μ_q are the fluid-particle exchange coefficient, slip velocity between continuous and disperse phases, solid phase fraction, continuous phase fraction, continuous phase density, drag coefficient between liquid and solid, solid particle size and the continuous phase viscosity. The liquid-solid drag coefficient is calculated from the equation (2-12).

The Energy-Minimization Multi-Scale (EMMS) correlation was developed for the circulating fluidizing bed (CFB) in which the regimes are divided into dense and dilute segments. The former segment is found at the bottom of the CFB containing dense solid-rich phase and gas-rich dilute phase (heterogeneous regime). The dilute segment occurs at the top of the CFB containing dense gas-rich phase mainly and the flow fields are uniform. Each segment is distinguished from a dense solid-phase to dilute gas-phase with respect to eight hydrodynamics parameters (superficial

velocities, phase fractions, minimum fluidizing velocity and others). Depending on the hydrodynamics parameters, the drag force is solved for each segment (dense phases, dilute phases and dense-dilute interactions). For gas-liquid flow, the disperse gas phase is associated with the dilute phase and the continuous phase is linked to dense phase (Ellenberger & Krishna 1994; Yang et al. 2007). Similarly, in a liquid-solid system, the solid phase is considered to be a dilute phase and the continuous phase as a dense phase. EMMS based drag force (Xu et al. 2014) is given by:

$$K_{q,s} = \frac{3}{4}\alpha_s \alpha_q \rho_q \frac{C_{D,qs}}{d_s}\left|\boldsymbol{u}_q - \boldsymbol{u}_s\right|\alpha_q^{-2.65} H_D \tag{2-16}$$

Where heterogeneity index H_D is defined as

$$H_D = a(Re_s + b)^c \tag{2-17}$$

Here a, b and c are the fitted parameters depending on the minimum fluidization void fraction.

2.4.2 Lift Force

The perpendicular force that is applied on the upward rising bubbles and is called transverse or lift force. This force is caused by three different mechanisms: the Magnus, the Saffman, and the deformed-bubble. At high Reynolds number, the Magnus lift force is caused by the rotation of the spherical bubbles in a uniform flow field (quiescent continuous phase). This rotation causes the surrounding fluid to entrain, hence producing the higher velocity on one side and lower on the other side, which ultimately forms an asymmetric pressure distribution. This behavior causes the bubbles to follow a higher velocity region. At low Reynolds number, the Saffman lift force is caused by a shear (friction) in the continuous phase and it is applied to non-rotating bubbles. At intermediate to high Reynolds numbers, bubbles tend to deform, like in the bubble columns, and the lift force is linked to that deformation. The wake behind the deformed-bubbles cause the lift force (Chen 2004). This lift force is described by Zun (1980) and it takes into the account disperse phase fraction (α_p), the density of continuous phase (ρ_q), the relative velocities between phases $\left(\boldsymbol{u}_p - \boldsymbol{u}_q\right)$, the velocity gradients ($\boldsymbol{\nabla u}_q$) and the lift coefficient ($-C_L$).

$$\boldsymbol{F}_L = -C_L \alpha_p \rho_q \left(\boldsymbol{u}_p - \boldsymbol{u}_q\right)\left(\boldsymbol{\nabla u}_q\right) \tag{2-18}$$

The Zun reported that the value of this lift coefficient (C_L) is in the range of 0.25 and 0.3. Lahey (1990) studied the influence of lift coefficient in different flow regimes, covering wide range of gas void fraction and reported the C_L value in the range of 0.01 and 0.5.

Tomiyama (1998) studied the lift coefficient using a single bubble in a shear flow. The author reported that the lift coefficient varies based on the bubble size. For small bubble size, the lift coefficient depends on the Reynolds number entirely, whereas the larger bubbles is a function of the modified Eotvos number, which considers the characteristic length of a deformed-bubble. This lift coefficient plays an important role in defining the shape of the radial profile of gas holdup and liquid velocity. The direction of the bubbles changes if the lift coefficient has a positive or negative value. Small bubbles (db <5.8 mm) are known to have a positive lift coefficient and bubbles tend to go towards the lowest liquid velocity (towards the wall). Larger bubbles (db > 5.8 mm) are associated with a negative value and tend to stay at the core of bubble column. The Tomiyama lift coefficient is defined by:

$$C_L = \begin{cases} min\left[0.288\, tanh\left(0.121Re, f(Eo')\right)\right], for\ Eo' \leq 4 \\ f(Eo'), \qquad\qquad for \leq Eo' \leq 10 \\ -0.27 \qquad\qquad for\ 10 \leq Eo' \end{cases} \tag{2-19}$$

$$f(Eo') = 0.00105{Eo'}^3 - 0.0159{Eo'}^2 - 0.0204Eo' + 0.474 \tag{2-20}$$

$$Eo' = \frac{g\left(\rho_q - \rho_p\right)d_h^2}{\sigma} \tag{2-21}$$

Where $C_L, Re, Eo', g, \rho_q - \rho_p, \sigma$ and d_h represent the lift coefficient, Reynolds number, modified Eotvos number, gravitational force, density difference, surface tension and maximun horizontal length of the deformed bubble, respectively.

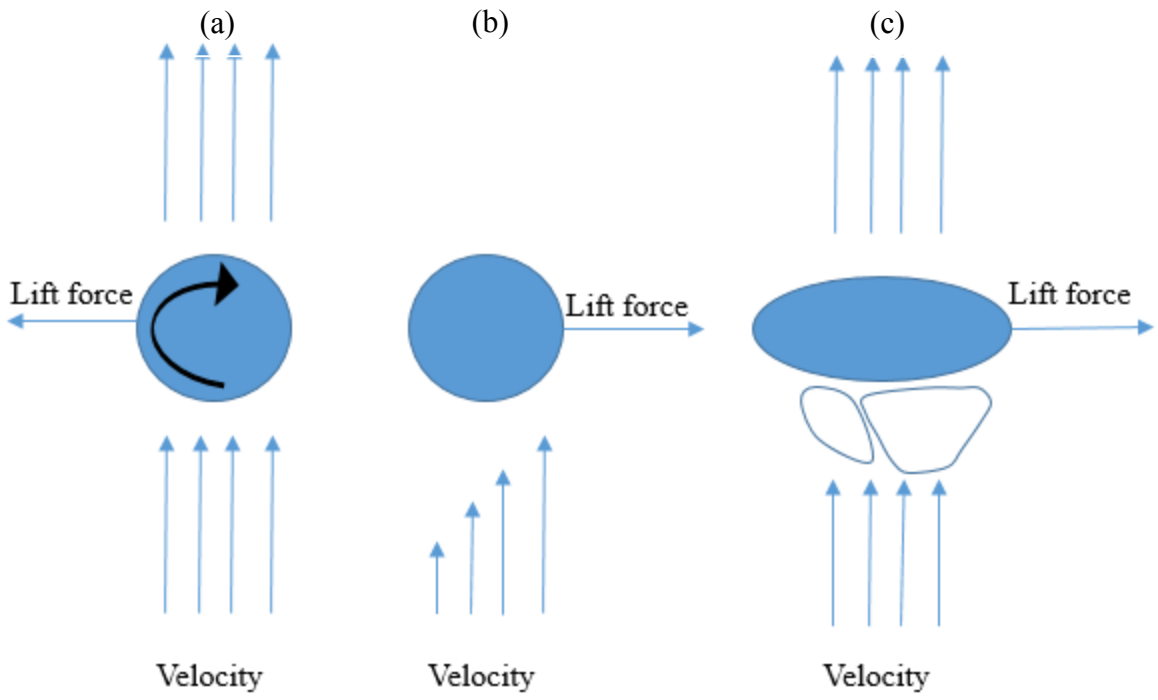

Fig. 2-3. Illustration of lift force in three mechanisms (a) Magnus (b) Staffman and (c) deformed-bubble

2.4.3 Wall Lubrication force

Antal et al. (1991) proposed a wall lubrication force, also known as the lift force at the wall, acts near the vicinity of the wall. The no-slip condition at the wall lowers the drainage rate between the rising bubble and the wall, which ultimately increases the drainage rate on the other side of the bubble. This behavior creates a force that tends to move the bubble away from the wall. The formation of wall lubrication force is similar to the lift force and it is described as:

$$\boldsymbol{F}_{wl} = C_{wl}\alpha_p\rho_q \left|\left(\boldsymbol{u}_p - \boldsymbol{u}_q\right)_{\|}\right|^2 (\boldsymbol{n}_w) \tag{2-22}$$

Where C_{wl}, $\left(\boldsymbol{u}_p - \boldsymbol{u}_q\right)_{\|}$ and $\boldsymbol{n}_w$ are the wall lubrication coefficient, the relative velocity tangential to the wall surface and the normal vector. The wall lubrication coefficient is defined as:

$$C_{wl} = max\left(0, \frac{C_{w1}}{d_b} + \frac{C_{w2}}{y_w}\right) \tag{2-23}$$

Here C_{w1} and C_{w2} are constant (equal to -0.01 and 0.05 respectively) whereas y_w represents the distance to the wall and it is written below as:

$$y_w \leq -\left(\frac{C_{w2}}{C_{w1}}\right) d_b \tag{2-24}$$

Tomiyama (1998) performed the multiple experiments using an air and glycerin fluids in a cylindric (pipe) geometry and modified the lift coefficient proposed by the Antal model. The modified correlation involves the influence of the bubble shape factor (Eotvos number). The Tomiyama wall lubrication coefficient is given as:

$$C_{wl} = C_w \frac{d_b}{2}\left(\frac{1}{{y_w}^2} - \frac{1}{(D-y_w)^2}\right) \tag{2-25}$$

Where C_w and D represent the modified correlation (factor) and column diameter. The former is a function of the Eotvos number and define as:

$$C_w = \begin{cases} 0.47 & Eo < 1 \\ e^{-0.933Eo+0.179} & 1 \leq Eo \leq 5 \\ 0.00599Eo - 0.0187 & 5 < Eo \leq 33 \\ 0.179 & 33 \leq Eo \end{cases} \tag{2-26}$$

And the Eotvos number is defined as:

$$Eo = \frac{g(\rho_q - \rho_p)d_b^2}{\sigma} \tag{2-27}$$

Hosokawa et al. (2002) conducted the experiments to study the lateral movement of a single bubble close to the wall. The authors concluded that the wall lubrication coefficient does not only depend on the Eotvos number but is also a function of the Reynolds numbers. The experiments were performed in the range of $2.2 \leq Eo \leq 22$ and $-6.0 \leq log_{10}Mo \leq -2.5$ while the wall lubrication coefficient is given by:

$$C_{wl} = max\left(\frac{7}{Re^{1.9}}, 0.0217Eo\right) \tag{2-28}$$

Here Mo is the Morton number.

Frank et al. (2004) simulated an upward flow in a vertical pipe. Their proposed correlation removes the dependency of the pipe diameter in the Tomiyama wall lubrication coefficient. The Frank wall lubrication coefficient is given as:

$$C_{wl} = C_w max\left(0, \frac{1}{C_{wd}} \cdot \frac{1 - \frac{y_w}{C_{wc}d_b}}{y_w\left(\frac{y_w}{C_{wc}d_b}\right)^{m-1}}\right) \tag{2-29}$$

Where C_{wd}, C_{wc} and m are the fitted parameters and equal to 6.8, 10.0 and 1.7, respectively.

2.4.4 Turbulent Dispersion Force

The turbulent dispersion force accounts for the interaction between turbulent eddies and disperse phase, as shown in Fig. 2-4. This force transports the disperse phase from the most to the least concentrated region. The averaging of the instantaneous interface drag force gives the mean and the fluctuating component of drag force and mathematically it is written below as

$$K_{pq}\left(\tilde{\boldsymbol{u}}_p - \tilde{\boldsymbol{u}}_q\right) = K_{pq}\left(\boldsymbol{u}_p - \boldsymbol{u}_q\right) - K_{pq}\boldsymbol{u}_{dr} \tag{2-30}$$

The left-hand term represents the instantaneous interface drag force, whereas the first and second terms on the right-hand side of the equation are the mean-drag force expressed in equation (2-4) and the fluctuating component of the drag force, also known as turbulent dispersion force F_{td}.

$$F_{td,q} = -F_{td,p} = K_{pq}\boldsymbol{u}_{dr} \tag{2-31}$$

Lopez De Bertodano (1991) correlated the drift velocity ($\boldsymbol{u}_{dr}$) with the turbulent kinetic energy of the continuous phase (k_q) and defined the turbulent dispersion force as

$$F_{td,q} = -F_{td,q} = C_{td}\rho_q k_q \nabla\alpha_p \tag{2-32}$$

Where C_{td}, ρ_q and $\nabla\alpha_p$ are constant (=1), the density of the continuous phase and the disperse phase gradient, respectively. Simonin & Viollet (1990) linked the drift velocity with both disperse and continuous phase gradients. The final expression is given as

$$\boldsymbol{F}_{td,q} = -\boldsymbol{F}_{td,p} = C_{TD}K_{pq}\frac{D_{t,pq}}{\sigma_{pq}}\left(\frac{\nabla\alpha_p}{\alpha_p} - \frac{\nabla\alpha_q}{\alpha_q}\right) \tag{2-33}$$

Where $D_{t,pq}, K_{pq}$ and σ_{pq} represent the fluid-particulate dispersion tensor, exchange coefficient between phases and the Prandtl number (=0.75). The former tensor is associated with the turbulence model and equals to the turbulent kinematic viscosity of a mixture phase. The Burns et al. (2004) formulation is similar to the Simonin & Viollet model, however the authors calculated the dispersion tensor from the turbulent kinematic viscosity of the continuous phase instead of a mixture phase.

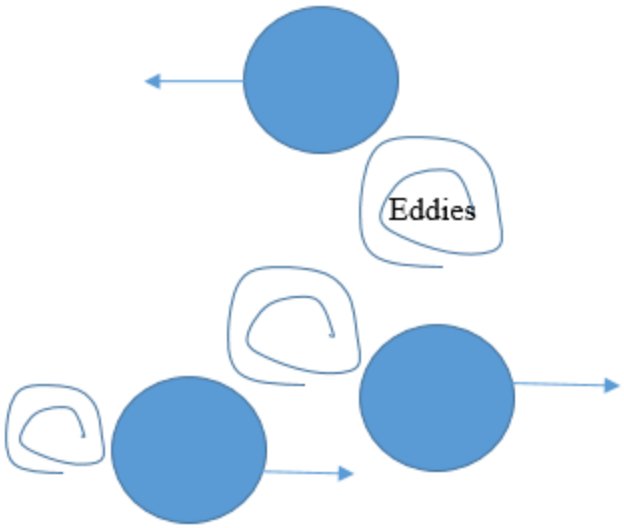

Fig. 2-4. Illustration of eddies interaction with the disperse phase

2.5 Turbulence Model in Multiphase System

Generally, flows become unstable above a critical Reynolds number ($=Ul/v$), which depends on the velocity, length scale of the flow (eddy size) and the kinematic viscosity. This instability introduces the turbulence in the system. The Reynolds number is the ratio of inertia (convective effects) and viscous forces. The flow is laminar if the Reynolds number is less than 2300 (for a pipe). Above this range, the flow is turbulent. This creates a random and chaotic behavior inside the system and a complete description of all random fluctuations are computationally costly. One of the possible ways to model turbulent flow, as shown in Fig. 2-5, is to decompose the velocity (u) into mean ($\bar{u}$) and the fluctuating component [$u'(t)$] as:

$$u = \bar{u} + u'(t) \tag{2-34}$$

Similarly, other transport equations for the pressure, energy, and species, denoted by ϕ, are defined as:

$$\phi = \bar{\phi} + \phi'(t) \tag{2-35}$$

In case of larger eddies, the convective effect is dominant while the viscous effect is negligible (Inviscid). However, for smaller eddies, the viscous effect is superior and viscosity defines the turbulence parameters. The length scale of small eddies is typically in the range of 0.1 to 0.01 mm with a 10 kHz frequency. These eddies transform the kinetic energy into thermal energy due to viscous dissipation.

The influence of turbulence on the Navier-Stokes equation is derived from the Reynolds equation. After performing the averaging operations and re-arrangements, the mean-momentum equation, also known as Reynolds-Averaged Navier-Stokes equation, is completed with a further addition of six stresses. These stresses are called turbulent stresses (or Reynolds stresses) containing three normal and three shear stresses. Likewise, these Reynolds stresses are added to other transport equations (species and energy) too and closure is needed for the unknown Reynolds stresses. One of the methods to correlate the Reynolds stresses to the mean velocity field is by using the turbulent viscosity. This technique is called the Boussinesq approach that is based on dimensional argument (Malalasekera & Versteeg 1995). The turbulent viscosity is the ratio of kinetic energy (k) and the dissipation rate of kinetic energy (ε) times a constant ($C_\mu = 0.09$) and a density and it is given by:

$$\mu_t = \rho C_\mu \frac{k^2}{\varepsilon} \tag{2-36}$$

One of the most commonly used models for kinetic energy and dissipation rate is a two-equation model, also known as a $k - \varepsilon$ model. The latter involves two partial differential equations: one for (k) and other for (ε). The standard $k - \varepsilon$ model is used in most of the industrial applications and generally performs well in a wide range of flow fields. However, the model does not capture the swirling flow due to curve boundary layer. Furthermore, the model assumes isotropic turbulence fields but in practical the flow is anisotropic. The standard $k - \varepsilon$ model has the following advantages and disadvantages:

Pros

- Easy to implement and requires only initial boundary conditions
- Most commonly used in engineering fields
- Model is well-developed and validated with literature data

Cons

- Computationally expensive due to the additional two equations
- The model is not suitable for large strains (swirling and rotational flows)
- Capturing the fully developed flow in a non-circular duct is limited

The deficiency of the standard model is addressed in the Renormalization model (RNG $k - \varepsilon$). In the latter, the k and epsilon are obtained by the following equations:

$$\frac{\partial(\rho_m k)}{\partial t} + \nabla.(\rho_m \boldsymbol{u}_m k) = \nabla.\left(\left(\mu_m + \frac{\mu_{t,m}}{\sigma_k}\right)\nabla k\right) + G_{k,m} - \rho_m \varepsilon \tag{2-37}$$

$$\frac{\partial(\rho_m \varepsilon)}{\partial t} + \nabla.(\rho_m \boldsymbol{u}_m \varepsilon) = \nabla.\left(\left(\mu_m + \frac{\mu_{t,m}}{\sigma_\varepsilon}\right)\nabla \varepsilon\right) + \frac{\varepsilon}{k}\left(C_{1\varepsilon} G_{\varepsilon,m} - C_{2\varepsilon}\rho_m \varepsilon\right) \tag{2-38}$$

The left-hand side of both equations involve unsteady and convective terms. The right-hand side of the equations include the diffusion, production and dissipation terms. The transport equations of RNG $k-\varepsilon$ model are similar to the Standard $k-\varepsilon$ model. However, the former contains the addition of strain rates in the dissipation term of the epsilon equation to model swirl/rotational flow.

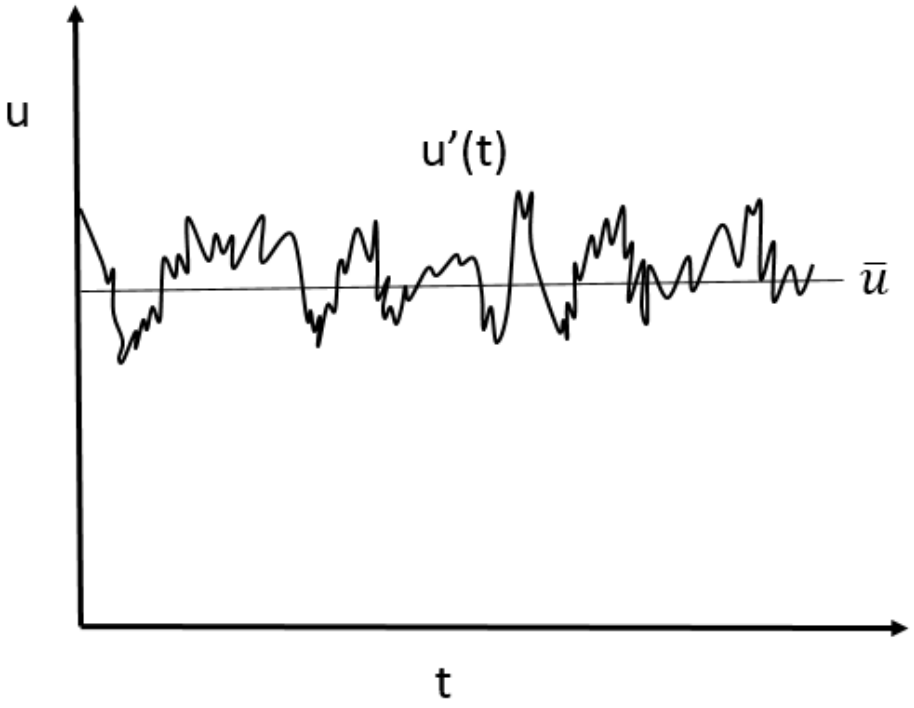

Fig. 2-5. Decomposition of the instantaneous velocity into mean and fluctuating components

2.6 Kinetic Theory of Granular Flows (KTGF)

As discussed earlier, the Eulerian framework assumes that the fluids are interpenetrating continua and that the fluid-fluid interaction defines the hydrodynamics behavior. This applies to particulate phase too, thus the accurate description of the solid interaction makes the system challenging. The momentum equation of solid phase, mentioned below, is slightly different from the gas and liquid phases since the closure involves the solid stress tensor ($\nabla\bar{\bar{\tau}}_s$).

$$\frac{\partial(\alpha_s \rho_s \boldsymbol{u_s})}{\partial t} + \nabla.(\alpha_s \rho_s \boldsymbol{u_s} \boldsymbol{u_s}) = -\alpha_s \nabla p - \nabla p_s + \nabla \bar{\bar{\tau}}_s + \alpha_s \rho_s \boldsymbol{g} + \boldsymbol{F}_{qs} \quad (2\text{-}39)$$

The solid stress tensor is modeled by three approaches: (a) empirical constant; (b) $k-\varepsilon$ model and (c) kinetic theory of granular flows (KTGF). The former computes the viscosity of the solid phase using a correlation that is a function of the solid loading and the phase fraction mainly (Farouk & Shah 1997; Troshko & Zdravistch 2009; Panneerselvam et al. 2009). This approach assumes that the solid is well dispersed (homogenous) inside the system and it is valid when the particle size is smaller than the bubble size. The implementation of this approach is simple, however it ignores the rheological behavior of the solid phase, for instance, the particle-particle interaction (Xu et al. 2014). In case of $k-\varepsilon$ model, the kinetic energy (k) corresponds to granular temperature and epsilon (ε) is linked to dissipation, which requires additional conservation equation (B.A & W.b Vanderheyden 1998). As a result, the particle turbulent viscosity is derived from the turbulence model. One of the drawbacks of this approach is that it ignores the particle-particle interaction, hence it is suitable only for a dilute system.

The KTGF approach is a closure model for the momentum equation of solid phase. This approach considers particle-particle interaction through effective solid pressure and the effective solid stress tensor, both of which are the function of a local granular temperature that corresponds to fluctuating component. Thus, KTGF approach predicts the local solid properties (particle pressure, viscosity and others). The effective solid shear stress is given by:

$$\bar{\bar{\tau}}_s = -P_s \bar{I} + 2\alpha_s \mu_s \left(\frac{1}{2}(\nabla \boldsymbol{u_s} + (\nabla \boldsymbol{u_s})^T)\right) + \alpha_s \left(\lambda_s - \frac{2}{3}\mu_s\right) \nabla.\boldsymbol{u_s} \bar{I} \quad (2\text{-}40)$$

Where $P_s, \bar{I}, \alpha_s, \mu_s \nabla \boldsymbol{u_s}$, and λ_s are the solid pressure, unit tensor, solid volume fraction, shear viscosity, velocity gradient of the solid phase and the bulk viscosity respectively. The solid pressure is calculated by:

$$p_s = \alpha_s \rho_s \Theta_s + 2\rho_s(1+e_{ss})\alpha_s{}^2 g_{0,ss} \Theta_s \quad (2\text{-}41)$$

Where Θ_s, e_{ss} and $g_{0,ss}$ are granular temperature, coefficient of restitution (=0.9) and radial distribution function. The latter is a function of the solid fraction and the maximum packing limit (=0.63). The solid shear stresses (solid viscosity) is the summation of collision ($\mu_{s,c}$), kinetic ($\mu_{s,k}$) and frictional viscosities ($\mu_{s,fr}$), as shown in Fig. 2-6. Depending on the solid volume fraction in the system, the solid viscosity is calculated locally and it is given as:

$$\mu_s = \mu_{s,c} + \mu_{s,k} + \mu_{s,fr} \tag{2-42}$$

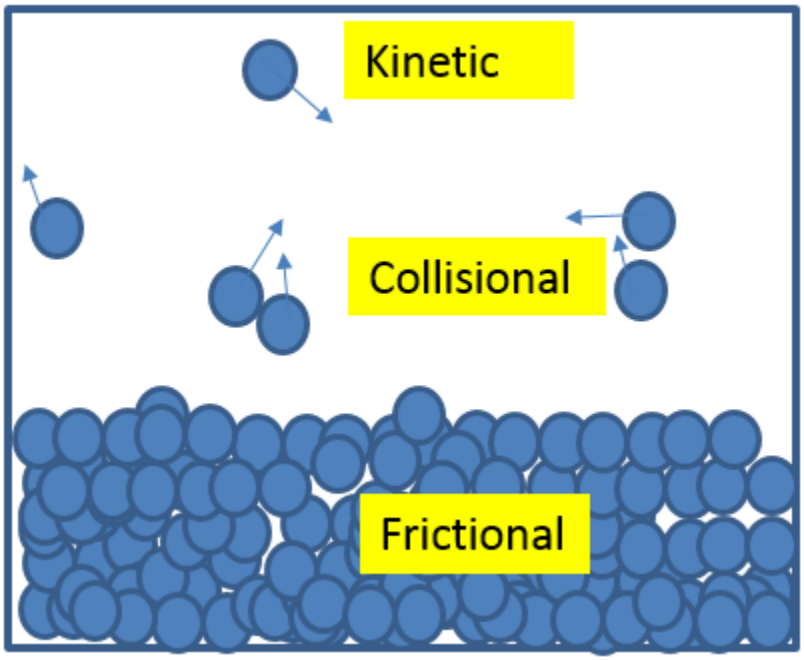

Fig. 2-6. Solid viscosity is calculated from the kinetic, the collision and the frictional viscosities

2.6.1 Collision Viscosity

Collision viscosity takes into account the collision of the solid particles. Syamlal et al. (1993) developed and proposed both the collision and kinetic viscosities and for further details, it is suggested to refer to Syamlal et al. (1993) technical document. The collision viscosity is given as:

$$\mu_{s,c} = \frac{4}{5}\alpha_s \rho_s d_s g_{0,ss}(1+e_{ss})\left(\frac{\Theta_s}{\pi}\right)^{1/2}\alpha_s \tag{2-43}$$

Here d_s and π represent the solid particle diameter and constant (=3.14159) respectively.

2.6.2 Kinetic Viscosity

The kinetic viscosity accounts for the particle translation and it is depended on solid phase fraction, particle size, granular temperature, the coefficient of restitution and radial distribution function. It is calculated using the following correlation as:

$$\mu_{s,k} = \frac{\alpha_s \rho_s d_s \sqrt{\Theta_s \pi}}{6(3-e_{ss})}\left[1+\frac{2}{3}(1+e_{ss})(3e_{ss}-1)\alpha_s g_{0,ss}\right] \tag{2-44}$$

2.6.3 Frictional Viscosity

If the volume fraction of the solid phase reaches nearby the maximum packing limit (=0.63), the frictional viscosity component is added into the solid viscosity. Schaefer (1987) proposed the frictional viscosity parameter, which is essentially derived from soil mechanics and described below as:

$$\mu_{s,fr} = \frac{p_s sin\phi}{2\sqrt{I_{2D}}} \tag{2-45}$$

Where ϕ and I_{2D} represent the angle of internal friction $(= 30^0)$ and second invariance of the deviatoric stress tensor respectively.

2.6.4 Bulk Viscosity

The bulk viscosity takes into account the resistance of the solid particles to compress and expand. Lun et al. (1984) studied the behavior of granular flows using inelastic and slightly inelastic particles and the proposed correlation is expressed as:

$$\lambda_s = \frac{4}{3}{\alpha_s}^2 \rho_s d_s g_{0,ss}(1 + e_{ss})\left(\frac{\Theta_s}{\pi}\right)^{1/2} \tag{2-46}$$

2.6.5 Granular Temperature

The granular temperature, which appears in the fluid-solid momentum equation (2-39), is correlated to the kinetic energy of the fluctuation component of the solid velocity and it is defined by:

$$\Theta_s = \frac{1}{3}{u_s}^2 \tag{2-47}$$

Where u_s is the fluctuating velocity of the instantaneous solid phase that is ensemble-averaged in time and space coordinates. The transport equation for the granular temperature (Θ_s) is taken from Ding Jianmin & Gidaspow (1990) work as:

$$\frac{3}{2}\left[\frac{\partial(\rho_s \alpha_s \Theta_s)}{\partial t} + \nabla.(\alpha_s \rho_s \boldsymbol{u}_s \Theta_s)\right] = \left(-p_s \bar{\bar{I}} + \bar{\bar{\tau}}_s\right): \nabla \boldsymbol{u}_s + \nabla.\left(k_{\Theta_s} \nabla \Theta_s\right) - \gamma_{\Theta_s} + \emptyset_{qs} \tag{2-48}$$

The first two terms on the left-hand side represent unsteady and convective terms. The terms on the right-hand side are the production of energy due to stress tensor, the diffusive flux of the granular energy, the rate of dissipation of energy due to the inelastic collision of particles and the

transfer of energy between phases. According to Syamlal et al. (1993) the diffusion coefficient (k_{Θ_s}) in the energy diffusion term is given by:

$$k_{\Theta_s} = \frac{15\alpha_s\rho_s d_s\sqrt{\Theta_s\pi}}{4(41-33\eta)}\left[1+\frac{12}{5}\eta^2(4\eta-3)\alpha_s g_{0,ss}+\frac{16}{15}(41-33\eta)\eta\alpha_s g_{0,ss}\right] \quad (2\text{-}49)$$

Where d_s and η are the diameter of solid particle and the restitution coefficient function.

2.7 Population Balance Model (PBM)

2.7.1 Framework

As discussed earlier that the real bubble columns involve the large spectrum of bubble sizes varying in space and time. The bubble size distribution influences the column behavior in term of hydrodynamics, heat and mass transfer, and thus has an important impact on the reactor's overall efficiency. For this reason, it is important to correctly quantify the bubble size distribution and one way to do it is by using population balance model.

The brief macroscopic framework of population balance is taken from the work of Jakobsen (2008). For more details related to the microscopic development of the population balance, see the published work of the Jakobsen. The population balance framework considers the evolution of the countable entities, for instance, bubbles, particles or droplets as a function of time, external and internal coordinates. The external coordinate (r) involves the actual physical-spatial coordinate whereas the internal coordinate (x) includes the abstract property space (example: bubble diameter or volume). The combination of both coordinates are often known as particle phase space. In general, the average number of bubbles per unit of particle space volume is of basic concern in most of the engineering fields. This number density function $f(x,r,t)$ could only change due to bubble coalescence and breakup phenomena and describes as:

The time rate for the change of number density in the particle phase space = Net generation of number density within the particle phase

In the mathematical terminology, it is given by:

$$\frac{D}{Dt}\int_{Vx(t)}\int_{Vr(t)} f\ dV_x dV_r = \int_{Vx(t)}\int_{Vr(t)} S\ dV_x dV_r \quad (2\text{-}50)$$

Where dV_x, dV_r *and* S are the infinitesimal volume of internal coordinate, infinitesimal volume of external coordinate and the source term representing the bubble birth and death. The notations in the above equation are simplified as $\int_{Vx(t)} \int_{V(t)} = \int_{V(t)}$ and $dV_x dV_r = dV$ and the equation is re-written as:

$$\frac{D}{Dt} \int\limits_{V(t)} f \, dV = \int\limits_{V(t)} S \, dV \tag{2-51}$$

The control volume system (eq. 2-51) is converted into the Eulerian framework using the Reynolds theorem as:

$$\frac{D}{Dt} \int\limits_{V(t)} f \, dV = \frac{\partial f}{\partial t} \int\limits_{V(t)} f \, dV + \int\limits_{A(t)} (\boldsymbol{v} f).n \, dA \tag{2-52}$$

Where $\boldsymbol{v}, dA$ and n represent the combined phase velocity ($\equiv vx + vr$), combined surface area ($\equiv Ax + Ar$), and combined normal vector ($\equiv nx + nr$) respectively. In equation (2-52), the surface integral is transformed into a volume integral using the Gauss divergence theorem, which is given as:

$$\int\limits_{A(t)} (\boldsymbol{v} f).n \, dA = \int\limits_{V(t)} \nabla.(\boldsymbol{v} f) \, dV \tag{2-53}$$

Substituting equations (2-52) and (2-53) into the equation (2-51) that can be re-written as:

$$\int\limits_{V(t)} \left(\frac{\partial f}{\partial t} + \nabla.(\boldsymbol{v} f) - S \right) dV = 0 \tag{2-54}$$

Since the combined volume V is valid for all sizes, the integrand vanishes. Hence the differential form of population balance equation is written as:

$$\frac{\partial f}{\partial t} + \nabla.(\boldsymbol{v} f) = S \tag{2-55}$$

The above equation could be written in term of both convective (external coordinate) and growth (internal coordinate) as:

$$\frac{\partial f}{\partial t} + \nabla.(\boldsymbol{v_r} f) + \nabla.(\boldsymbol{v_x} f) = S \tag{2-56}$$

In the absence of mass transfer, bubble growth and reactions, the number density function for each bubble class (n_i) is described as:

$$\frac{\partial}{\partial t} n_i + \nabla . (\boldsymbol{u}_b n_i) = S \tag{2-57}$$

The population balance equation consists of a transient, convective, and source terms. The latter contains the breakage (S_b) and coalescence (S_c) of bubbles. The local gas volume fraction (or holdup) is:

$$\alpha_g = \sum_{i=1}^{N} n_i \frac{\pi}{6} d_i^3 \tag{2-58}$$

The source term (S_b and S_c) is described as:

$$S_b = \int_v^\infty m(v)\, \beta(v, v') \Omega_B(v') n_i(v') dv' - \Omega_B(v) n_i(v) \tag{2-59}$$

$$S_c = \frac{1}{2} \int_0^v \Omega_C\, (v - v', v') n_i(v - v') n_i(v') dv' - \int_0^\infty \Omega_C(v, v') n(v) n(v')\, dv' \tag{2-60}$$

In equation (2-59), the first term shows the production of daughter bubbles v from v' due to breakage and the second term represents the death of v during the breakup process. In equation (2-60), the first term shows the production of a coalesced bubble v from v' and v-v' and the second term is the death of v. The terms $m(v), \beta(v, v'), \Omega_B(v'), and\ \Omega_C(v, v')$ represent the number of daughter bubbles (=2), the daughter size distribution, breakup rate and coalescence rate. These terms need to be solved to close the population balance equation. The physical model of bubble coalescence involves collision frequency and coalescence efficiency. The collision frequency is defined by number of mechanisms:

1. Turbulent based induced collisions (Chung-Hur Lee 1987; Prince & Blanch 1990; Luo 1993)
2. Velocity gradient based induced collision (Prince & Blanch 1990)
3. Bubbles trapped in a turbulent-eddy (Chesters 1991)
4. Buoyancy force induced collision (Prince & Blanch 1990)
5. Wake entrainment (Wu et al. 1998)

Similarly, the coalescence efficiency involves the following mechanisms:

1. Energy model (Howarth 1964)

2. Critical velocity model (Lehr et al. 2002)
3. Film drainage (Chung-Hur Lee 1987; Prince & Blanch 1990; Chesters 1991; Luo 1993)

The details of each model is well explained in the published data of Liao & Lucas (2010). Chen et al. (2005) studied a different combination of the bubble coalescence models and concluded no significant influence. Bubble coalescence model proposed by Luo (1993) is extensively used in the open literature, the details of this model is explained in the next chapters. Also, in the Ansys-Fluent v.17.2 software the Luo model is available.

The mechanisms of the binary bubble breakage for the gas-liquid system are divided into following categories:

1. Breakup due to eddies collision (Chung-Hur Lee 1987; Prince & Blanch 1990; Luo & Svendsen 1996; Martinez-Bazan et al. 1999b; Lehr et al. 2002)
2. Viscous shear stress (Kocamustafaogullari & Ishii 1995)
3. Shearing-off (Fu & Ishii 2002)
4. Interfacial instability (Wang et al. 2005)

For details of each model, the reader is suggested to refer to Liao & Lucas (2009) work. Bubble breakup due to eddy bombardment is most significant as compared to other mechanisms, which have a negligible effect and are ignored often. The breakup models proposed by Luo & Svendsen (1996) and Lehr et al. (2002) require no daughter size distribution as an input parameter that makes implementation of these models easy. Luo & Svendsen considered the U-shape daughter distribution (i.e. making extremely small and large fragments). One of the drawbacks of this model is that it makes too many small bubbles in the system and the equal sized fragments are not possible, also the shape of the distribution is not dependent on the parent bubble size. In case of the Lehr, the shape of the daughter size distribution depends on the parent's bubble size. For the small bubbles, the authors observed monomodal distribution and for the large bubbles, the bimodal distribution was reported. In this work, the focus is made on both breakup models (Luo & Svendsen 1996; Lehr et al. 2002), which are not extensively studied in the open literature especially in case of a three-phase system.

2.8 The Binary Bubble Coalescence Kernel

According to Luo (1993), the coalescence kernel $B_{C,i}$ is defined as the summation of all coalescence event giving birth to bubbles of size (d_i) as:

$$B_C(i) = \sum_{d_j=d_{min}}^{d_i/_2} \Omega_C(d_j: d_i - d_j) \tag{2-61}$$

Where d_{min} is the minimum bubble size that depends on the minimum eddy size occurring in the system. The bubble of size (d_j) coalesce with bubble of size $(d_i - d_j)$ to produce bubble of size (d_i). The upper limit $(d_i/2)$ is the symmetry assumption to avoid counting the coalescence of the same pair of bubble size twice. Similarly, $D_{C,i}$ of bubble size (d_i) is given as:

$$D_C(i) = \sum_{d_j=d_{min}}^{d_{max}-d_i} \Omega_C(d_j: d_i) \tag{2-62}$$

Where (d_{max}) is the maximum size of the bubble present in the system.

Luo (1993) proposed that the coalescences rate $\Omega_C(d_j: d_i)$ of two bubbles in a liquid medium that includes three basic steps (see Fig. 2-7). First, the bubbles collide and as a result, a small liquid film is trapped between them. Then, the trapped liquid tends to drain out until that separating liquid film between bubbles reaches a critical thickness. Third, the thin layer of liquid raptures and the two bubbles coalesce. Mathematically, the collision of bubbles and the contact time to rapture the thin layer of liquid are examined by collision frequency and probability function. Therefore, the binary bubble coalescence rate is the product of the collision frequency $\omega_C(d_i: d_j)$ and coalescence efficiency $p_C(d_i: d_j)$. The binary coalescence phenomenon $'\Omega_C(d_i: d_j)'$ between two bubbles (.i.e. d_i and d_j) is given as:

$$\Omega_C(d_i: d_j) = \omega_C(d_i: d_j) p_C(d_i: d_j) \tag{2-63}$$

The collision frequency and coalescence efficiency are complex functions and depend on the drop or bubble density, size distribution and flow behavior of the continuous phase. For instance, increasing the velocity (gas or liquid) tends to increase the collisions frequency and eventually the coalescence rate. However, such an increase in velocity provides enough energy for bubbles to

rebound before coalescence occurs. As a result, the coalescence efficiency decrease as well as the coalescence rate. The details of collision frequency and coalescence efficiency are described in the next subsections.

2.8.1 Bubble-Bubble Binary Collision Frequency

Luo's model considered the collision frequency as a function of the turbulent collision only. Turbulent collision happens due to the random motion of bubbles in the system. However, a simplification (isotropic turbulent) is made in order to determine the mean relative velocity between bubbles in turbulent collision. The collision frequency is given as:

$$\omega_C(d_i : d_j) = \frac{\pi}{4}(d_i + d_j)^2 n_i n_j \overline{u}_{ij} \tag{2-64}$$

Where

$$\overline{u}_{ij} = \left(\overline{u}_i^2 + \overline{u}_j^2\right)^{1/2} = \overline{u}_i\left(1 + \xi_{ij}^{-2/3}\right)^{1/2} \tag{2-65}$$

Here ξ_{ij} is the bubble size ratio of d_i/d_j and $\overline{u_i}$ is the mean bubble velocity. The latter is calculated from the mean turbulent velocity below as:

$$\overline{u_t} = \left(\frac{8\overline{u^2}}{3\pi}\right)^{1/2} = \left(\frac{8\tilde{\beta}}{3\pi}\right)^{1/2} = \beta^{1/2}(\varepsilon\lambda)^{1/3} \tag{2-66}$$

Where β and λ are the constant (equals 2) and the eddy size, respectively. The latter is substituted by the bubble diameter of size $d_i \; or \; d_j$.

2.8.2 Bubble-Bubble Binary Coalescence Efficiency

The coalescence efficiency (coalescence probability) predicts the possibility for two interacting bubbles to coalesce when coming in contact with each other. It is the ratio of coalescence time (t_C) to contact time (t_I). When t_I is greater than t_C, the liquid film between bubbles reaches the critical rupture thickness and hence, the coalescence process occurs. The coalescence efficiency is defined by:

$$p_C = exp\left(-\frac{t_C}{t_I}\right) \tag{2-67}$$

$$t_C \simeq 0.5\frac{\rho_L \overline{u}_{ij} d_i^2}{\left(1+\xi_{ij}\right)^2 \sigma} \tag{2-68}$$

$$t_I \simeq 2t_{max} = (1+\xi_{ij})\sqrt{\frac{(\rho_G/\rho_L+\gamma)}{3\left(1+\xi_{ij}^2\right)(1+{\xi_{ij}}^3)}\frac{\rho_L d_i^3}{\sigma}} \tag{2-69}$$

Where $\rho_L, \overline{u}_{ij}, \sigma\ \gamma$ are the liquid density, turbulent relative velocity, surface tension and virtual mass coefficient, respectively. Substituting t_C and t_I in equation (2-67) as:

$$p_C = exp\left\{-c_1\frac{\left[0.75\left(1+\xi_{ij}^2\right)(1+{\xi_{ij}}^3)\right]^{1/2}}{(\rho_G/\rho_L+\gamma)^{1/2}(1+{\xi_{ij}}^3)}We_{ij}^{1/2}\right\} \tag{2-70}$$

Where the Weber number is defined as

$$We_{ij} = \frac{\rho_L d_i \overline{u}_{ij}^2}{\sigma} \tag{2-71}$$

2.9 Binary Bubble Breakup Kernel

The breakup kernel $B_B(i)$ is defined as the summation of all the events giving birth to bubble size (d_i) such as:

$$B_B(i) = \sum_{d_j=d_i}^{d_{max}} \Omega_B\left(d_j{:}\, d_i\right) \tag{2-72}$$

The death of bubble with size (d_i) due to breakup is given as:

$$D_B(i) = \Omega_B(d_i) \tag{2-73}$$

Luo & Svendsen (1996) breakup rate '$\Omega_B\left(d_j{:}\, d_i\right)'$ of bubbles is the product of eddy-bubble collision $\omega_B(d_{i,}\lambda)$ and breakage efficiency $p_B(d_i{:}\, d_j, \lambda)$. The individual breakup rate of mother size bubble d_i into a daughter size bubbles (d_j) is depicted as:

$$\Omega_B\left(d_i{:}\, d_j\right) = \int_{\lambda_{min}}^{d_i} \omega_B(d_{i,}\lambda)\ p_B(d_i{:}\, d_j, \lambda)d\lambda \tag{2-74}$$

The upper integration limit states that the bubble breakage occurs only when the eddy size is less than or equals to the bubble diameter ($\lambda \leq d_i$).

2.9.1 Eddy-Bubble Collision

The arrival eddies (see Fig. 2-8), which are smaller or equal to the bubble size tend to break the bubble into two fragments, whereas the larger eddies do not induce bubble breakage process and only disperse the bubbles. The eddy-bubble collision $\omega_B(d_i,\lambda)$ is given as:

$$\omega_B\left(d_i,\lambda\right) = \frac{\pi}{4}(d_i+\lambda)^2\overline{u}_\lambda n_i \dot{n}_\lambda \tag{2-75}$$

Here $\dot{n}_\lambda$ denotes the number of eddies per reactor volume (or number density of eddies) with size between λ and $\lambda + d\lambda$, whereas $\overline{u}_\lambda$ is the turbulent velocity calculated from equation (2-66). The number density of eddies $\dot{n}_\lambda$ is calculated from the energy spectrum E (k), and it is given as:

$$\dot{n}_\lambda = \frac{c_2(1-\varepsilon_G)}{\lambda^4} \tag{2-76}$$

Where c_2 is a constant equals 0.841. Substituting equations (2-66) and (2-76) into the eddy-bubble collision equation (2-75), allows it to be written as:

$$\omega_B\left(d_i,\lambda\right) = \frac{\pi}{4}(d_i+\lambda)^2\beta^{1/2}(\varepsilon\lambda)^{1/3}c_2\frac{(1-\varepsilon_G)}{\lambda^4} \tag{2-77}$$

In dimensionless variable, the above equation of eddy-bubble collision is written as:

$$\omega_B(\xi) = c_3(1-\varepsilon_G)n_i(\varepsilon d_i)^{\frac{1}{3}}\frac{(1+\xi)^2}{d_i^2\xi^{\frac{11}{3}}} \tag{2-78}$$

Where $\xi = \lambda/d_i$ and c_3 equals 0.923.

2.9.2 Breakage Efficiency (Probability)

The breakup efficiency (probability) is the closure for the breakage rate equation (2-74). The arriving eddies hitting the mother bubble of size d_i tend to break-up the bubble into binary fragments d_j (daughter bubble sizes). The probability of this breakage depends on the energy confined in the arrival eddies and the minimum energy needed to overcome the increase of the surface area due to the bubble fragmentation. Mathematically, the expression is written as:

$$e(d_i,\lambda) \geq e_s\left(d_i,d_j\right) \tag{2-79}$$

Where $e(d_i,\lambda)$ represents the kinetic energy of the arrival eddy of size λ to break the bubble size (d_i), whereas $e_s\left(d_i,d_j\right)$ describes the increase of bubble surface energy needed to break the mother bubble size into bubble fragments. The break-up probability is given by:

$$p_B(d_i : d_j, \lambda) = exp(-\chi_c) \tag{2-80}$$

Where

$$\chi_c = \frac{e_s(d_i, d_j)}{\bar{e}(d_i, \lambda)} = \frac{3C_f \pi \sigma}{2\beta \rho_c \varepsilon^{2/3} d_i^{5/3} \xi^{11/3}} \tag{2-81}$$

Where $\chi_c, C_f, \sigma, \beta, \varepsilon$ and ξ are the critical dimensionless energy ratio, increase coefficient of surface area, surface tension, constant (=2), energy dissipation rate and dimensionless ratio ($= \lambda/d_i$), respectively. Substituting equations (2-78) and (2-80) into the breakup rate equation (2-74) leads to the following equation:

$$\Omega_B(d_i : d_j) = c_3(1 - \varepsilon_G) n_i (\varepsilon/d_i^2)^{\frac{1}{3}} \int_{\xi_{min}}^{1} \frac{(1+\xi)^2}{\xi^{\frac{11}{3}}} \exp\left(-\frac{3C_f \pi \sigma}{2\beta \rho_c \varepsilon^{2/3} d_i^{5/3} \xi^{11/3}}\right) d\xi \tag{2-82}$$

The minimum size of eddies in inertia subrange is $\xi_{min} = \lambda_{min}/d_i$, , $\lambda_{min} = (11.4 \sim 31.4) * \left(\frac{\mu^3}{\varepsilon}\right)^{\frac{1}{4}}$.

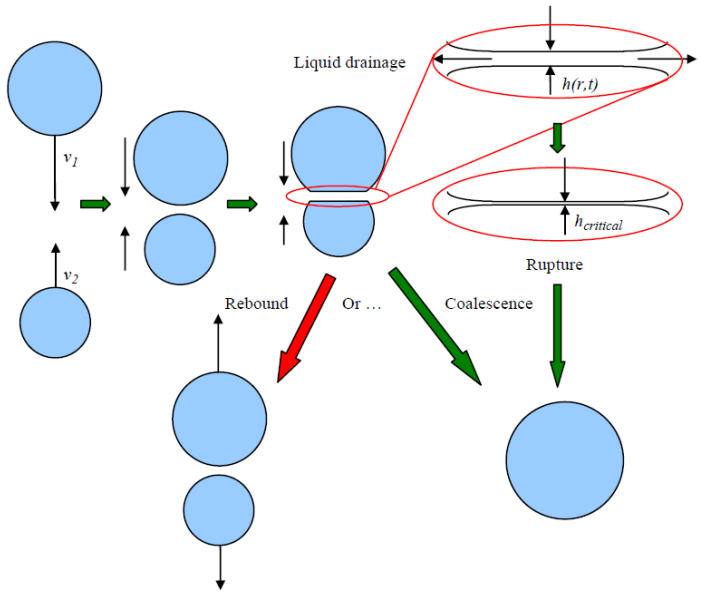

Fig. 2-7. Illustration of Luo's bubble coalescence mechanism (Chen et al. 2005)

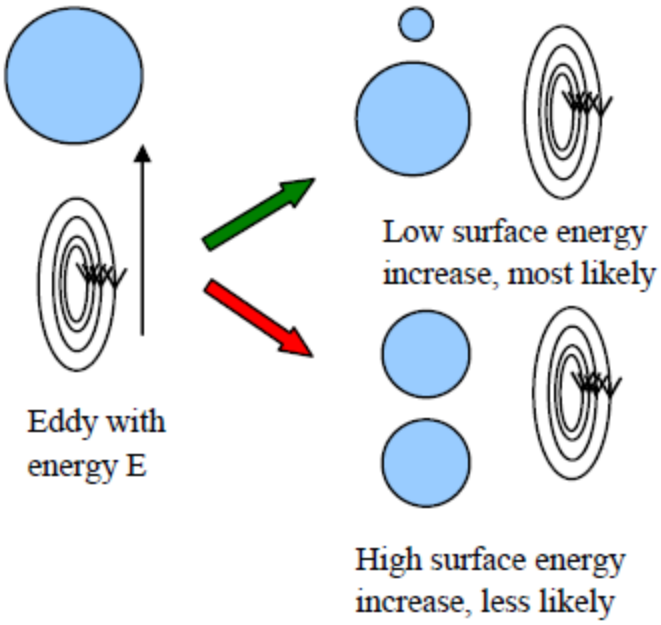

Fig. 2-8. Illustration of Luo & Svendsen break-up process (Chen et al. 2005)

Fig. 2-8. Luo & Svendsen breakup model predicted that the arrival eddies, which are equal and less than parent bubble size, break the bubble into small and large fragments (unequal-sized). Furthermore, these fragments have low interfacial area and ultimately a lower surface energy. Therefore, the possibility for the arriving eddies to overcome this resultant surface energy of unequal sized bubbles is higher. Hence, the daughter bubble size distribution should be U-shaped. The possibility of equal-sized bubble fragments is low because Luo model considered that eddies size larger than the bubble size tend to transport the bubbles rather than breaking it.

Lehr et al. (2002) investigated the binary breakage of a bubble in a pseudo-homogeneous and turbulent flow fields and developed a breakup model similar to Luo & Svendsen model. However, the Lehr calculated the breakage possibility from interfacial force of the bubble surface and inertial force of the arrival eddies. Both forces balance each other and are defined as:

$$d_{max} = 2^{1/5} \frac{\sigma^{3/5}}{\rho_q^{3/5} \varepsilon^{2/5}} \tag{2-83}$$

Where d_{max} is the maximum stable bubble size. The Lehr breakup rate is given as:

$$\Omega_B(d_i:d_j) = \frac{1.19\sigma}{\rho_l \varepsilon^{1/3} d_i^{7/3} f^{1/3}} \int_{\xi_{min}}^{1} \frac{(1+\xi)^2}{\xi^{\frac{13}{3}}} exp\left(\frac{2\sigma We_{crit}}{\rho_l \varepsilon^{2/3} d_i^{5/3} f^{1/3}} \xi^{-2/3}\right) d\xi \qquad (2\text{-}84)$$

Where $f \; and \; We_{crit}$ represent the volume fraction of daughter bubble $\left(= d_j/d_i\right)^3$ and constant (=0.1).

2.10 Discretizing Population Balance Equations using Class Method

In literature, population balance equations (PBE) are discretized using the class (bin) method (Kumar & Ramkrishna 1996), the Monte Carlo method (Smith & Matsoukas 1998), the quadrature method of moments (QMOM) (McGraw 1997), the direct quadrature method of moments (DQMOM) (Fan et al. 2004), the extended quadrature method of moments (EQMOM)(Yuan et al. 2012) and the least square method (LSM) (Zhu et al. 2009). The details of each discretizing scheme are well explained in the work of Ramkrishna (2000), Selma et al. (2010) and Yeoh et al. (2014).

The bubble class method assumes a fixed pivotal grid over which the bubbles are distributed. The formation of bubble of size (v) due to breakup/coalescence, is divided into a number of intervals and each interval is assigned to a pivot volume/grid points (x_i) to calculate the total number of bubbles of size i per unit volume (N_i). If the bubble volume is not equal to the pivot volume, the bubbles are assigned to the closest pivot size to ensure the conservation of bubble mass and numbers. After applying the algebraic formulations and rearrangement, the population balance equation (eq. 2-57) is written in discretized form as:

$$\begin{aligned} &\frac{\partial}{\partial t} N_i + \nabla.(\boldsymbol{u}_b N_i) \\ &= \sum_{k=0}^{n} \sum_{j=0}^{n} \left[\theta\left(x_{i-1} < (x_j + x_k) < x_i\right)\left(1 - \frac{1}{2}\delta_{j,k}\right)\right] \eta \, \Omega_C N_j N_k \\ &+ \sum_{k=0}^{n} \sum_{j=0}^{n} \left[\theta\left(x_i < (x_j + x_k) < x_{i+1}\right)\left(1 - \frac{1}{2}\delta_{j,k}\right)\right] \eta \, \Omega_C N_j N_k \\ &- N_i \sum_{k=0}^{n} \Omega_C N_k + \sum_{k=i}^{n} \pi_{i,k} \Omega_B N_k - \Omega_B N_i \end{aligned} \qquad (2\text{-}85)$$

And

$$\pi_{i,k} = \int_{x_{i-1}}^{x_i} \frac{v - x_{i-1}}{x_i - x_{i-1}} m_v dv + \int_{x_i}^{x_i+1} \frac{x_{i+1} - v}{x_{i+1} - x_i} m_v dv \tag{2-86}$$

Where j and k are bubble class indexes, and θ is a test function and defined as

$$\theta = \begin{cases} 0, false \\ 1, true \end{cases} \tag{2-87}$$

The conservation of numbers and mass (η) is given as:

$$\eta = \begin{cases} \dfrac{x_{i+1} - v}{x_{i+1} - x_i}, x_i \leq v \leq x_{i+1} \\ \dfrac{v - x_{i-1}}{x_i - x_{i-1}}, x_{i-1} \leq v \leq x_i \end{cases} \tag{2-88}$$

Where v equals $(x_j + x_k)$, The Kronecker delta $(\delta_{j,k})$ avoid counting the same coalescence event twice and is defined as:

$$\delta_{j,k} = \begin{cases} 0 & i \neq j \\ 1 & i = j \end{cases} \tag{2-89}$$

2.11 Numerical Solvers

The numerical solvers involve Pressure-based and Density-based solvers. Generally, the former is suitable for the incompressible flows and the latter for compressible flows. In the pressure-based solver, the pressure fields are obtained from continuity and momentum equations. The other scalar variables (turbulence, energy, species, and others) in the control-volume technique are obtained by following steps:

- Dividing the domain into discrete control volume (called grid/mesh).
- Integration of the governing equations over each control volume in order to obtain the algebraic equation for each variable.
- Linearization of the algebraic discrete equations

The pressure-based solver consists of Segregated and Coupled algorithms. The former solves each variable (temperature, pressure, velocity, and others) one after another. The latter algorithm solves all variable together. The solution procedure for both algorithms are shown in Fig. 2-9.

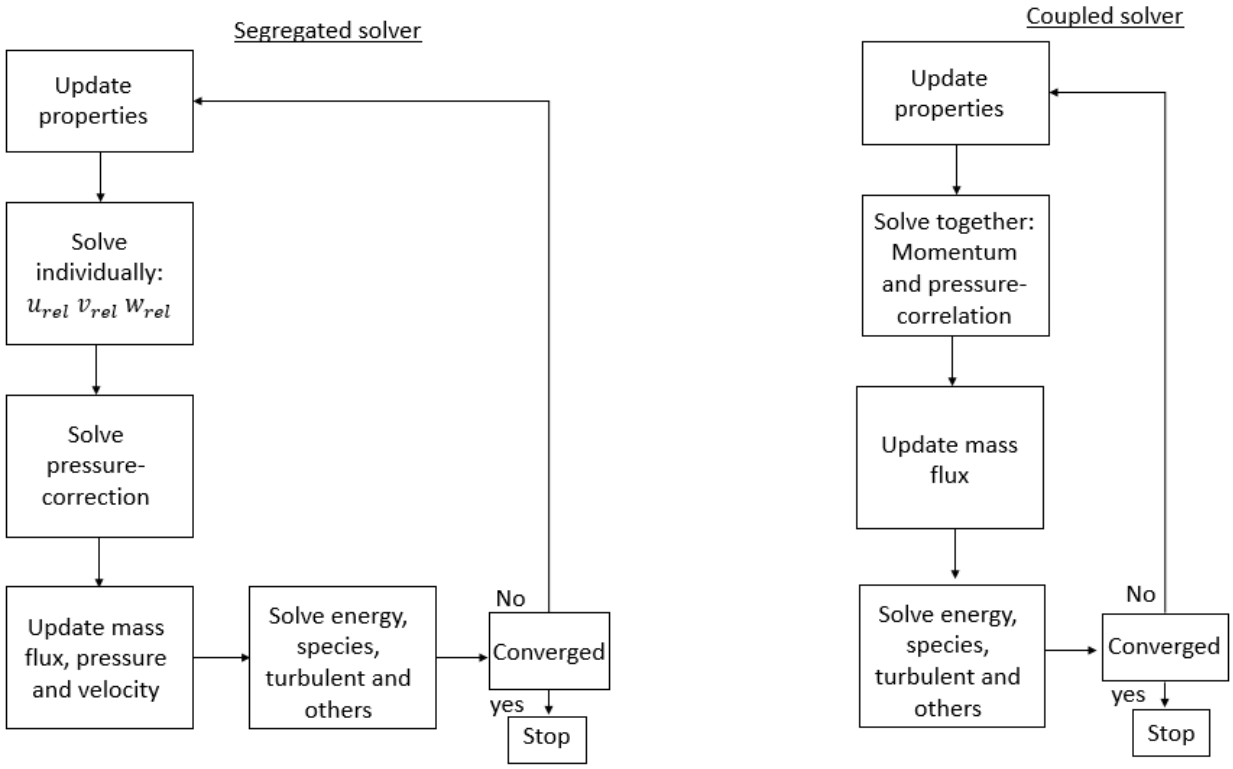

Fig. 2-9. Solution procedure for segregated and coupled solvers (Ansys 2016a)

The transport equations are integrated over the cell volume and converted into algebraic discrete equations, which are given as:

$$\int_v \frac{\partial \rho \emptyset}{\partial t} dV + \oint \rho \emptyset \boldsymbol{u}. d\boldsymbol{A} = \oint \Gamma_\emptyset \nabla \emptyset. d\boldsymbol{A} + \int_v S_\emptyset dV \tag{2-90}$$

Where $\rho, \emptyset$, V, $\boldsymbol{u}, \boldsymbol{A}, \Gamma_\emptyset$ and $S_\emptyset$ are density, scalar quantities, control volume (cell volume), velocity vector, surface area vector, diffusion coefficient for the scalar quantity, and source term respectively. The discretize form of eq.(2-90 is given by:

$$\frac{\partial \rho \emptyset}{\partial t} dV + \sum_f^{N_{faces}} \rho_f \boldsymbol{u}_f \emptyset_f . \boldsymbol{A}_f = \sum_f^{N_{faces}} \Gamma_\emptyset \nabla \emptyset_f . \boldsymbol{A}_f + S_\emptyset V \tag{2-91}$$

Where N_{faces}, $f, \emptyset_f, \rho_f \boldsymbol{u}_f . \boldsymbol{A}_f, \boldsymbol{A}_f, \nabla \emptyset_f$ and V represent number of faces in a cell, face, convection of scalar quantity via face, mass flux via face, area of face, gradient of quantities at the face and volume of the cell respectively. The first term '$(\partial \rho \emptyset)/\partial t$ dV' in the eq. (2-91 is temporal discretization. The scalar values ∅ are stored at the centre of the cell, however for the convective and diffusive terms face values of the ∅ are required, which can be accomplished by interpolating

the center value to the face value (also called upwind). This interpolation can be achieved by first order upwind scheme, second order upwind scheme, power law, QUICK scheme and others. In the first order upwind scheme, the cell face values are assumed to be similar to cell center value. The second order scheme computes the cell face values using a multidimensional linear reconstruction approach (i.e. Taylor series). For the power law, face value is calculated by a one-dimensional convection-diffusion equation. The QUICK scheme is similar to second order upwind scheme, however, the face values are weighted average. Jakobsen (2003) studied the influence of the numerical schemes and reported the numerical diffusion at elevated velocity when using the low order schemes. The author suggested to use the high order schemes in order to avoid the numerical dependency on the solution.

2.12 Previous Studies on the Two-Phase Flow

Computational fluid dynamics (CFD) have been used by numerous authors to simulate the hydrodynamics of bench and industrial-scaled bubble columns, operating from homogeneous to heterogeneous regimes. Some of the most important studies involved in the Eulerian framework are discussed in this section.

Krishna et al. (1999) conducted both the experiments and the 2D-axisymmetric simulations to study the influence of scale-up on the hydrodynamics of air-water bubble column. The operated superficial gas velocities were in the range of 0.02 m/s to 0.35 m/s, covering the homogeneous and heterogeneous regimes while the column diameter was varied from 0.38 m to 0.63 m. The Authors treated the small bubbles, large bubbles, and the water phase as an individual fluid and solved the three-fluid model. The proposed drag coefficient (C_D) was based on the bubble rise velocity of small and large bubbles and is defined as:

$$C_D = \frac{4}{3}\frac{\rho_L - \rho_G}{\rho_L} g d_b \frac{1}{V_b^2} \tag{2-92}$$

Where $(\rho_L - \rho_G), g, d_b \; and \; V_b$ represent density difference between air and liquid phases, gravitational force, bubble diameter, and bubble rise velocity, respectively. The latter is defined as:

$$V_{b,small} = 1.53 \left(\frac{\sigma g}{\rho_L}\right)^{0.25} \tag{2-93}$$

$$V_{b,large} = 0.71\sqrt{gd_{b,large}}\,(SF)(AF) \tag{2-94}$$

Where σ, $V_{b,small}$, $V_{b,large}$, AF, and SF represent surface tension, bubble rise velocity (small bubble), bubble rise velocity (large bubble), the acceleration factor, and the scale correction factor, respectively. AF and SF account for fluid viscosity and column diameter effects. The predicted radial profiles and total gas holdup were in good agreement with the experimental values, however the authors considered no interaction between small and large bubbles. Krishna et al. (2000) continued this work and performed a 2D-axisymmetric and 3D simulations using air-water and air-Tellus oil systems. They concluded that the time-averaged radial profiles of the liquid axial velocity and gas hold in 2D and 3D were close to each other. Furthermore, the assumption of small and large bubbles to simulate the heterogeneous regime showed a similar trend with empirical values, although not sufficient enough to correctly predict the gas void fraction.

Pfleger et al. (1999) performed both the experiments and the CFD-simulations to study the influence of a turbulence model in an air-water rectangular column. The inlet geometry involved 8 holes placed in a rectangular configuration while the static bed height was at 0.45 m. The interphase momentum transfer consisted of drag forces only. The authors compared the predicted radial profiles of axial liquid velocity and the turbulent kinetic energy with the empirical profiles and suggested that even for a diluted system (gas holdup below 2%), the inclusion of a turbulent model allows predicting better results. Pfleger & Becker (2001) simulated a 3D bubble column using a modified k-epsilon turbulence model. The k-epsilon model was solved for a liquid phase and the influence of a disperse phase was accounted by a bubble-induced turbulence source term. They concluded that the modified k-epsilon model improves the time-averaged radial profile of axial liquid velocity but on the other side, deteriorates the gas holdup profile when compared with experiments. Furthermore, the mesh sensitivity analysis results showed that the decrease in mesh size improved the predicted time-averaged gas holdup profile when compared to the empirical profile. However, this fine mesh predicts a flatter profile of axial liquid velocity, which was inconsistent with the experiments.

Olmos et al. (2001) implemented the population balance model (PBM) to simulate the hydrodynamics of a bubble column. The source terms in the PBM involved the Prince & Blanch (1990) bubble coalescence model and the Luo & Svendsen (1996) bubble breakup model. Furthermore, the experimental setup consisted of laser doppler velocimetry, an optical probe, and

photography to measure the axial liquid velocity, gas holdup, and bubble size distribution. The superficial gas velocity (Ug) was varied from 0.005 m/s to 0.096 m/s in a 0.01 m diameter column. The simulations were performed using 2D-axisymmetric geometry. PBM was discretized using bubble class method, and single momentum equation was solved for all the bubble sizes. In general, the predicted gas holdup and axial liquid velocity profiles were in good agreement as compared with experiments, however at Ug >0.08 m/s, the discrepancy in the radial profile of gas holdup was observed.

Buwa & Ranade (2002) studied the influence of inlet configurations, which involved perforated and sintered plates. The former plate configuration consisted of 8 holes that were varied from 0.8 mm to 2 mm. The pitch was also varied in the range of 6 mm to 12 mm. The experimental setup consisted of a rectangular bubble column, which was similar to the one reported in Pfleger et al. (1999) work. The interphase momentum transfer involved drag, lift, and virtual mass forces. The results showed that the different inlet configurations had no significant influence on the oscillation of the bubble plume. Buwa et al. (2006) used this rectangular column to study the influence of the lift force. Overall, the results showed that the time-averaged radial profiles of axial liquid velocity and gas holdup improved as compared with experiments following the inclusion of lift force. However, at 0.0014 m/s the gas holdup was over-predicted.

Chen et al. (2005) simulated an air-water bubble column using 2-dimensional axisymmetric geometry and studied the effect of different breakup and coalescence closures. The latter included the Prince & Blanch (1990), Chesters (1991) and Luo (1993) models, whereas the breakup kernel involved the Martinez-Bazan et al. (1999a and 1999b) and Luo & Svendsen (1996) models. The Chen increased all the breakup rates by a factor of 10. The population balance equations (PBE) were discretized using a bubble class method and the interphase momentum transfer included the drag force only. The Chen compared the CFD-simulations with a wide range of experimental data involving column diameters of 0.14 m, 0.19 m and 0.44 m as well as superficial gas velocities ranging from 0.02 m/s to 0.1 m/s. In Fig. 2-10, the authors showed no significant difference when comparing the different combination of breakup and coalescence kernels with experimental results. Furthermore, they concluded that the 2D-axisymmetric simulations could predict a time-averaged radial profiles of gas holdup and axial liquid velocity operated at homogeneous and heterogeneous regimes. However, the authors reported an unrealistic “hump” in the gas holdup

profile, which might be related to a constraint in the lateral movement of the disperse gas imposed by axisymmetric assumption. Ekambara et al. (2005) simulated the bubble column using 1D, 2D, and 3D geometries. The authors reported that 2D and 3D simulations predicted good agreement with empirical values for the time-averaged radial profiles of the gas holdup and axial liquid velocity. The authors did not report a "hump" in the gas holdup profile.

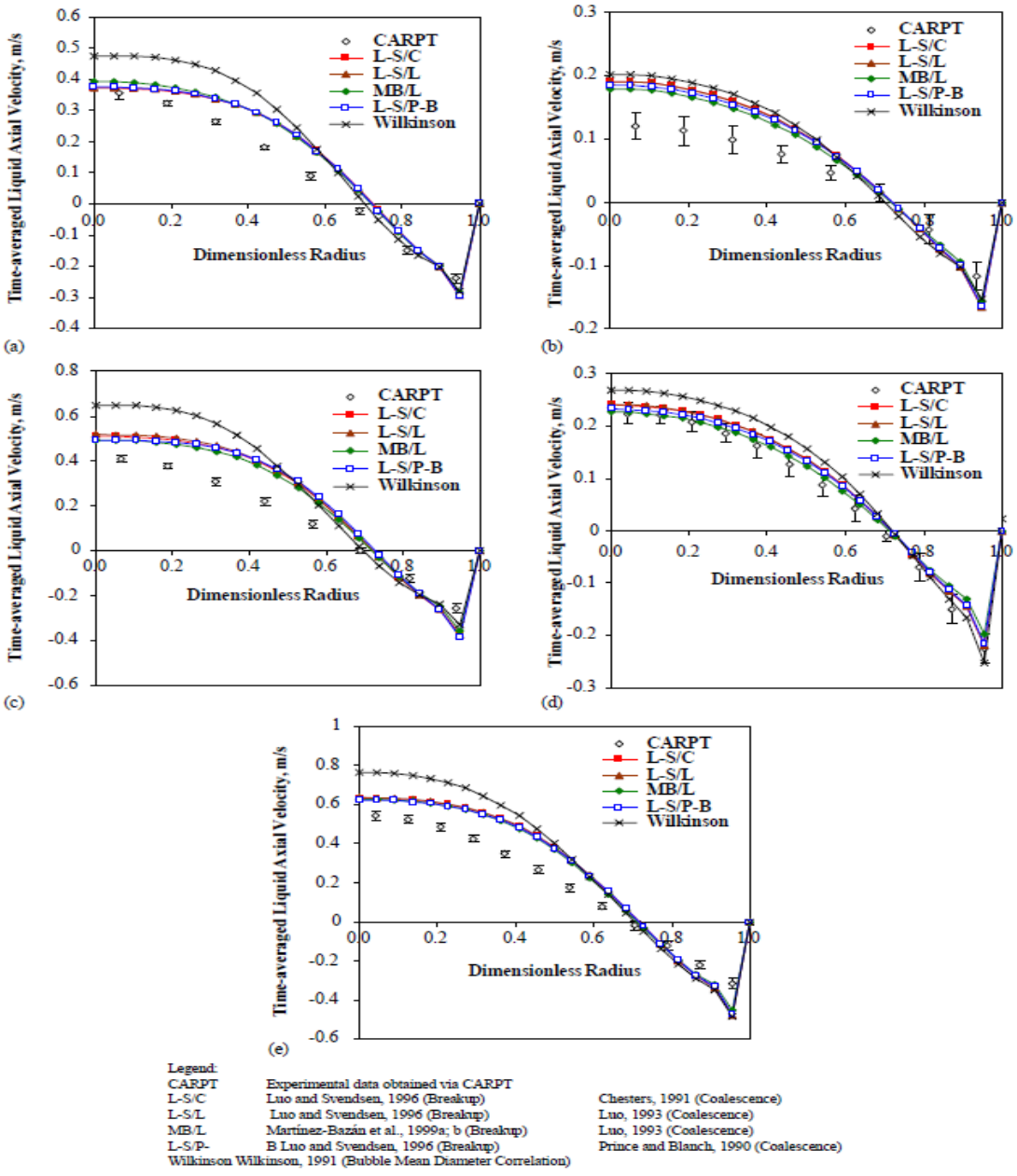

Fig. 2-10. Comparison between CFD and experimental results, (a) 0.14 m column diameter using 0.096 m/s Ug, (b) 0.19 m column diameter using 0.02 m/s Ug, (c) 0.19 m column diameter using 0.12 m/s Ug, (d) 0.44 m column diameter using 0.02 m/s Ug, (e) 0.44 m column diameter using 0.1 m/s Ug (Chen et al. 2005)

Wang et al. (2003 and 2005) studied the effect of different coalescence and breakup kernels that include Prince & Blanch (1990), Luo (Luo 1993; Luo & Svendsen 1996) and Lehr et al. (2002) formulations. The superficial velocities were tested from 0.03 m/s to 0.12 m/s and results show that the Luo breakup model predicts a lower breakup rate, while the Lehr kernel predicts a higher breakup rate. Furthermore, the bubble size distribution (BSD) in the case of Prince and Luo formulations was mono-modal and shifted towards the left-hand side (forming small bubbles) when superficial gas velocity was increased. The BSD proposed by Lehr model is mono-modal at low superficial velocity (Ug) and becomes bi-modal with an increase in Ug. The authors suggested that the Lehr formation has a tendency to simulate heterogeneous regimes. Wang proposed his own coalescence model that included the phase fraction parameter while the rest is very similar to Lehr formulation.

Bannari et al. (2008) worked on the 3D-simulations of a dispersed two-phase flow using a bubble class method applied to population balance. The interphase included the drag, virtual mass, and lift forces. The superficial gas velocity was varied from 0.0014 m/s to 0.0073 m/s, assuming a diluted system with a gas holdup below 5 %. The liquid bed height was also varied from a 2.25 to a 4.5 height-to-width ratio. The predicted time-averaged radial profiles of hold up and axial liquid velocity were in good agreement with experimental values. Furthermore, the authors did not report a significant difference in the radial profiles of the gas holdup and axial liquid velocity as compared to experiments using a different number of bubble classes, which were varied from 11 to 25 classes.

Zhang et al. (2006) analyzed the influence of the interphase forces and the closure of the turbulence model on the hydrodynamics of the two-phase bubble column. The interphase forces included the drag, lift and virtual mass. The turbulence source terms, also known as bubble-induced turbulence (BIT), consisted of Sato & Sekogushi (1975), Pfleger & Becker (2001) and Troshko & Hassan (2001) correlations. The k-epsilon turbulence model was used and solved for the liquid phase. The Zhang concluded that the drag force affects the gas hold and axial liquid radial profiles while the virtual mass has no influence. The lift force significantly impacts the fluid behavior, especially the dispersion and shape of the bubble plume. Furthermore, the effective liquid viscosity predicted by the Troshko BIT model showed a peak near the wall, which was non-consistent with the experimental profiles. The Sato model gave a higher turbulent viscosity and resolved only the overall flow patterns and as a result quasi-state bubble plume was predicted. The fluctuating

velocity of the liquid phase predicted by the Troshko and Pfleger models were in good agreement with the empirical observations.

Laborde-Boutet et al. (2009) simulated the churn flow in a two-phase bubble column and investigated the turbulence model in the Reynolds-Averaged Navier-Stoke (RANS) approach. The k-epsilon turbulence model consisted of Standard, Renormalization Group (RNG) and Realizable formulations. These formulations were solved for the continuous phase and the influence of bubble-induced turbulence (BIT) was also studied. Furthermore, the numerical verifications were performed on seven different mesh sizes. They considered a constant bubble size, which was calculated from the Wilkinson (1991) correlation. The bubble-bubble interaction was ignored, while the gas-liquid interaction involved only the drag force. The authors concluded that the Standard and Realizable formulation of turbulence models deteriorated the flow fields (axial velocity and gas holdup), and even the inclusion of BIT did not lead to improvement. The RNG k-epsilon formulation predicted good results with the experimental data and this formulation led to higher energy dissipation rate as compared to the Standard and Realization formulations. The influence of BIT on the radial profiles of gas holdup and axial liquid velocity was negligible. Furthermore, the authors suggested using a higher order of discretizing scheme and finer mesh to avoid unwanted numerical diffusion.

Krepper et al. (2008) implemented an inhomogeneous multiple size group (iMUSIG) formulation to simulate the bubble column. This formulation divides the gas phase into N number of velocity groups and solves the momentum equation for each group, making the solution computationally costly. The authors suggested that 2-3 subgroups are sufficient to capture the fluid behavior in the heterogeneous regime. It was concluded that although iMUSIG allows simulating the local radial profiles, it is still limited by breakup and coalescence kernels that use the isotropic turbulent approach.

Xu et al. (2013) simulated a bubble column using constant-size bubbles, double-size bubbles and a population balance model (MUSIG and iMUSIG) approaches. For the constant-size bubble, Wilkinson's (1991) correlation and the latter depends on the viscosity of the continuous phase, density of each phase and on the superficial velocity. The double-size model involved Krishna et al. (2000) formulation (as discussed earlier) while the population balance model consisted of Luo coalescence and Luo & Svendsen breakup models (Luo 1993; Luo & Svendsen 1996). The authors

used a scaling factor (=0.5) to decrease the bubble coalescence. The Xu concluded that the constant-bubble and double-size bubble models were unable to predict the radial profile of gas holdup close to experiments. However, both homogeneous-MUSIG (with lift forces) and inhomogeneous-MUSIG models agreed well with experimental values.

Masood & Delgado (2014) studied the influences of different drag forces and turbulent source terms. The experimental setup involved a rectangular bubble column operated at 0.0097 m/s and 0.0122 m/s superficial gas velocities. The model validation was performed by comparing the radial profiles of gas holdup and axial liquid velocity with experiments. The authors concluded that the drag coefficient proposed by Ishii & Zuber (1979) predicted better flow fields when compared with empirical data. RNG k-epsilon and RNG k-epsilon (with BIT) both agreed well with experiments and no significant influence of BIT was found. Furthermore, the inclusion of wall lubrication force increased the vertical liquid velocity, especially at the center due to the fact that the bubbles were pushed from the wall vicinity towards the center of the column.

Yamoah et al. (2015) performed a sensitivity analysis on a wide range of interphase momentum transfer models. The latter included the drag, lift, wall lubrication and turbulent dispersion forces. The bubble size was assumed to be constant for all set of CFD-simulations. The authors reported the insignificant difference between Antal et al. (1991) and Frank et al. (2004) wall lubrication coefficients when compared to experimental values. Furthermore, at higher Reynolds number, the Tomiyama (1998) lift coefficient predicted a similar trend of the radial profiles of gas holdup and axial liquid velocity with the empirical values. Wang & Yao (2016) also evaluated the interphase forces and concluded that each model has its limitation related to bubble size, bubble shape, flow regime and operating conditions. Hence, there is no universal model fitting all the operating conditions. However, the authors suggested that the inclusion of drag, lift and wall lubrication forces are necessary to simulate the bubble column.

2.13 Previous Studies on the Three-Phase Flow

Farouk & Shah (1997) examined the hydrodynamics of a three-phase bubble column using 2D-axisymmetric geometry. The fluids consisted of air, water, and glass beads for which the average diameter and density were 0.405 mm and 2460 kg/m^3. CFD-simulations were performed using a three-fluid model consisting of gas-liquid and liquid-solid interactions. The gas-liquid interaction involved the Ishii & Zuber (1979) drag coefficient, which was tuned to take into account the influence of the solid phase. The effective solid viscosity was derived and calculated from the Choi & Chung (1983) correlation. The Standard k-epsilon turbulence model was solved for the liquid phase, whereas the influence of bubbles were considered by bubble-induced turbulence (BIT). The authors concluded that the axial solid velocity trend in the three-phase system was similar to axial liquid velocity in two-phase, which is high at the center and low near the wall of the column making parabolic shape profile. They proposed a new parameter for the drag correlation that requires tuning from case to case. Furthermore, the grid sensitivity performed on 50x20 and 60x30 mesh sizes, showed similar results with the experiments. Overall, the axial solid fraction was in good agreement with the experiments.

Matonis et al. (2002) performed both experiments and CFD-simulations to evaluate the flow fields and turbulence parameters in a slurry bubble column. The solid viscosity and phase velocities were determined by the viscometer and particle image velocimetry (PIV) techniques. The superficial gas and liquid velocities were 0.037 m/s and 0.02 m/s respectively and the solid phase involved glass-beads with a particle size of 800 μm. The mass and momentum equations were solved for each phase (three-fluid model). The gas-solid drag force included the Ergun (1952) and Stokes (Soo 1990) formulations, while the particle-particle drag coefficient was based on the kinetic theory of granular flows formulated by Syamlal (1985). The published results for the gas holdup, axial velocities and stresses showed similar trend with regard to the experiments.

Michele & Hempel (2002) measured and modeled the liquid field and gas holdup values in a two- and three-phase bubble column. The liquid velocity was measured by an electrodiffusion measurement (EDM) electrode. The superficial gas velocity (Ug) was varied from 0.02 m/s to 0.09 m/s and the solid loading was 10 % with particle size and density of 3 mm and 1200 kg/m^3 respectively. The solid viscosity was assumed to be constant. The inlet geometry consisted of a plate, one nozzle placed at the center and the ring spargers. Results showed that the spargers design

significantly influenced the central-line axial liquid velocity. In the case of the plate sparger, the measured central-line axial liquid velocity remained almost constant along the column height (except near the distributor). However, the nozzle configuration showed two peaks, one at the bottom of the column and other at the top of the column. Furthermore, at 0.02 m/s Ug, the nozzle sparger produced a 100% higher central-line axial liquid velocity as compared to plate distributor. At the highest Ug value, this difference was reduced to 20%. The predicted radial profile of axial liquid velocity using the plate sparger showed similar trend with the experiments. However, the model failed to correctly predict the total gas holdup values with the empirical values. The authors didn't show simulation results using nozzle geometry.

Gamwo et al. (2005) studied the influence of particle size for methanol synthesis in an industrial-scale slurry bubble column. The column diameter and superficial gas velocity were 0.57 m and 0.1524 m/s respectively. The solid loading was 18% with an average particle diameter varying from 20 to 120 microns. Both reactions and mass transfer rates were implemented in the simulations. The former was then correlated with the particle granular temperature, which changes depending on different particle size. The particle-particle interaction involved the kinetic theory of granular flows (KTGF). The authors concluded that the maximum values of 356 cm^2/s^2 granular temperature, which was found for 60-70 micron particle size. Hence, the optimum particle size for the methanol synthesis is 60-70 micron.

Rampure et al. (2003) performed both the experiments and CFD-simulations for a gas-liquid and gas-liquid-solid systems in a cylindrical column. The superficial gas velocity was varied from 0.01 m/s to 0.20 m/s, whereas the solid loading was in the range of 1 to 20%. The solid particle and bubble sizes were 0.45 mm and 5 mm and the solid viscosity was calculated using the KTGF approach. Results showed that the predicted axial liquid velocity in gas-liquid system agreed well with the experiments, however, the gas holdup was over-predicted. The predicted solid holdup in gas-liquid-solid system showed an increase in concentration near the wall, which was non-consistent with the experimental data obtained by the same authors.

Schallenberg et al. (2005) evaluated the influence of the solid phase on gas-holdup in a three-phase bubble column. The superficial gas velocity was varied from 0.02 m/s to 0.08 m/s, whereas the particle loading and particle size were 10 % and 3 mm respectively. The solid viscosity was assumed to be constant and was equal to the water viscosity. The three-fluid model was used for

the gas, liquid, and solid phases and the liquid phase was treated as a continuous phase while the rest were treated as a dispersed phase. The phase interactions involved the gas-liquid, liquid-solid, solid-solid and gas-solid. The former interaction included Ishii & Zuber (1979) drag coefficient, which was scaled using 'E' factor which was a "fitted" parameter calculated from the empirical data. The liquid-solid, solid-solid and gas-solid drag coefficients were based on Schiller & Naumann (1933), Wen & Yu (1966) and Michele & Hempel (2002) correlations. The authors reported that the presence of solid phase reduced the axial liquid velocity in the three-phase as compared to two-phase flow. Furthermore, the total gas holdup in the three-phase system was also decreased in comparison with the two-phase. This decreased in holdup was related to the presence of particles, which increased the bubble coalescence and formed large bubbles. The latter had higher bubble rise velocity leading to lower gas holdup values. Still, in this case, the predicted axial liquid velocity and total gas holdup were in good agreement with the empirical values.

Panneerselvam et al. (2009) studied the hydrodynamics of a gas-liquid-solid fluidized bed using simulations where the results were compared with two different set of experiments. The particle mean diameter used in the experiments were 2.3 mm and 3 mm and the initial solid loadings were 59 % and 60 %. For such a dense system, the authors considered a constant viscosity model, which used a correlation that was based on a solid void fraction. This correlation predicts the solid phase pressure but ignores the solid shear viscosity. The phase interactions involved gas-liquid, liquid-solid, and gas-solid. The k-epsilon turbulence model was solved for the liquid phase, however, the bubble-induced and particle-induced turbulence were also taken into account using Sato & Sekogushi's (1975) correlation. Results showed that the predicted averaged gas holdup profile near the wall region was over-estimated as compared to experiments. Furthermore, the predicted solid profile and turbulence stresses showed a deviation in the range of 8-21% and 10-19% respectively. Overall, the simulation results showed a similar trend with regard to the experimental values.

Troshko & Zdravistch (2009) performed a CFD-simulations to model the Fisher-Tropsch synthesis in the industrial scale slurry bubble column. The two-fluid model consisted of a slurry (liquid and solid) and gas phases and interaction between the gas and slurry phase involved the Ishii & Zuber (1979) drag coefficient. The bubble-bubble interaction included the Luo (1993) bubble coalescence and Lehr et al. (2002) bubble breakup kernels. The k-epsilon turbulence model was solved for the mixture phase. The calculated turbulent kinetic energy was later tuned by correlation

to take into account the influence of the solid phase loading. The exponential value of the correlation was adjusted in order to provide a good match with the experiments. Results showed that the gas holdup in a 0% loading was over-predicted as compared to empirical data, however, at 36% loading, the predicted results showed similar trend with the experiments. The authors concluded that the CFD model could be used to simulate the Fisher-Tropsch synthesis at industrial scale bubble column.

Rabha et al. (2013) performed both the CFD-simulations and experiments to study the influence of the particle size on the hydrodynamics of slurry bubble column. The particle size was varied from 50 to 150 micron using a 0-20% solid loading in a 0.07 m diameter column. The liquid was treated as a continuous phase while the gas and solid as disperse phases. The population balance model (PBM) was considered to account for the bubble-bubble interaction and discretized using the bubble class method. The authors concluded that the presence of solid increased the Sauter-mean bubble diameter and decreased the gas holdup. Particle size and solid loading ≤ 100 micron and $\leq 3\%$ had no influence on the gas holdup. Furthermore, the predicted results were unable to estimate the bubble coalescence and bubble breakup correctly.

Ojima et al. (2014) used both modeling and experiments to investigate the effect of the hydrophilic solid particles on bubble coalescence using a rectangular bubble column. The superficial gas velocities were 0.02 m/s and 0.034 m/s and the solid loading was varied from 0 to 40 %. The particle density and particle sizes were 2250 kg/m^3 and 800 mm respectively. The modeling approach involved a hybrid model, which consisted of multi-fluid and interface-tracking models. The bubble-bubble interaction included the bubble coalescence and bubble breakup formulations. Results showed that the presence of solid particles influenced the film drainage time during the coalescence of two bubbles. The authors tuned this drainage time and presented the scaling factor. The latter factor is set to zero for two-phase flow, however, changes depending on the solid loading. The author concluded that the gas holdup was decreased with an increase of the solid loading, which promotes the bubble coalescence process. Furthermore, results showed that a multi-fluid model has a tendency to predict the phase distribution profiles in the slurry bubble column.

Xu et al. (2014) implemented the population balance model (PBM) in the slurry bubble column operated at a high superficial gas velocity of 0.26 m/s with solid loading up to 40%. The particle size and density were 35 microns and 2452 kg/m^3, respectively. The simulations were performed

using a constant bubble size model, 1D model, and PBM approaches. The latter approach included the Luo (1993) coalescence and Lehr et al. (2002) breakup models. The bubble coalescence was reduced using a scaling factor (c_0=0.4) to match the results. The momentum transfer between liquid and solid involved a hybrid interface, which takes into account the influence of solid phase loading. The authors concluded that the scaled-Luo and Lehr models predicted a total gas holdup value close to experiments. The axial solid holdup predicted by the modified interface showed a similar trend with experiments. Furthermore, the predicted profiles using 40% solid loading did not correlate with experiments.

Zhou et al. (2017) simulated a slurry bubble column using a Dual-Bubble-Size (DBS) drag model, which was based on the Energy Minimization Multi-Scale (EMMS) approach. The superficial velocities were varied from 0.02 m/s to 0.3 m/s and the solid loading was in the range of 0 to 40%. The gas-liquid interface involved the DBS-drag model, which is the ratio of drag coefficient and bubble diameter. This ratio was calculated from the correlation that depends on the superficial gas velocity. Moreover, when the solid loading is greater than 10 %, DBS-drag model is further modified and uses a scaling factor, which is tuned to match the results. The authors concluded that the DBS drag model predicted the gas holdup close to experiments with low solid loading ($<$ 10 %). The predicted the radial profiles using modified-DBS drag model agreed well with the empirical values for a solid loading of 25% and 40 %.

3 METHODOLOGY

3.1 Experimental Setups for the Published Data of the Hills (1974)

Since the multi-phase bubble column is a complex system, therefore, the CFD model was first tested in the simple two-phase flow. In the open literature, most of the experimental data were limited to lower superficial velocity, however, Hills (1974) performed the air-water experiments in a wide range of operating conditions. His data is extensively reported by other authors too and broadly considered. The Hills considered the superficial gas velocity of 0.019 m/s and 0.038 m/s in 0.138 m inner diameter and 1.38 m height bubble column. The inlet consists of 61 number of holes that were uniformly spaced on three circles, the hole diameter was 0.4 mm. The published data consisted of the gas holdup and axial liquid velocity profiles, which were plotted at 0.6 m height. For the measurement of the gas holdup, a conductive probe was used as it is shown in Fig. 3-1. The needle probe consisted of a tungsten wire, which was insulated by the Araldite resin. The wire was bent to 90 degrees, pointing vertical or horizontal direction. The wire was carried in a glass case of 3mm length that was attached to the column wall. The tip of the needle probe was considered as a single measuring point inside the bubble column and was traversed along the column diameter to measure the radial profile of the gas holdup. The time-averaged flow fields were observed to be radial symmetric in nature and remained unchanged with the position (vertical/horizontal) of the needle. The needle was either covered by gas bubble or liquid and depending on that conductivity was measured. These conductivity measurements were amplified and converted into bubble frequency to measure total gas holdup value at each radial point. The liquid axial velocity was measured by the modified Pitot tube (also called Pavlov tube), which measures the fluctuating pressure and calculates the local liquid velocity. Pavlov tube was connected to the differential pressure manometer and traversed over the column diameter to calculate the liquid velocity at each point. Further details of the experimental setup are mentioned in published data of the Hills (1974).

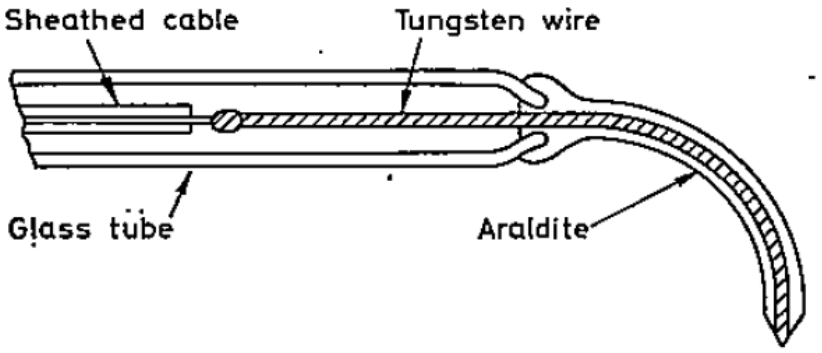

Fig. 3-1. The conductive probe used to measure the local gas holdup Hills (1974)

3.2 Experimental Setup for the Published Data of the Sannaes (1997)

The three-phase (air-water-glass beads) CFD simulations were validated with experimental setup of Sannaes (1997), which were performed in two columns (0.14 m and 0.26 m diameter) using a solid loading of 14 % and 7 % (volume based) and the superficial velocities of 5 cm/s and 8 cm/s. The air was dispersed through the perforated plate containing holes of 0.04 cm diameter, the configuration of the gas distributor is given in Table 5-3. The glass-beads density and mean-particle size were 2965 kg/m^3 and 151 microns respectively. This operating conditions and particle size are close to Enerkem's slurry column. The motion of the solid phase (glass-beads) was tracked by the Scandium radioactive particle (tracer) with a density of 2890 kg/m^3. The weight of the non-spherical tracer was similar as of particle of 150 microns. The terminal velocities of the glass-beads and tracer were 1.8 cm/s and 1.9 cm/s respectively. This velocity was determined by dropping the particles in a stagnant water and measuring the distance between two positions. The dynamics height was measured virtually. Since the free surface of the slurry bed was in continuous motion due to bubbles, the average dynamic height was considered. The total gas holdup calculation was based on this average dynamics height. The author measured the axial solid velocity profiles inside the columns where the fully developed region was reached, typically between 0.5 and 0.8 z/L. Here 'L' is the dynamic height of the slurry bed. To measure the local solid velocity, the Computer Automated Radioactive Particle Tracking (CARPT) technique was considered, as shown in Fig. 3-2. The motion of the solid phase was tracked by the Scandium radioactive particle (tracer). In the CART technique, the scintillation detectors (between 16 and 32) were placed at different locations of the columns (0.14 m and 0.26 m). The tracers follow the

continuous phase and emit the gamma-radiations and when these radiations interest with the detectors light photons are released and converted into anode current pulses. The fast filter amplifiers (FEA) were applied to amplify the pulses. The data from CARPT contains noise (low energy signals), which were filtered and removed by post-processing. Further details of the experimental setup are mentioned in the work of Sannaes (1997).

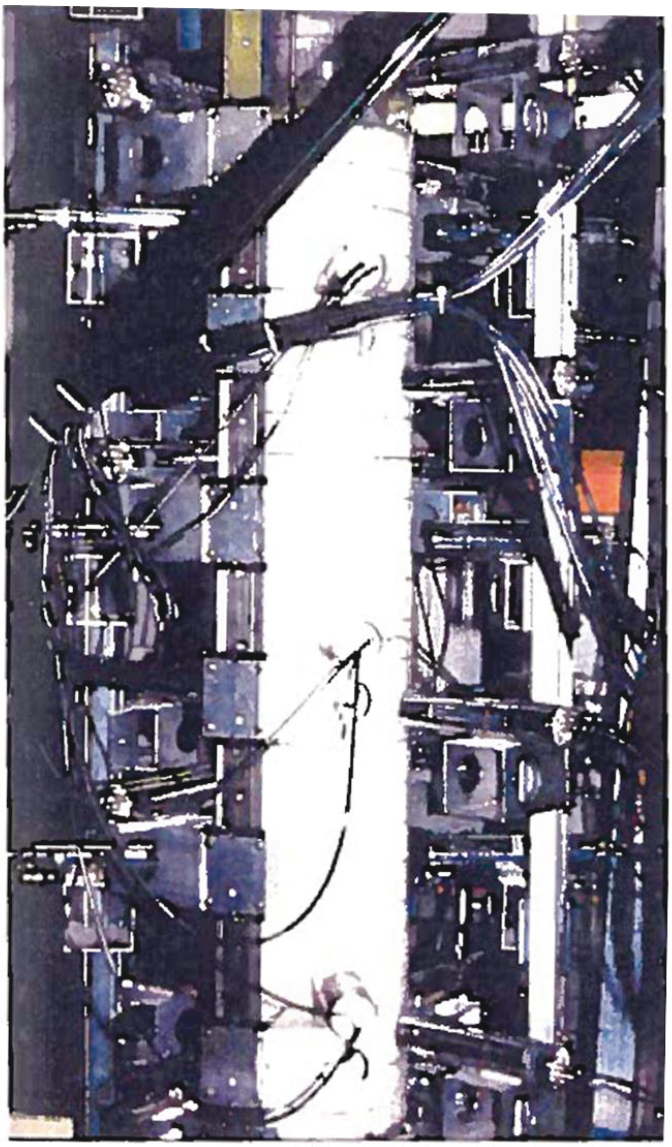

Fig. 3-2. CARPT technique to measure the solid movement inside the three-phase slurry reactor using 0.26 m diameter column Sannaes (1997)

3.3 Experimental Setup for the Bench

Scaling from industrial to bench unit is always been a challenge in chemical engineering and different techniques are being used including (but not limited to) dimensionless numbers. The key idea is to match the dimensionless numbers both in the lab and industrial scale units and once these numbers are matched, both systems are assumed to have similar hydrodynamic behavior. The dimensionless numbers depend on the column geometry, physical properties of fluid as well as on the operating conditions. Safoniuk et al. (1999) developed the dimensionless numbers, as according to the Buckingham Pi theorem, which involves the Morton number (Mo), Eotvos number (Eo), Froude number (Fr) and the density ratios as:

$$Mo = \frac{g\Delta\rho\mu_L^4}{\rho_L^2\sigma_L^3} \tag{3-1}$$

$$Eo = \frac{g\Delta\rho d_P^2}{\sigma_L} \tag{3-2}$$

$$Fr = \frac{q^2\rho_L}{D^2 g\Delta\rho} \tag{3-3}$$

Where $g\Delta\rho$, $\mu_L, \rho_L, \sigma_L, q, D$ and d_p represent the Buoyancy term, liquid viscosity, liquid density, surface tension, volumetric flow rate, column diameter and solid particle diameter respectively. The Enerkem industrial three-phase column was scaled down to a bench scale unit (see Table 3-1) to roughly approximate the bench dimensions (column diameter and height). All dimensionless numbers are in good agreement with each other except the density ratio. One of possible reasons for this discrepancy might be related to operating pressure. The actual Enerkem's reactor is operating at elevated pressure, however, the bench is considered to be at ambient pressure. The test bench included a transparent glass cylinder of 2.1 m height, 0.203 m inner diameter, and 2 mm (+/-1.1 mm) wall thickness. The latter was supplied by Friedrich & Dimmock International. The experiments were performed at ambient conditions. The superficial gas velocities (Ug) investigated in this work were of 0.010 m/s, 0.0151 m/s, 0.021 m/s and 0.026 m/s. Gas flow was monitored by a digital flow meter. The static bed height (water level) at rest condition (H_0) was 1.4 m and maintained constant throughout the experiments. The dynamics bed height (H_d) remained linear until a 0.026 m/s value of Ug was reached, corresponding to a homogeneous regime. The total gas holdup is calculated as

$$\alpha_g = \frac{H_d - H_0}{H_d} \tag{3-4}$$

The bubble plume height was observed visually at different velocity. The pressure probes close to the wall were located axially at 0.27 m, 0.58 m, 0.86 m, 1.14 m and 1.41 m and were connected to a high accuracy digital gauge. The experiments were performed with a gas inlet consisting of single and triple cylindrical porous spargers for which the dimensional ratio between bench and Enerkem units was respected. The height, diameter, and pore diameter of the sparger were of 0.1587 m, 0.0254 m and 0.8 µm respectively. The sparger top (see Fig. 6-1) was an opaque stainless steel plate supplied by the Pall Corporation. The experimental setup of the single and triple spargers are shown in Fig. 6-1 and Fig. 6-2 respectively. Each sparger was placed at an angle of 120^0. The distance between the spargers and the glass cylinder centroids was of 0.1016 m.

Table 3-1. Matching dimensionless numbers in Enerkem's bubble column and lab scale bench

Dimensionless number	Symbol	Enerkem Unit	Bench lab scale	
			Value	% error
Densities ratio 1	ρg/ρl	0.030	0.001	-95%
Morton number	Mo	0.00000000104	0.00000000104	0%
Eotvos number	Eo	0.000872	0.000872	0%
Densities ratio 2	ρs/ρl	3.58	3.57	0%
Modified Froude number	Fr	0.000093	0.000093	0%

3.4 Numerical Setups

The numerical setups both for the Hills (1974), and Sannaes (1997) as well as for the bench data are reported in chapters 4,5 and 6 respectively. The numerical setup includes fluids properties, geometry types, discretizing schemes, sampling method, mesh sizes, boundary types and bubble inlet size calculations.

4 CFD SIMULATION OF AN AIR-WATER BUBBLE COLUMN: EFFECT OF LUO COALESCENCE PARAMETER AND BREAKUP KERNELS

Abstrait

Dans ce travail, des simulations CFD d'une colonne à bulles air-eau ont été réalisées et validées à partir des données expérimentales. Un régime homogène a été retenu pour les vitesses superficielles des gaz comprises entre 0.019 m/s et 0.038 m/s utilisées dans ce travail. Ce type de régime implique une physique plus simple par rapport à un régime hétérogène où les vitesses superficielles sont plus élevées. Afin de simuler le système, un modèle de bilan de population a été résolu numériquement à l'aide d'une méthode discrète et d'un noyau de fermeture impliquant le modèle de coalescence de Luo ainsi que deux modèles de rupture différents: Luo et Lehr. Pour les calculs multiphasiques, un cadre eulérien a été sélectionné et le transfert de moment interphase incluait des termes de traînée, de levage, de lubrification des parois et de dispersion turbulente. Une analyse de sensibilité a été effectuée sur un noyau de coalescence de Luo en changeant le paramètre de coalescence (c0) de 1,1 à 0,1 et les résultats ont montré que les profils radiaux de rétention de gaz et de vitesse axiale du liquide étaient significativement affectés par ce paramètre. À partir des résultats de la simulation, les principales conclusions sont les suivantes: a) Une combinaison des coalescences de Luo et des noyaux de rupture de Luo (Luo-Luo) associée à une valeur décroissante de c0 améliorent les profils de rétention de gaz par rapport aux valeurs empiriques. Cependant, à la plus faible valeur de c0 étudiée dans ce travail, la vitesse axiale du liquide se détériore en ce qui concerne les données expérimentales lorsqu'on utilise une vitesse superficielle du gaz de 0,019 m/s. (b) Il a été montré qu'une combinaison des modèles de coalescence de Luo et de rupture de Lehr (Luo-Lehr) améliore les valeurs de rétention de gaz avec des données expérimentales par rapport aux grains de Luo-Luo. Cependant, lorsque c0 diminue, les modèles de Luo-Lehr sous-estiment les profils axiaux de vitesse du liquide en ce qui concerne les valeurs empiriques. (c) Des schémas numériques du premier et du second ordre permettent de prédire des profils radiaux similaires de rétention de gaz et de vitesse axiale du liquide. (d) Les résultats de la sensibilité du maillage montrent qu'une taille de maille de 3 mm peut être considérée

comme raisonnable pour simuler des données expérimentales. (e) L'inclusion du paramètre de lubrification de paroi s'est révélée significative, mais seulement lors d'un maillage plus fin. De plus, il permet une amélioration de la vitesse axiale du liquide au cœur de la colonne à bulles.

Auteurs et affiliation

Syed Alizeb Hussain: Département de génie chimique et de génie biotechnologique, Faculté de Génie, Université de Sherbrooke. La Chaire de Recherche Industrielle sur l'Éthanol Cellulosique et les biocommodités (CRIEC-B).

Tommaso Melchiori: Département de génie chimique et de génie biotechnologique, Faculté de Génie, Université de Sherbrooke. La Chaire de Recherche Industrielle sur l'Éthanol Cellulosique et les biocommodités (CRIEC-B).

Micael Boulet: Enerkem Inc., Sherbrooke, Québec, Canada.

Jean-Michel Lavoie : Département de génie chimique et de génie biotechnologique, Faculté de Génie, Université de Sherbrooke. La Chaire de Recherche Industrielle sur l'Éthanol Cellulosique et les biocommodités (CRIEC-B).

Date d'acceptation: 21st September 2017

Revue: Frontiers in Chemistry, section Chemical Engineering

Titre en français: Simulation CFD d'une colonne de bulle air-eau: effet du paramètre de coalescence de Luo et des noyaux de rupture.

CFD Simulation of an Air-Water Bubble Column: Effect of Luo coalescence parameter and breakup kernels

Abstract

In this work, CFD simulations of an air-water bubbling column were performed and validated with experimental data. The superficial gas velocities used for the experiments were 0.019 m/s and 0.038m/s and were considered as a homogeneous regime. The former involves simpler physics when compared to a heterogeneous regime where the superficial velocities are higher. In order to simulate the system, a population balance model (PBM) was solved numerically using a discrete method and a closure kernels involving the Luo coalescence model as well as two different breakup models: Luo's and Lehr's. For the multi-phase calculations, an eulerian framework was selected and the interphase momentum transfer included drag, lift, wall lubrication, and turbulent dispersion terms. A sensitivity analysis was performed on a Luo coalescence kernel by changing the coalescence parameter (c0) from 1.1 to 0.1 and results showed that the radial profiles of gas holdup and axial liquid velocity were significantly affected by such parameter. From the simulation results, the main conclusions were: (a) A combination of the Luo coalescence and Luo breakup kernels (Luo-Luo) combined with a decreasing value of c0 improves the gas holdup profiles as compared to empirical values. However, at the lowest value of c0 investigated in this work, the axial liquid velocity deteriorates with regards to experimental data when using a superficial gas velocity of 0.019 m/s. (b) A combination of the Luo coalescence and Lehr breakup models (Luo-Lehr) was shown to improve the gas holdup values with experimental data when compared to the Luo-Luo kernels. However, as c0 decreases, the Luo-Lehr models underestimate the axial liquid velocity profiles with regards to empirical values. (c) A first and second order numerical schemes allowed predicting similar radial profiles of gas holdup and axial liquid velocity. (d) The mesh sensitivity results show that a 3 mm mesh size can be considered as reasonable for simulating experimental data. (e) The inclusion of wall lubrication parameter was found to be significant, although only when using finer meshing. In addition, it allows an improvement of the axial liquid velocity at the core of the bubble column.

Keywords: Population balance model (PBM); Bubble size distribution; Time-average radial profiles of holdup and axial liquid velocity; Bubble column.

4.1 Introduction

Bubble columns have reportedly been used in the chemical, petrochemical, bioprocesses, and pharmaceutical industries. In simple bubble column reactors, the gas phase is dispersed into a liquid or liquid-solid continuous phase. In general, depending on superficial velocities and column diameter, the regime inside the bubble column is either homogeneous, transitional or heterogeneous (Deckwer 1992). The former involves simpler physics as compared to the latter and most of the models (interphase, coalescence, and breakup) were developed in that regime before being later implemented in the heterogeneous regime. The gas holdup has been reported as the most important design criterion in bubble columns. The latter is related to the bubble size, which ultimately allows determining the interfacial area and ultimately, defines the mass transfer phenomena. In biphasic non-reactive bubbly flows, the bubble size varies due to the gas and liquid velocities, inlet geometry, bubble coalescence, bubble breakup and bubble growth, hence complicating the hydrodynamic behavior inside the system (Fan 1989; Yeoh et al. 2014). Furthermore, the gas and liquid flow need closure terms in the interphase momentum transfer equations that depend locally on the velocity profiles, physical properties of phases and on the turbulence parameters that are still under development in the open literature (Ishii & Hibiki 2011). Hence, a comprehensive understanding of the fluid dynamics is required and the latter would, in turn, be very useful in many industrial fields. Many researchers have used computational fluid dynamics (CFD) techniques to simulate biphasic bubble columns. The latter are in most cases simulated by the Euler-Euler approach (two-fluid) due to a lesser computational cost when compared to the Euler-Lagrange or volume of fluid (VOF) approaches. In gas-liquid flow, the interface involves both drag and non-drag forces.

The drag force has an influence on the macroscopic structure of the flow. For instance, the radial profiles of velocity and holdup depend on the drag coefficient, Reynolds number, Eotvos numbers, terminal velocity and on the physical properties of the continuous phase (Wang & Yao 2016). Rzehak et al. (2017) simulated a bubbly flow in different operating conditions and the geometries using the Ishii drag coefficient (Ishii & Zuber 1979) and the predicted results were reported to be in good agreement with experimental values. This drag correlation is suitable for a wider range of bubbles sizes and covers all flow regimes (homogeneous, transitional or heterogeneous).

In bubble columns, the shape of the radial profiles may change according to the net lateral lift force. According to Tomiyama (2004), small bubbles (d_b <5.8 mm) have a positive lift coefficient and tend to go towards the reactor wall. However, larger bubbles have a negative lift coefficient and tend to stay at the core of the bubble column. Zhang et al. (2005 and 2006) suggested that the inclusion of the Tomiyama lift coefficient could predict a better correlation with experimental values. Nevertheless, Masood et al. (2014) and Yamoah et al. (2015) studied the influence of wall lubrication force and found that the Tomiyama correlation (Tomiyama et al. 1995) tends to over-estimate the velocity profiles when compared to the Antal correlation (Antal et al. 1991) that however agrees well with experimental data. Finally, Lucas et al. (2007) developed a 1D-model, studying the effect of wall lubrication and turbulent dispersion forces and suggested that the combination of these non-drag forces provides reasonable results.

Laborde-Boutet et al. (2009) focused on different formulations of the turbulent model and showed that the Renormalization Group (RNG k-ε) predicts higher turbulent dissipation rate as compared to Standard k-ε, which is known to be underestimated (Jakobsen et al. 2005). Most of the coalescence and breakup kernels depend on the local turbulent dissipation rate. Therefore, Laborde-Boutet suggested that the RNG k-ε turbulent model should be used to implement a population balance model.

The bubble coalescence and breakup phenomenon requires a Population Balance Equations (PBE) which allows discretization into N-classes of bubble size that can then be coupled with a two-fluid model. A single momentum equation can be solved for all N-classes, an approach called Homogeneous multi size group (MUSIG). In the case of non-homogeneous multi size group (called iMUSIG), multiple momentum equations are solved, making the solutions computationally costly. Krepper et al. (2008) developed and worked on the simulation of a gas-liquid phase using an iMUSIG model and suggested that 2-3 subgroups are sufficient to capture the fluid behavior. It was concluded that although iMUSIG allows simulating the local radial profiles, it is still limited by breakup and coalescence kernels that use an isotropic turbulent approach. Similarly, Xu et al. (2013) simulated a bubble column using both MUSIG, and iMUSIG. The results showed that the former (which includes lift force) and the latter both agreed well with experimental results. Wang et al. (2003 and 2005) studied the effect of different coalescence and breakup kernels and results showed that the Luo breakup (Luo & Svendsen 1996) predicts lower breakup rates, while the Lehr

kernel (Lehr et al. 2002) predicts higher breakup rates with regards to empirical values. The key difference in both kernels is in the estimation of the breakup efficiency. Luo's model includes the surface energy constraint, which shows that the break-up could only occur if the kinetic energy of the colliding eddies is higher than the surface energy necessary for bubble breakage. However, Lehr's model only considers the capillary constraint, assuming that the interfacial and inertial forces balance each other. Chen et al. (2005) also studied the effect of different kernels and concluded that the radial profiles were not sensitive as long as the breakup is increased ten times. Xu et al. (2013) used Luo's model for bubble coalescence and breakup and modified the coalescence parameter to 0.5, generating results that were in good agreement with experimental data.

In literature, the most commonly used kernel for bubble coalescence is the Luo's model while for bubble breakup, the Luo and Lehr model are usually preferred. Luo's coalescence model over-predicts the collision frequency and needs adjustment to reduce the coalescence rate which can be achieved by tuning the coalescence parameter (Wang et al. 2005; Yeoh et al. 2014). Finally, the effect of coalescence parameter in Luo's model was not extensively reported in the open literature and only a handful of studies have been published so far (Xu et al. 2013; Xu et al. 2014). Furthermore, the influence of this coalescence parameter on radial profiles of gas holdup and axial liquid velocity using two different bubble breakup models is limited.

In light of this, this work intends to fill the gaps identified in the previously reported approaches with the specific target to fit with industrial applications. Hence, the main objectives of this paper are as follows:

- Investigate the influence of the coalescence parameter on radial profiles using a combination of Luo coalescence and Luo breakup models.
- Study the influence of the coalescence parameter on radial profiles using a combination of Luo coalescence and Lehr breakup models.
- Perform a sensitivity analysis of a number of bubble classes and numerical schemes.
- Provide a sensitivity analysis of the wall lubrication force and the mesh sizes.

The presented results for a biphasic bubbling column were generated on a 2D-axisymmetric geometry and the predicted time-averaged profiles were compared with the literature data of Hills (1974). CFD-simulations were conducted using the commercial software ANSYS-Fluent v.17.2.

4.2 Model Development

4.2.1 Two-Fluid Model and Interphase

The eulerian framework was considered for the air-water system for which the conservation equations were solved for each phase while the mass and momentum equations are reported below as:

$$\frac{\partial(\alpha_q \rho_q)}{\partial t} + \nabla.\left(\alpha_q \rho_q \boldsymbol{u}_q\right) = 0 \tag{4-1}$$

$$\frac{\partial(\boldsymbol{u}_q \rho_q \alpha_q)}{\partial t} + \nabla.\left(\alpha_q \rho_q \boldsymbol{u}_q \boldsymbol{u}_q - \mu_q \alpha_q (\nabla \boldsymbol{u}_q + (\nabla \boldsymbol{u}_q)^T)\right) = -\alpha_q . \nabla p + \boldsymbol{F}_{pq} + \alpha_q \rho_q \boldsymbol{g} \tag{4-2}$$

4.2.2 Drag Force

The drag force is in this case generated by the slip velocity between the gas and liquid phases, which depends on the drag coefficient as well as the interfacial area of bubbles. For this study, the drag coefficient involves the Ishii correlation (Ishii & Zuber 1979), which considers a wide range of bubble size, varying according to the flow regime (viscous, distorted and capped regime). This variation of the flow regime depends in turn on the local Reynolds number in the viscous regime ($0 \leq Re < 1000$) and for distorted and cap regime ($Re \geq 1000$). The drag force and the Ishii drag coefficient are given by:

$$\boldsymbol{F}_D = -\frac{3}{4} \alpha_p \rho_q \frac{C_D}{d_p} \left|\boldsymbol{u}_p - \boldsymbol{u}_q\right| \left(\boldsymbol{u}_p - \boldsymbol{u}_q\right) \tag{4-3}$$

For viscous regime [$C_{D,dis} < C_{D,vis}$],

$$C_{D,vis} = \frac{24}{Re}(1 + 0.1Re^{0.75}) \tag{4-4}$$

For distorted regime [$C_{D,vis} < C_{D,dis} < C_{D,cap}$],

$$C_{D,dis} = \frac{2}{3} d_p \sqrt{\frac{g\Delta\rho}{\sigma}} \left(\frac{1 + 17.67 f^{*\frac{6}{7}}}{18.67 f^*}\right), \qquad f^* = (1 - \alpha_p)^{1.5} \tag{4-5}$$

For capped regime $[C_{D,dis} > C_{D,cap}]$,

$$C_{D,cap} = \frac{8}{3}(1-\alpha_p)^2 \tag{4-6}$$

The relative Reynolds number Re is defined as:

$$Re = \frac{\rho_q |\boldsymbol{u}_p - \boldsymbol{u}_q| d_p}{\mu_q} \tag{4-7}$$

4.2.3 Lift Force

In bubble columns, each upward moving bubble experiences a force perpendicular to the direction of its motion. This force is called *transverse* or *lift force* and is calculated by taking into account the disperse phase fraction, the density of the continuous phase, the relative velocity between phases, the velocity gradients as well as the lift coefficient. The lift coefficient plays an integral role on the radial profiles of gas holdup and on the liquid velocity. Small bubbles (d_b <5.8 mm) are known to have a positive lift coefficient and bubbles tend to go towards the lowest gradient of liquid velocity (i.e., towards the reactor's wall). Larger bubbles (d_b > 5.8 mm) however, are associated to a negative value and tend to stay at the core of the bubble column (Tomiyama 2004). The lift force and the Tomiyama lift coefficient are given as follows:

$$\boldsymbol{F}_L = -C_L \alpha_p \rho_q (\boldsymbol{u}_p - \boldsymbol{u}_q)(\boldsymbol{\nabla u}_q) \tag{4-8}$$

$$C_L = \begin{cases} \min\left[0.288\tanh\left(0.121Re, f(Eo')\right)\right], for\ Eo' \le 4 \\ f(Eo'), \qquad for\ 4 \le Eo' \le 10 \\ -0.27 \qquad for\ 10 \le Eo' \end{cases} \tag{4-9}$$

Where

$$f(Eo') = 0.00105Eo'^3 - 0.0159Eo'^2 - 0.0204Eo' + 0.474 \tag{4-10}$$

The modified Eotvos number Eo' is defined as:

$$Eo' = \frac{g(\rho_q - \rho_p)d_h^2}{\sigma} \tag{4-11}$$

Where

$$d_h = \frac{d_b(1 + 0.163Eo^{0.757})}{\sigma} \tag{4-12}$$

The Eotvos number Eo is described as:

$$Eo = \frac{g(\rho_q - \rho_p)d_b^2}{\sigma} \tag{4-13}$$

4.2.4 Wall Lubrication Force

The wall lubrication force acts near the vicinity of the wall and tends to push the bubbles away from it (Yeoh et al. 2014). The wall lubrication coefficient (Antal et al. 1991) depends mainly on the wall distance and the bubble size and it is given as:

$$\boldsymbol{F}_{wl} = C_{wl}\alpha_p\rho_q \left|\left(\boldsymbol{u}_p - \boldsymbol{u}_q\right)_{\parallel}\right|^2 (\boldsymbol{n}_w) \tag{4-14}$$

$$C_{wl} = max\left(0, \frac{C_{w1}}{d_p} + \frac{C_{w2}}{y_w}\right) \tag{4-15}$$

4.2.5 Turbulent Dispersion Force

The turbulent dispersion force accounts for the interaction between turbulent eddies and the disperse phase (i.e., bubbles). The latter disperses the bubbles from the most to the least concentrated regions. This force depends on the drift velocity and the gradient of the disperse phase (Simonin & Viollet 1990) and it is given by:

$$\boldsymbol{F}_{td,q} = -\boldsymbol{F}_{td,p} = C_{TD}K_{pq}\frac{D_{t,pq}}{\sigma_{pq}}\left(\frac{\nabla\alpha_p}{\alpha_p} - \frac{\nabla\alpha_q}{\nabla\alpha_q}\right) \tag{4-16}$$

4.2.6 Turbulent Model

The mixture Renormalization Group (RNG) k-epsilon model is written as:

$$\frac{\partial(\rho_m k)}{\partial t} + \nabla.(\rho_m \boldsymbol{u}_m k) = \nabla.\left(\left(\mu_m + \frac{\mu_{t,m}}{\sigma_k}\right)\nabla k\right) + G_{k,m} - \rho_m\varepsilon \tag{4-17}$$

$$\frac{\partial(\rho_m \varepsilon)}{\partial t} + \nabla.(\rho_m \boldsymbol{u}_m \varepsilon) = \nabla.\left(\left(\mu_m + \frac{\mu_{t,m}}{\sigma_\varepsilon}\right)\nabla\varepsilon\right) + \frac{\varepsilon}{k}\left(C_{1\varepsilon}G_{\varepsilon,m} - C_{2\varepsilon}\rho_m\varepsilon\right) \tag{4-18}$$

4.2.7 Population Balance Model (PBM)

The PBM was solved numerically using the class method for which the volume based bubble number density function is given as:

$$\frac{\partial}{\partial t} n_i + \nabla.(u_i n_i) = \sum_{d_j=d_i}^{d_{max}} \Omega_B(d_j:d_i) - \Omega_B(d_i) + \sum_{d_j=d_{min}}^{d_i/2} \Omega_C(d_j:d_i-d_j) - \sum_{d_j=d_{min}}^{d_{max}-d_i} \Omega_C(d_j:d_i) \quad (4\text{-}19)$$

The local gas volume fraction (or holdup) is defined as follows:

$$\alpha_g = \sum_{i=1}^{N} n_i \frac{\pi}{6} d_i^3 \quad (4\text{-}20)$$

The Luo coalescence kernel (Luo 1993) is the product of the collision frequency and coalescence efficiency. The binary coalescence phenomena between two classes of bubbles (d_i and d_j) is given as follows:

$$\Omega_C(d_i: d_j) = c_0(d_i + d_j)^2 \left(d_i^{2/3} + d_j^{2/3}\right)^{1/2} \varepsilon^{1/3} n_i n_j \, exp\left\{-\frac{t_c}{t_I}\right\} \quad (4\text{-}21)$$

Here c_0 is the adjustable coalescence parameter, which equals 1.1 in the Luo coalescence model. Other coalescence models (Chung-Hur Lee 1987; Prince & Blanch 1990) used the same approach but varied the coalescence parameter from 1.1 to 0.28. According to many authors who published on this aspect (Xu et al. 2013 and 2014), the Luo coalescence model over-predicts the collision frequency and requires adjustments. As mentioned earlier, the most commonly used breakup models are the Luo kernel (Luo & Svendsen 1996) and Lehr kernel (Lehr et al. 2002). Both models predict breakup rate and daughter size distribution directly from the models, hence the distribution does not need to be provided as an input parameter. The total breakup rate is given as:

$$\Omega_B(d_i) = \int_0^{0.5} \Omega_B(d_i: d_j) df \quad (4\text{-}22)$$

The binary bubble breakup according to Luo (1996) and Lehr (2002) are defined respectively as:

$$\Omega_B(d_i: d_j) = 0.9238 \varepsilon^{1/3} d_i^{-2/3} \alpha \int_{\xi_{min}}^{1} \frac{(1+\xi)^2}{\xi^{\frac{11}{3}}} exp\left(\frac{12\sigma c_f}{\rho_l \varepsilon^{2/3} d_i^{5/3}} \xi^{-11/3}\right) d\xi \quad (4\text{-}23)$$

$$\Omega_B(d_i: d_j) = \frac{1.19\sigma}{\rho_l \varepsilon^{1/3} d_i^{7/3} f^{1/3}} \int_{\xi_{min}}^{1} \frac{(1+\xi)^2}{\xi^{\frac{13}{3}}} exp\left(\frac{2\sigma We_{crit}}{\rho_l \varepsilon^{2/3} d_i^{5/3} f^{1/3}} \xi^{-2/3}\right) d\xi \quad (4\text{-}24)$$

4.3 Numerical Setup

All simulations were run on a 2D axis-symmetric geometry. The assumption for the 2D axis-symmetric could be reasonable since experimental data reported by Hills (1974) and Degaleesan (1997) showed that the time-averaged flow field produces a stationary axis-symmetric flow pattern, hence supporting the validity of the 2D model. Simulations were validated using the experimental data published by Hills (1974), which was shown to be robust and is often used by other authors (Krishna et al. 1999; Baten 2000; Ekambara and Joshi, 2005). Hills data has been extensively cited in literature explaining why the model developed in this work was validated using these empirical values. The two-fluids involved in the experiments consisted of air (acting as disperse phase) and water (considered as the continuous phase). The superficial gas velocity was varied between 0.019 m/s and 0.038 m/s, range in which a homogeneous regime could be achieved (Krishna et al. 1999). The diameter and height of the cylindrical column were of 0.138 m and 1.38 m respectively. The static liquid height was 0.9 m and all the experimental observations were performed at a 0.6 m height. The inlet geometry of the experimental setup consisted of a perforated plate with 61 holes which all had a 0.0004 m diameter. Due to the limitation associated with the mesh size and computational cost, the gas was assumed to be introduced uniformly from the bottom of the column. This assumption was supported by Buwa & Ranade (2002) where the influence of the sparger design using a perforated plate (actual experimental inlet with holes) and the sintered plate was investigated and was shown to induce no significant difference with regards to empirical data. They also concluded that a hole diameter of 0.8 mm requires, in turn, a very fine meshing in the simulations, making it computationally very expensive. Similarly, Chen et al. (2005) also simulated a bubble column using a sintered plate instead of a perforated plate and reported that it is not essential to use the actual experimental inlet configuration.

The boundary condition involves a uniform inlet bubble size which was calculated from Kumar's correlation and was obtained for diameters of 3.6 mm and 4.5 mm at superficial gas velocities of 0.019 m/s and 0.038 m/s respectively (Kumar et al. 1976). The outlet and wall include atmospheric pressure and non-slip boundary conditions respectively. Gas was the only mixture introduced from the inlet ($\alpha_p = 1$), while the 0.9 m static column height involved $\alpha_q = 1$ and $\alpha_p = 0$. Above this level (free board), the gas and water phase fractions were $\alpha_q = 0$ and $\alpha_p = 1$ respectively. The bubble volume of each class was calculated from the following formula ($v_{i+1}/v_i = 2^r$), where r

is the ratio factor which equals to 1, 2…n. For all the simulations (except for the mesh sensitivity analysis), a third order upwind scheme was used to discretize the continuity equation while the rest of the transport equations were solved by a second order scheme (see Table 4-1). The mesh sensitivity analysis was performed using a first order scheme due to convergence issues that were faced when solving the transport equations with higher order schemes for finer mesh. Convergence problems were encountered when an adaptive time step approach was used. In such cases, solutions tended to diverge due to the variation of the time step, especially at the initial flow time. The fixed time step was well consistent in term of convergence. Hence, 1E-04 sec time steps were used and guaranteed that the courant number for air and water velocities was less than 1. Once a statistically steady state was reached, a time-averaged sampling was calculated for 30 sec.

Table 4-1. Boundary conditions, physical properties and numerical schemes used in the simulation work

	Boundary and physical conditions	**Units**
Inlet	Velocity inlet	
Outlet	Pressure outlet	
Wall	Non-slip condition	
Pressure-velocity coupling	Coupled	
Bubble inlet size	3.6 and 4.5	mm
Time step	1.00E-04	s
Column diameter	0.138	m
Column height	1.38	m
Ug	0.019 and 0.038	m/s
Static loading height	0.9	m
	Numerical schemes for all the simulations	**Numerical schemes only for the mesh sensitivity**
Continuity	QUICK	First order upwind
Momentum	Second order upwind	First order upwind
Turbulent model	Second order upwind	First order upwind
PBM	Second order upwind	First order upwind
Transient formulation	Second order implicit	First order upwind

4.4 Results and Discussions

4.4.1 Number of Classes Comparison

The effects of three different distributions of bubble classes were investigated at a 0.019 m/s superficial gas velocity. In such case, the bubble coalescence and breakup were calculated according to Luo's model. The range of bubble diameters was varied from 1 mm to 28 mm, 1 mm to 32 mm and 1 mm to 46 mm hence covering all sizes of bubbles. These ranges were later divided into 14, 20 and 22 classes (bins). Fig. 4-1, shows a comparison of the time-averaged radial profiles of the gas holdup and the axial liquid velocity obtained from simulations using a different number of bubble classes. Results show so far that there is no significant difference in the predicted radial profiles. Such behavior is reasonable because according to the predicted particle size distribution (see Fig 4-2) all three distributions showed a similar trend while the higher bins are almost empty in all three cases that might influence the mean-bubble size and ultimately the radial profiles. Hence, 14 bubble bins were selected for the rest of the simulations to reduce computational cost.

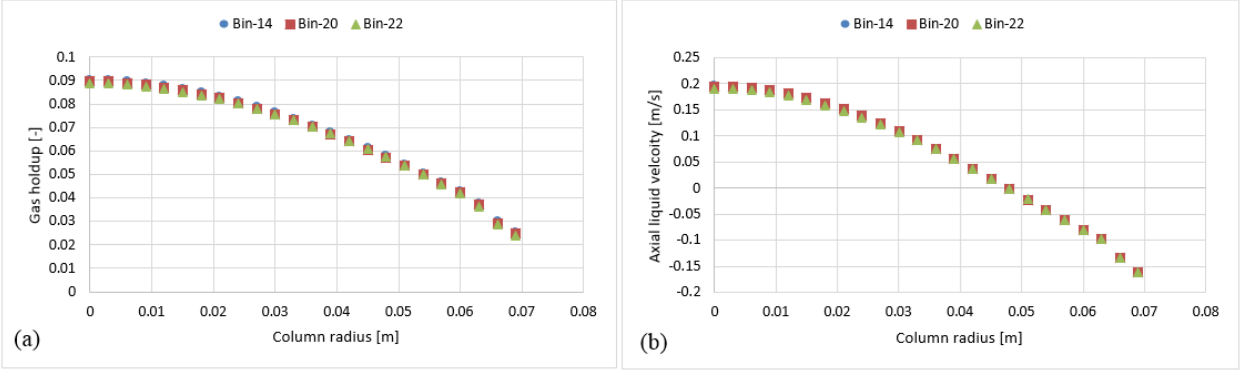

Fig. 4-1. Simulated time-averaged radial profiles of the gas holdup (a) and axial liquid velocity (b) using different number of bubble classes (bins)

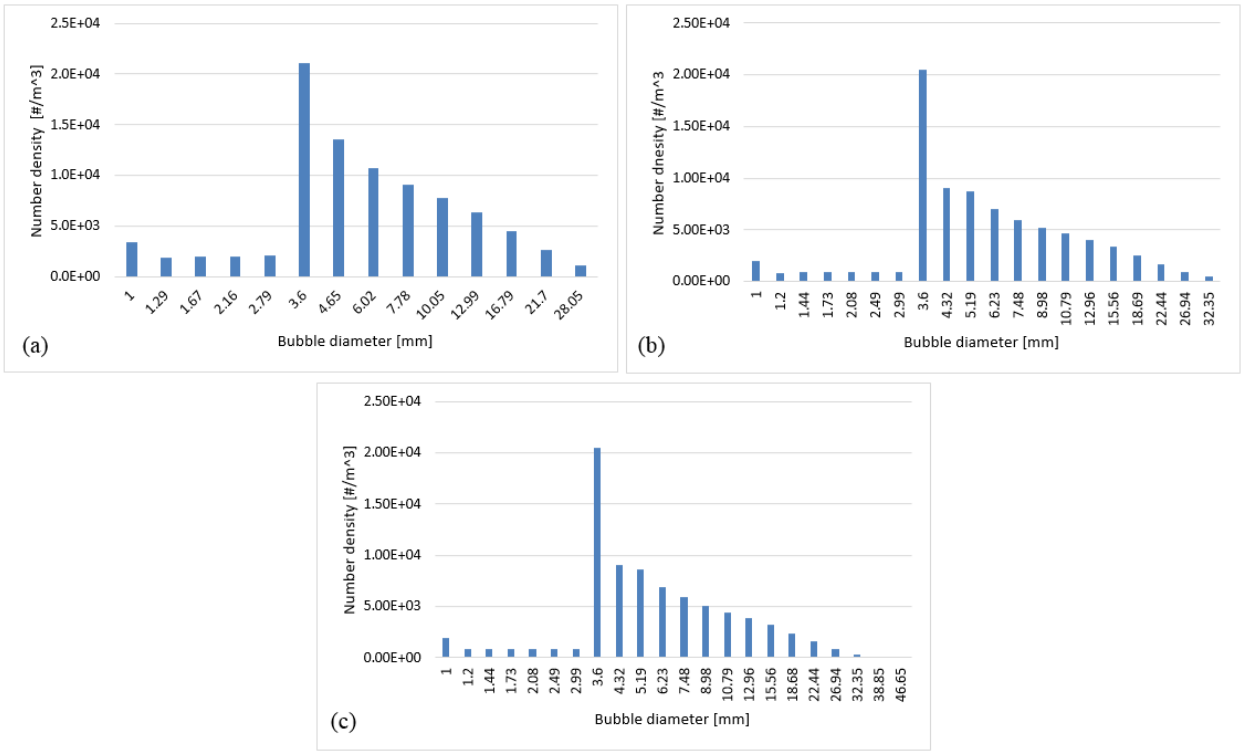

Fig 4-2. Predicted particle size distribution plotted at a 0.6 m height using (a) 14 bins (b) 20 bins and (c) 22 bins

4.4.2 Scheme Analysis

In bubble columns, liquid re-circulation is a known phenomenon occurring for column diameters greater than 0.1 m (Joshi 1980). This backflow might bring unwanted numerical diffusion in the system. To avoid such behavior, Jakobsen (2003) suggested using a higher order scheme, which may, however, cause instability and convergence issues (Ansys 2016b). The latter were faced in this work for finer mesh (1.5 mm x 1.5 mm) with the higher order scheme. Therefore, before performing a mesh analysis, the dependency of numerical schemes (first and second order) were evaluated both on 3 and 6 mm mesh sizes (Fig. 4-3 and Fig. 4-4). Results show that there is no significant difference in radial profiles. However, for coarser mesh size, a slight discrepancy was observed at the core of the column where the velocity magnitude is higher as compared to near wall vicinity, which might induce the numerical diffusion and predicts slight deviation.

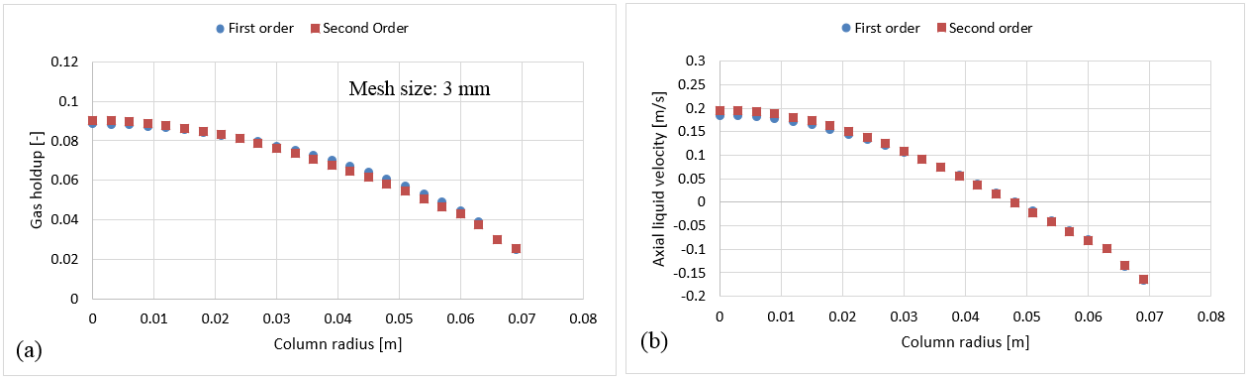

Fig. 4-3. Comparison between first and second order numerical discretization scheme on gas holdup (a) and axial liquid velocity (b) using 3 mm mesh size at a 0.019 m/s superficial gas velocity

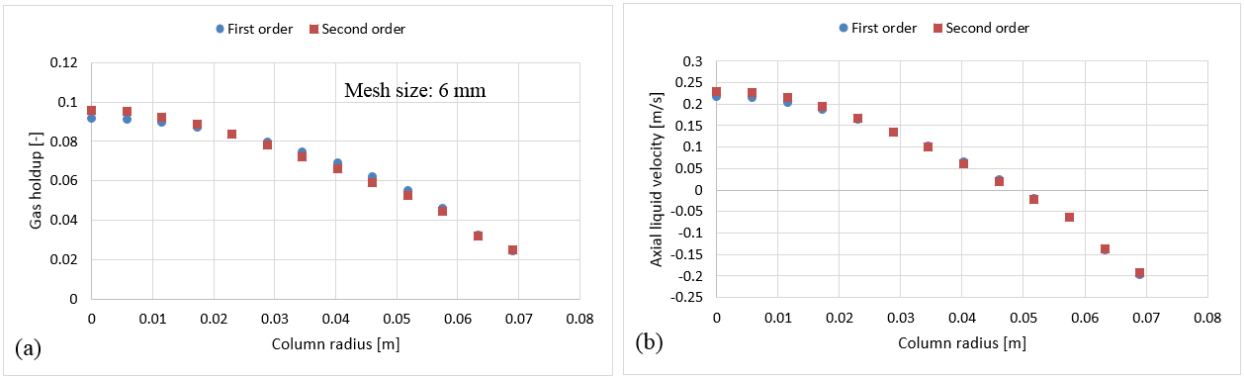

Fig. 4-4. Comparison between first and second order numerical discretization scheme on gas holdup (a) and axial liquid velocity (b) using a 6 mm mesh size at 0.019 m/s superficial gas velocity

4.4.3 Mesh and Wall Lubrication Sensitivity

As reported in Fig. 4-3 and Fig. 4-4, the influence of the first and second order schemes are non-significant with regards to the radial profiles of the axial liquid velocity and the holdup (except for a slight difference at the core of the column). Therefore, a first order scheme can be used for the mesh sensitivity analysis. Hence, the investigated mesh sizes were 1.5 mm x 1.5 mm (fine), 3 mm x 3 mm (medium) and 6 mm x 6 mm (coarse) leading to a total number of cells for the fine, a medium and coarse mesh of 41492, 10422, and 2736 respectively. Fig. 4-5 shows that the coarser mesh allows predicting a slightly higher gas hold up and axial liquid velocity due to the sharp gradient at the core of the bubble column. Simulations with finer mesh size predicted an increase of gas hold and liquid velocity near the wall. One of the possible reasons for this might be related to y^+ values. The latter is the dimensionless wall distance, where the regime is considered as viscous (non-turbulent). This value was calculated at the cell adjacent to the wall at 0.6 m height using a continuous phase velocity. Hence, the predicted y^+ values for the fine, medium and coarse mesh were 12.5, 26.75 and 58.29 respectively. The k-epsilon model using standard wall function

depends on the y^+ values and does not account for the turbulence parameter near the wall vicinity (viscous regime). In the case of the fine mesh, the y^+ value is very close to the wall. Hence, the simulations predict non-realistic profiles of the gas holdup and axial liquid velocity as compared to experimental data. This discrepancy could be avoided when including the wall lubrication force (Antal et al. 1991) that pushes bubbles away from the wall (as shown in Fig. 4-6). Results clearly show that both the 3 and 1.5 mm mesh sizes predict almost similar results following the inclusion of the wall lubrication force. Therefore, the simulations shown in the following sections were performed on a 3 mm mesh size, including the wall lubrication force. Furthermore, when including wall lubrication, the predicted axial velocity is slightly closer to experimental values. The discrepancy in gas holdup between simulations and experiment is explained in the next section. Additional investigation of wall lubrication coefficient with regards to wall distance is however beyond the scope of this study and could be the subject of future work.

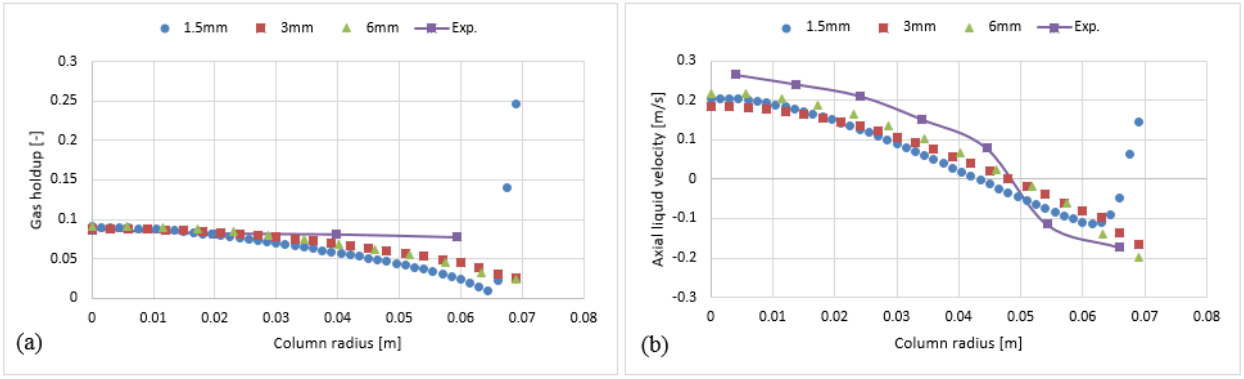

Fig. 4-5. Comparison between the radial profiles of gas holdup (a) and axial liquid velocity (b) obtained from three mesh sizes and validated with experimental data from Hills (1974) at a 0.019 m/s superficial gas velocity

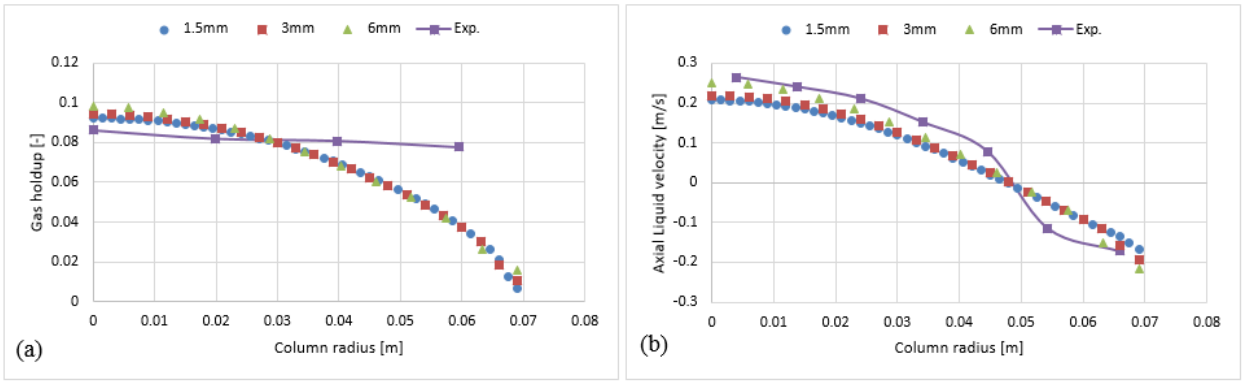

Fig. 4-6. Comparison of the radial profiles of gas holdup (a) and axial liquid velocity (b) obtained from three mesh sizes using wall lubrication forces and validated with experimental data from Hills (1974) at a 0.019 m/s superficial gas velocity

4.4.4 Kernels Sensitivity

The population balance model (PBM) was solved using Luo's coalescence model as well as two different breakup kernels: Luo and Lehr. The coalescence of two bubbles in a liquid medium is often described in three basic steps. First, the bubbles collide, resulting in the trapping of a small liquid film between them. This liquid tends to drain out until the film between bubbles reaches a critical thickness. Ultimately, the thin layer of liquid ruptures and leads to the coalescence of the two bubbles. Mathematically, these bubble collisions and the contact time to layer rupture are the product of collision frequency and probability function. The bubble collision frequency includes three types of mechanism: turbulent, buoyancy, and shear-stress. In the case of the Luo coalescence kernel (Luo 1993), the collision frequency only involves turbulent mechanism and the value related to the coalescence parameter c_0 was set to 1.1107. As discussed previously, the other coalescence models presented by Chung-Hur Lee (1987) and Prince & Blanch (1990) used a similar approach but varied this coalescence parameter from 1.1 to 0.28. Xu et al. (2013 and 2014) as well as Yeoh et al. (2014)reported for comparable investigations that the Luo coalescence model over-predicts the collision frequency and requires adjustment. The sensitivity analysis was performed on Luo's coalescence parameter and was tested at 1.1, 0.9, 0.5, 0.3, 0.2 and 0.1 respectively. The adjustment in the coalescence parameter was done using the user-defined-functions (UDF) and was compiled and implemented in Fluent v.17.2 accordingly.

4.4.5 Simulations with Luo's coalescence and Luo's breakup (Luo-Luo) model

Fig. 4-7a, shows the radial profiles of the gas holdup using the Luo coalescence and Luo breakup (Luo-Luo) kernels at a 0.019 m/s superficial velocity. The Luo-Luo models predict a higher holdup at the core and a lower holdup away from the core. In addition, the shape of the simulated holdup profile is parabolic, which is similar to the data recently reported by Van-Baten (Baten 2000). The latter reported that the holdup profile has a parabolic shape at a 0.019 m/s superficial velocity. This limitation of the CFD-simulation could be related to the turbulent model, which is isotropic in nature. The simulated gas holdup increased as the coalescence parameter (c_0) decreased to the lowest value. One of the possible reasons is that when c_0 decreases from 1.1, 0.9, 0.5, 0.3, 0.2 to 0.1, the predicted mean bubble diameter also decreases to 14.9 mm, 13.15 mm, 10.0 mm, 8.4 mm, 6.9 mm and 4.94 mm respectively, leading to an increase of a gas holdup. Also, the relative difference between simulations and experiments decreases significantly with a lower value of c_0 (see Table 4-2). The unwanted increase of the gas holdup near the vicinity of the wall especially

at c_0=0.1 is related to the lift force and is explained below. To have a clear picture of the effect of c_0 on the gas holdup, the total gas holdup for the simulations was determined by taking an area-weighted integral at 0.6 m height as shown in Fig. 4-8. As the c_0 values decrease from 1.1 to 0.1, the total gas holdup increased from 5.4% to 7.8%. The calculated experimental value of the total gas holdup is 8%. Hence, at the lowest value of c_0, the total gas holdup values is maximal and close to empirical value (8%). It could, therefore, be concluded that the modified Luo-Luo models provide total holdup results that are comparable with experiments in addition to c_0 values that may require tuning from case to case.

Fig. 4-7b, shows the time-averaged axial liquid velocity for the experiments using the Luo-Luo kernels. It was observed that the effect of c_0 was non-significant on the axial liquid profiles until a value of 0.2 was reached. One of the possible reasons is that the particle size distribution (see Fig. 4-9) does not change significantly and the predicted mean bubble diameters for the Luo-Luo and 0.2 Luo-Luo kernels are 14.9 mm and 6.9 mm respectively. The latter average bubble size is above the critical bubble size ($d_b > 5.8$ mm) and depicts a negative lift coefficient, therefore bubbles tend to stay at the core of the column (Tomiyama 2004; Lucas et al. 2007). In the case of 0.1 Luo-Luo kernels, the mean bubble size (4.94 mm) is below the critical bubble size (d_b <5.8 mm) and experiences positive lift coefficient, pushing the bubbles toward the wall (Tomiyama 2004; Lucas et al. 2007). This leads to a significant decrease of the axial liquid profile as compared to the empirical values. Hence, both the gas holdup and axial liquid velocity profiles must be compared with experiments when tuning this coalescence parameter.

Fig. 4-10 depicts the time-averaged volume gas fraction in correlation with different values of c_0. Results show that when moving from the gas inlet to the top of the column, the gas holdup reaches a maximum value before decreasing to a constant level. This phenomenon was clearly observed in Fig. 4-15. As c_0 decreases, the maximum value of gas holdup moves upward along the column (except c_0=0.1 where the fully developed region is not reached). Therefore, it could be concluded that c_0 effects the gas holdup both in the axial and radial directions.

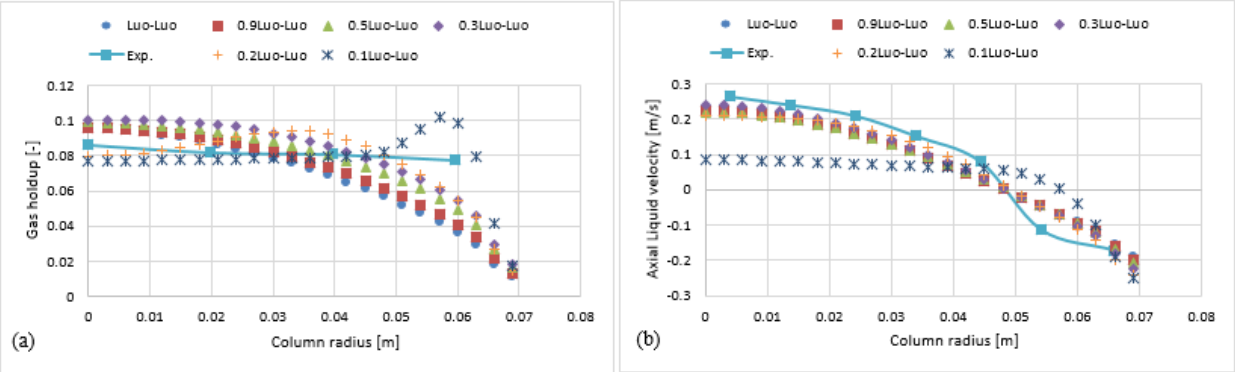

Fig. 4-7. Comparison of the radial profiles of gas holdup (a) and axial liquid velocity (b) obtained from different coalescence parameter values and validated with experimental data from Hills (1974) at a 0.019 m/s superficial gas velocity

Table 4-2. Area-weighted mean relative difference of the gas holdup profiles between experimental values of (Hills 1974) and simulations using 0.019 m/s and 0.038 m/s superficial gas velocity

Parameters	**Mean-relative difference (%) at 0.019 m/s**	**Mean-relative difference (%) at 0.038 m/s**
Luo-Luo	23.14	50
0.9Luo-Luo vs. Exp.	20.57	-
0.5Luo-Luo vs. Exp.	15.93	-
0.3Luo-Luo vs. Exp.	13.3	34.91
0.2Luo-Luo vs. Exp.	13.39	29.54
0.1Luo-Luo vs. Exp.	10.85	16.6
Luo-Lehr	6.82	9.9
0.9Luo-Lehr vs. Exp.	4.11	-
0.5Luo-Lehr vs. Exp.	3.69	-
0.3Luo-Lehr vs. Exp.	3.65	-

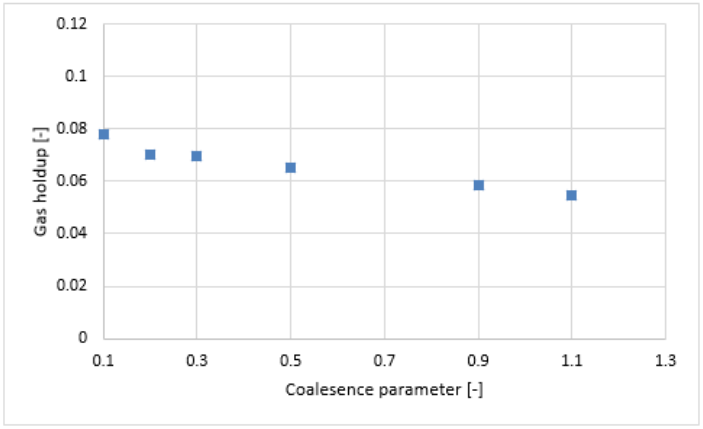

Fig. 4-8. Area-weighted total gas holdup in Luo-Luo model, calculated at 0.6 m height with different coalescence parameter

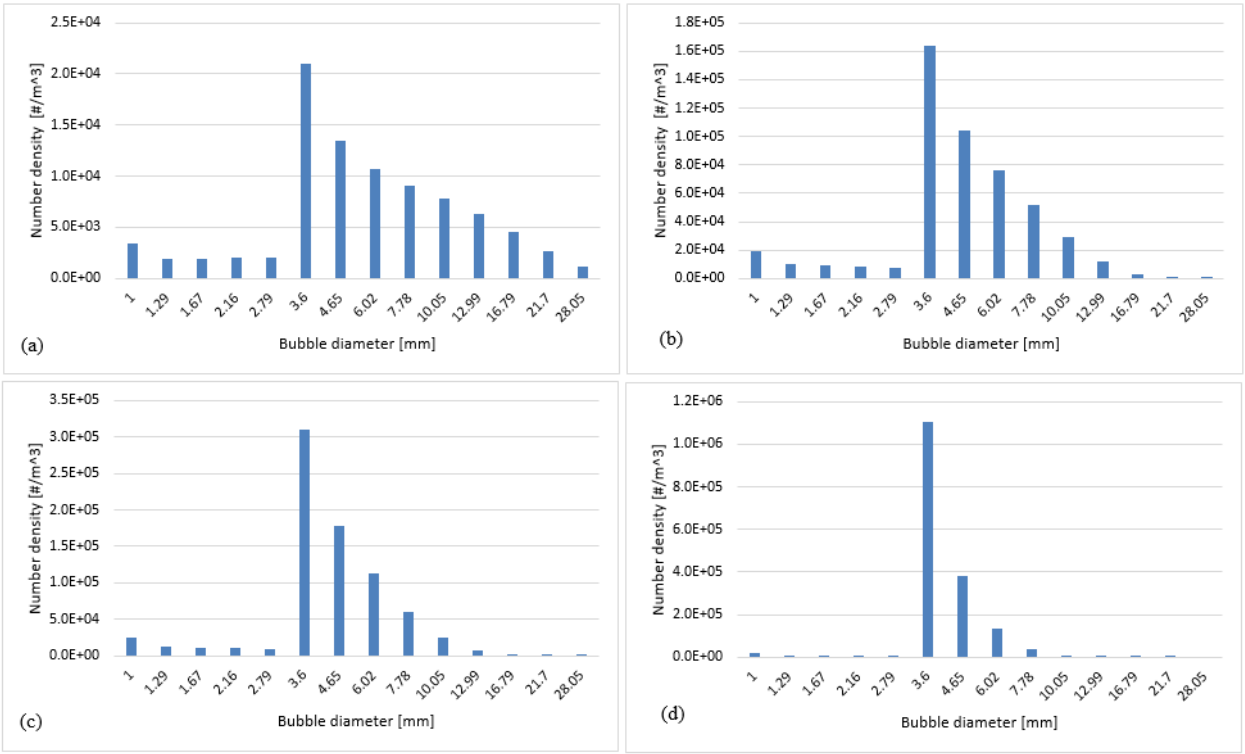

Fig. 4-9. Predicted particle size distribution plotted at 0.6 m height using (a) Luo-Luo, (b) 0.3 Luo-Luo, (c) 0.2 Luo-Luo and (d) 0.1 Luo-Luo kernels where the superficial gas velocity is 0.019 m/s

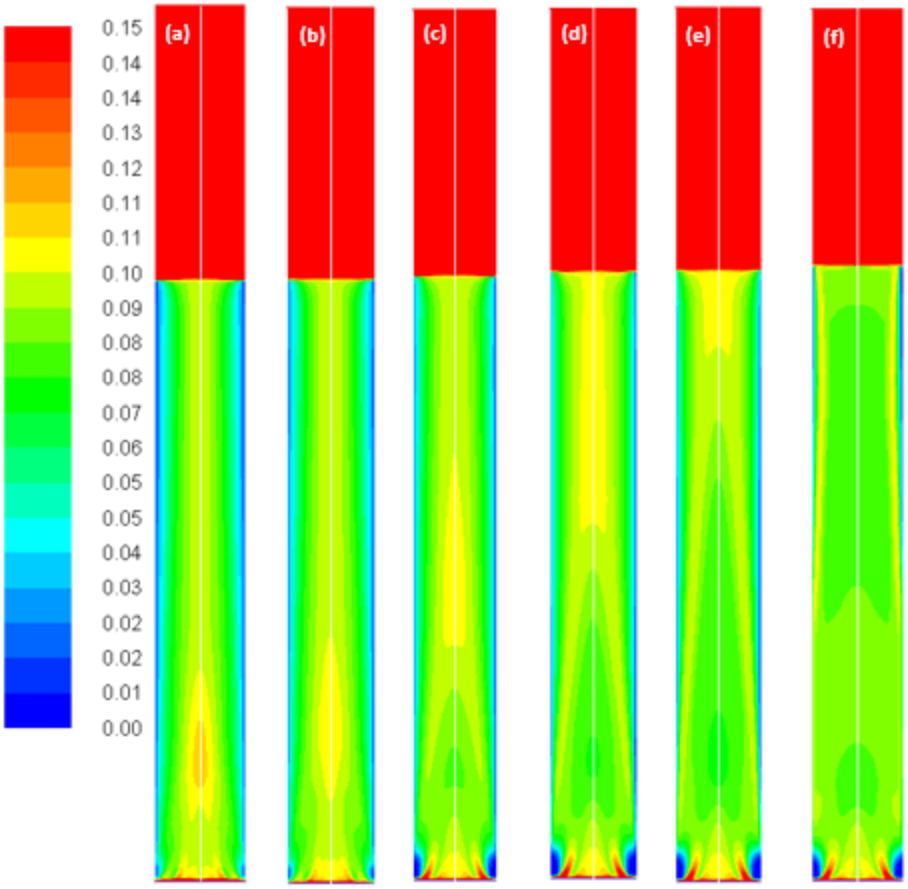

Fig. 4-10. Volume-gas fractions simulated with the Luo coalescence and Luo breakup model at a Ug value of 0.019 m/s using different values of the coalescence parameter, (a) default value 1.1; (b) 0.9; (c) 0.5; (d) 0.3; (e) 0.2 and (f) 0.1

4.4.6 Simulations with Luo's Coalescence and Lehr's Breakup (Luo-Lehr) Model

Fig. 4-11a, shows the radial profile of the gas holdup using a combination of the Luo coalescence and Lehr breakup models (Luo-Lehr) at a 0.019 m/s superficial gas velocity. The Luo-Lehr models predict a parabolic shape of gas holdup profile similar to Luo-Luo's model, which is not consistent when compared to experimental data. As previously mentioned, such behavior might be related to limitations related to CFD calculations. Moreover, as the coalescence parameter (c_0) decreases to 0.3, the predicted radial profiles become flatter and closer to experimental values, also the relative difference is lowest at 3.65 % (see Table 4-2). However, modifications of the Luo coalescence kernel significantly under-estimate the axial liquid velocity (as shown in Fig. 4-11b). In consequence, simulations using c_0=0.2 and c_0=0.1 were not performed. One of the possible reasons for such a discrepancy with the empirical values is that when c_0 is shifted from its highest to the lowest value (1.1 to 0.3), the particle size distribution (see Fig. 4-12) is shifted towards the left-hand side forming smaller bubbles. The predicted mean bubble diameter in the Luo-Lehr and 0.3

Luo-Lehr kernels are 6.6 mm and 4.5 mm respectively. The latter average bubble size experiences positive lift coefficient and influences the radial profile, which becomes flatter. Fig. 4-13 shows the effect of the coalescence parameter from 1.1 to 0.3 on the Luo coalescence and Lehr breakup model in term of the total holdup. Following a decrease of the coalescence parameter from 1.1 to 0.3, the total gas holdup slightly increased from 7.7% to 8.3%. Hence, tuning the coalescence parameter doesn't lead to a significant improvement in the total holdup. Fig. 4-14 and Fig. 4-15 depict the time-averaged volume gas fraction with different values of coalescence parameter. The bubbles are well dispersed inside the system and the maximum value of gas holdup moves upward along the column as the c_0 decreases. This behavior is consistent with the Luo-Luo kernels. However, at the lowest coalescence parameter (c_0 =0.3), the maximum gas holdup value in the Luo-Lehr kernels are not reached and the flow is in a developing stage. Because of this reason, the corresponding value for c_0 (0.3) was not plotted.

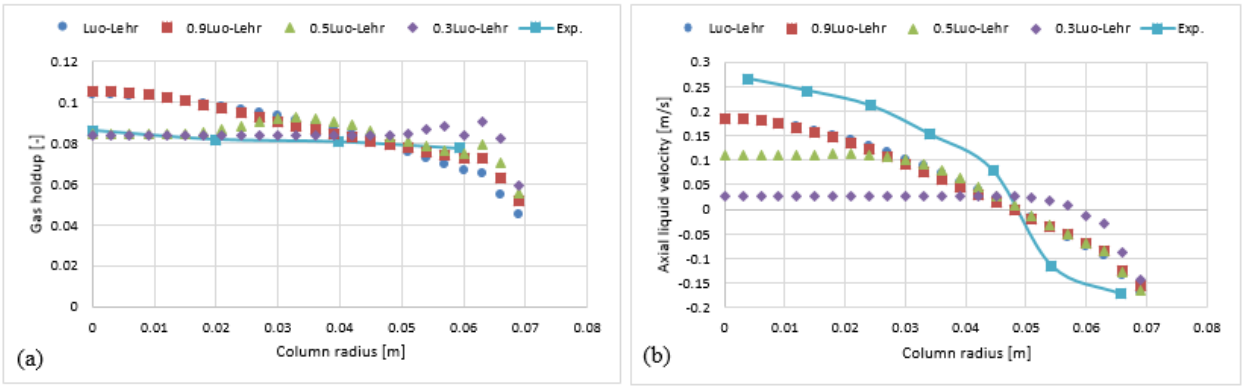

Fig. 4-11. Comparison of the radial profiles of gas holdup (a) and axial liquid velocity (b) obtained from different coalescence parameter values using Luo-Lehr models and validated with experimental data from Hills (1974) at a 0.019 m/s superficial gas velocity

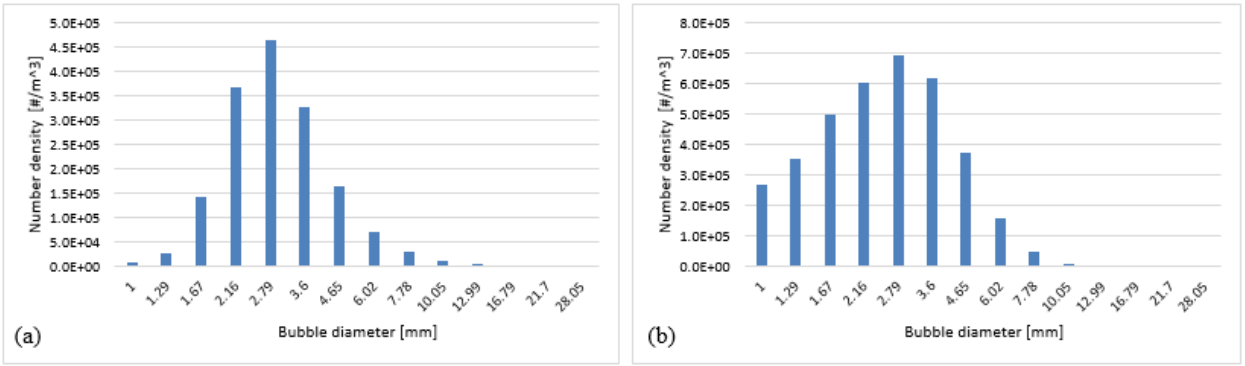

Fig. 4-12. Predicted particle size distribution at a 0.6 m height using the Luo-Lehr (a) and 0.3 Luo-Lehr (b) kernels with a superficial gas velocity of 0.019 m/s

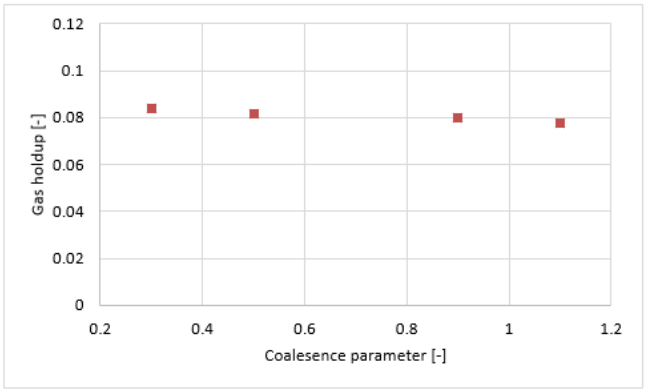

Fig. 4-13. Area-weighted total gas holdup in the Luo-Lehr model, calculated at a 0.6 m height with regards to the coalescence parameter

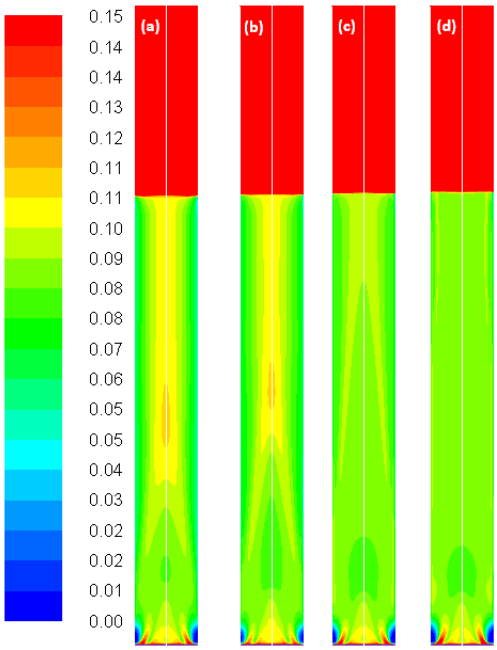

Fig. 4-14. Volume-gas fractions simulated with the Luo coalescence and Lehr breakup model at a Ug value of 0.019 m/s using different values of the coalescence parameter, (a) default value 1.1; (b) 0.9; (c) 0.5 and (d) 0.3

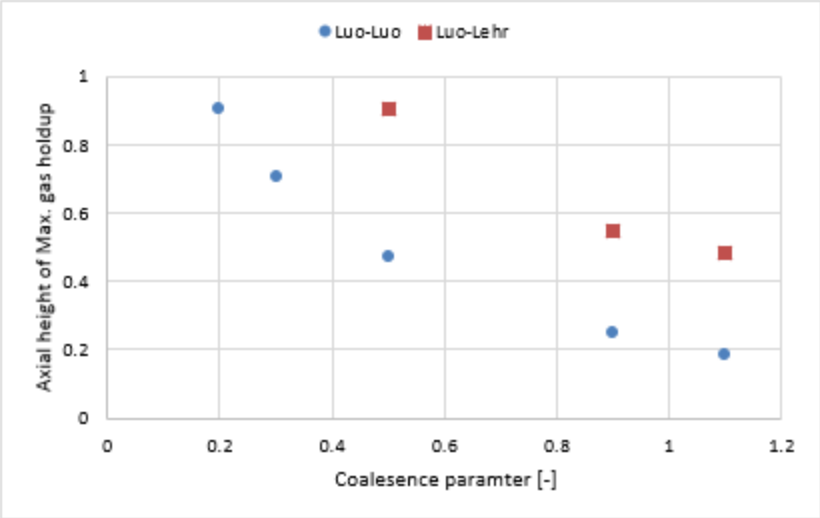

Fig. 4-15. Comparison of the axial height of the maximum gas holdup obtained from Luo-Luo kernels and Luo-Lehr kernel with different values of the coalescence parameter ranging from 1.1 to 0.2

4.4.7 Effect of Superficial Velocity

The impact of the higher superficial gas velocity (0.038 m/s) was studied with a combination of Luo coalescence and Luo breakup (Luo-Luo), modified Luo coalescence and Luo breakup (0.3 Luo-Luo, 0.2 Luo-Luo, and 0.1 Luo-Luo) and Luo coalescence and Lehr (Luo-Lehr) models. Fig. 4-16a and Fig. 4-17a show that at an elevated superficial velocity (0.038 m/s), all combinations depict a parabolic shape holdup with regards to experimental values. The unmodified Luo-Luo models predict a significant lower holdup as compared to empirical data (50% difference, see Table 4-2). However, an improvement in the radial profile of gas holdup was observed as the coalescence parameter was reduced. This behavior is consistent with previously discussed results reporting that the Luo-Luo models require tuning from case to case. Furthermore, the Luo-Lehr models predict a reasonable match as compared to experiment (9.9% difference, see Table 4-2) without using any scaling factor, which is also consistent with previously discussed results. In Fig. 4-16b and Fig. 4-17b a time-averaged radial profile of axial liquid velocity using different combinations of the models showed a similar trend and predict reasonable liquid profiles as compared to empirical values. The predicted mean-bubble size in the Luo-Luo, 0.3 Luo-Luo, 0.2 Luo-Luo, 0.1 Luo-Luo and Luo-Lehr models was 16.04 mm, 10.0 mm, 8.77 mm, 7.22 mm and 7.75 mm respectively. Table 4-3 shows the comparison for the total holdup between CFD simulations and experimental data using a 0.019 m/s and 0.038 m/s superficial gas velocities. Both modified Luo-Luo and Luo-Lehr models agree well with the experimental data.

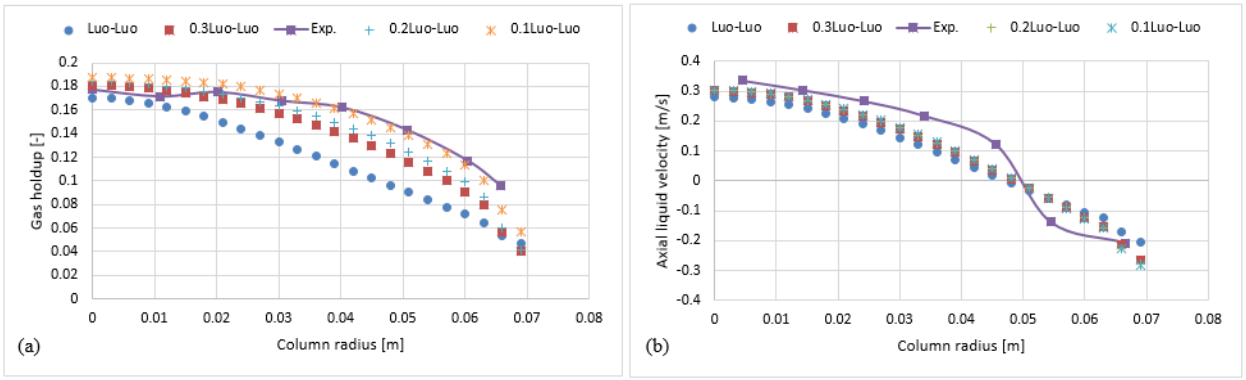

Fig. 4-16. Comparison of the radial profiles of (a) gas holdup and (b) axial liquid velocity obtained from modified and non-modified Luo coalescence and Luo breakup models and validated with experimental data from Hills (1974) at a 0.038 m/s superficial gas velocity

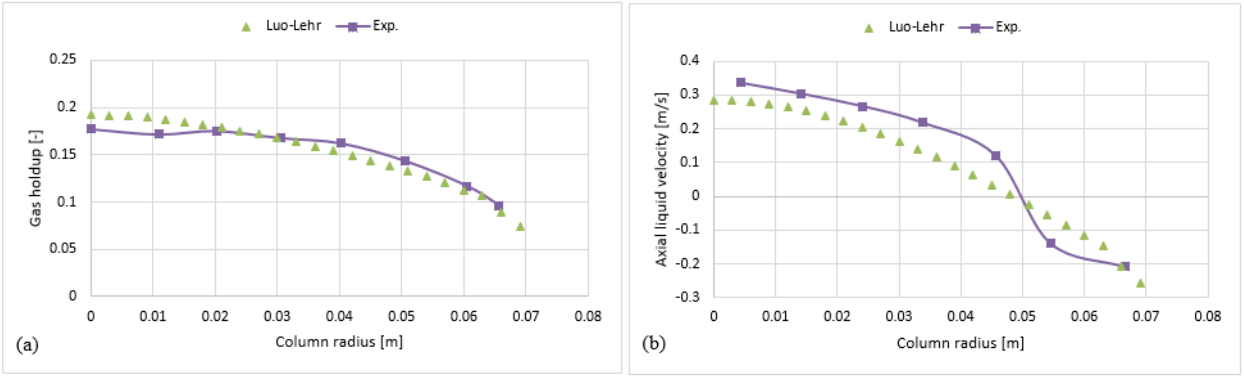

Fig. 4-17. Comparison of the radial profiles of (a) gas holdup and (b) axial liquid velocity obtained from Luo coalescence and Lehr breakup models and validated with experimental data from Hills (1974) at a 0.038 m/s superficial gas velocity

Table 4-3 Comparison of total gas holdup between CFD-simulations and experiments (Hills 1974) at 0.019 m/s and 0.038 m/s superficial gas velocities where the total hold up is determined by area-weighted integral of the profiles plotted at 0.6 m height

Results	**Ug [m/s]**	**Total holdup [%]**
Exp	0.019	7.86
Luo-Luo	0.019	5.46
0.3Luo-Luo	0.019	6.98
0.2Luo-Luo	0.019	7.00
0.1Luo-Luo	0.019	7.79
Luo-Lehr	0.019	7.79
Exp	0.038	14.60
Luo-Luo	0.038	9.56
0.3Luo-Luo	0.038	11.85
0.2Luo-Luo	0.038	12.51
0.1Luo-Luo	0.038	13.76
Luo-Lehr	0.038	13.6

4.5 Conclusion

In this work, 2D-axisymmetric simulations of a bubbling column were performed and the simulated time-averaged radial profiles were compared with the empirical data obtained from Hills (1974). The investigated superficial gas velocities were 0.019 m/s and 0.038 m/s, covering the homogeneous bubbly regime. The developed model consisted of a two-fluid model coupled with a population balance model. The former included the gas-liquid interface that considered the drag, lift, wall lubrication and turbulent dispersion forces. The latter involved the Luo bubble coalescence model as well as two different bubble breakup models: Luo and Lehr. From this work, the following conclusions could hence be formulated:

The sensitivity analysis of the bubble classes was performed using 14 bins, 20 bins, and 22 bins and it was shown that the solution was independent of the bubble classes. Hence, the lowest number of bubble classes were selected to reduce computational cost.

Verification of the numerical schemes was performed using first and second orders and results showed that numerical schemes had no significant influence on the predicted radial profiles of gas holdup and axial liquid velocity. However, at the center of the column, a slight discrepancy was observed, which might be related to numerical diffusion.

Mesh sensitivity was conducted on 1.5 mm (finer), 3 mm (medium) and 6 mm (coarse) mesh sizes. The predicted axial liquid profile of coarse (6 mm) mesh size differed from medium and fine mesh size, and hence was ignored. The fine meshing showed a non-realistic behavior near the wall without the inclusion of wall lubrication force, which might be related to the y^+ value of 12.5 and once introduced, there was no significant difference between fine- and medium-sized mesh. In addition, the predicted axial liquid velocity slightly improved at the core of the bubble column.

The combination of the Luo coalescence and Luo breakup kernels (Luo-Luo) was shown to under-predict the gas holdup both at a 0.019 m/s and 0.038 m/s superficial gas velocity. The gas holdup was increased to a maximum when the coalescence parameter was reduced. However, at the lowest Ug and the c_0 (=0.1) values, the predicted velocity profile was far away from the experimental values. It is thus recommended to tune the coalescence parameter when using the Luo-Luo kernels and both the holdup and axial liquid profiles should be considered for validation purposes.

Simulations using a combination of the Luo coalescence and Lehr breakup kernels (Luo-Lehr) predicted a closer holdup both for the 0.019 m/s and 0.038 m/s superficial velocities when compared with experiments. Scaling of coalescence parameter, in combination with the Lehr model leads to no significant improvement in the gas holdup. Furthermore, a decrease of the coalescence parameter significantly influences the axial liquid profile that under-predicts the profile compared to experiments. Results have shown that it is better to use Luo-Lehr kernels without any modification of the coalescence parameter.

5 CFD SIMULATIONS OF A SLURRY BUBBLE COLUMN: EFFECT OF POPULATION BALANCE KERNELS

Abstrait

Dans ce travail, les simulations CFD d'une colonne de bulle à bulle ont été réalisées et validées avec des données expérimentales. Les vitesses de gaz superficielles étudiées dans les expériences étaient de 5 cm / s et de 8 cm / s. Le chargement solide variait de 7% à 14% et le diamètre de la colonne de 0,14 m à 0,26 m. Un modèle d'équilibre de la population (PBM) a été mis en place et résolu numériquement selon la méthode de la classe des bulles. Les noyaux de fermeture impliquaient le modèle de coalescence de Luo ainsi que deux modèles de rupture différents: les modèles Luo et Lehr. La théorie cinétique des écoulements granulaires (KTGF) a été utilisée pour calculer la viscosité solide locale. Le cadre eulérien a été sélectionné pour les calculs multiphasés et le transfert de moment de l'interphase pour les conditions de traînée, de levage et de dispersion turbulentes inclus dans le gaz liquide. L'interphase liquide-solide impliquait à la fois des conditions de dispersion et de dispersion turbulente. Les résultats ont montré que: (a) Une combinaison des noyaux de fusion Luo et de Luo (Luo-Luo) peut prédire des tendances similaires pour le profil radial de la vitesse axiale solide en ce qui concerne les expériences. Cependant, à la vitesse de gaz superficielle la plus élevée dans la petite colonne, un écart a été observé dans les résultats. (B) Une combinaison de coalescence de Luo et de noyaux de rupture de Lehr (Luo-Lehr) a prédit des tendances similaires pour les vitesses solides par rapport aux données empiriques, mais cette combinaison montre également une divergence à la plus haute vitesse superficielle testée dans la petite colonne. (C) L'attelage total du gaz dans les modèles Luo-Luo et Luo-Lehr est inférieur et prédit respectivement par rapport aux résultats expérimentaux. (D) Les résultats de la sensibilité au maillage ont montré qu'une maille de 3 mm est réaliste pour capturer les champs d'écoulement. (E) L'analyse de sensibilité du nombre de classes de bulles a montré que les profils radiaux étaient indépendants du nombre de classes de bulles. Cependant, le plus grand nombre de classes couvre les formations des plus grandes bulles.

Auteurs et affiliation

Syed Alizeb Hussain: Département de génie chimique et de génie biotechnologique, Faculté de Génie, Université de Sherbrooke. La Chaire de Recherche Industrielle sur l'Éthanol Cellulosique et les biocommodités (CRIEC-B).

Tommaso Melchiori: Département de génie chimique et de génie biotechnologique, Faculté de Génie, Université de Sherbrooke. La Chaire de Recherche Industrielle sur l'Éthanol Cellulosique et les biocommodités (CRIEC-B).

Micael Boulet: Enerkem Inc., Sherbrooke, Québec, Canada.

Jean-Michel Lavoie : Département de génie chimique et de génie biotechnologique, Faculté de Génie, Université de Sherbrooke. La Chaire de Recherche Industrielle sur l'Éthanol Cellulosique et les biocommodités (CRIEC-B).

Date de soumission : 13th July 2017

Revue: Computers and Fluids

Titre en français: Simulations CFD d'une colonne de bulle de boue: effet des grains de la balance de la population.

CFD Simulations of a Slurry Bubble Column: Effect of Population Balance Kernels

Abstract

In this work, CFD simulations of a slurry bubble columns were performed and validated with experimental data. The superficial gas velocities investigated in the experiments were 5 cm/s and 8 cm/s. The solid loading varied from 7 % to 14 % and the column diameter from 0.14 m to 0.26 m. A population balance model (PBM) was implemented and solved numerically using the bubble class method. The closure kernels involved the Luo coalescence model as well as two different breakup model: Luo's and Lehr's models. The kinetic theory of granular flows (KTGF) was used to calculate the local solid viscosity. The Eulerian framework was selected for multi-phase calculations and the interphase momentum transfer for gas-liquid included drag, lift, and turbulent dispersion terms. The liquid-solid interphase involved both drag and turbulent dispersion terms. Results showed that: (a) A combination of the Luo coalescence and Luo breakup kernels (Luo-Luo) can predict similar trends for the radial profile of solid axial velocity with regards to experiments. However, at the highest superficial gas velocity in the small column, the discrepancy was observed in the results. (b) A combination of Luo coalescence and Lehr breakup kernels (Luo-Lehr) predicted similar trends for the solid velocity when compared to empirical data, however, this combination also shows discrepancy at the highest superficial velocity tested in the small column. (c) The total gas holdup in the Luo-Luo and Luo-Lehr models are under and over predicted respectively when compared with the experimental results. (d) The mesh sensitivity results showed that a 3 mm mesh size is realistic to capture the flow fields. (e) The sensitivity analysis of the number of bubble classes showed that the radial profiles were independent of a number of bubble classes. However, the highest number of classes cover the formation of largest bubbles.

Keywords: Population balance model (PBM); Bubble size distribution; Kinetic theory of granular flows model (KTGF); Time-average radial profiles of a holdup (gas and solid) and axial solid velocity; Bed expansion; Slurry Bubble column.

5.1 Introduction

Slurry bubble columns are extensively used in a wide range of industrial applications such as chemistry, biochemistry and process engineering. Some of the applications of slurry bubble column include but are not limited to waste-water treatment, methanol synthesis, Fischer-Tropsch synthesis and single-cell protein production (Lee & Liang-Shin 2002). Some of the key advantages of slurry column include significant heat transfer property so that they can be used for exothermic reactions as well as for an easy removal of slurry for catalyst regeneration when compared to fixed bed, they are also easier to build due to the absence of moving parts inside the reactor (Shah et al. 1982; Shaikh & Al-Dahhan 2013). However, bubble columns have some disadvantages which are essentially related to back-mixing, foaming, and the necessity to separate liquid and solid phases (Deckwer 1992). Since there is no moving part inside a bubble column, the gas flow rate dictates both the phase interaction (gas, liquid and solid) and flow regime. Industrial slurry columns are often operated at elevated superficial velocity and the flow regime is heterogeneous in such cases. In this regime, a wide spectrum of bubble sizes occur due to bubble coalescence, growth, and breakage, which complicate such systems (Liang-Shin & Yang 2003). Furthermore, studies concluded that the presence of solid phase lowers the gas holdup (Sada et al. 1986; Swart et al. 1996; Fan et al. 1999). Gandhi et al. (1999) simulated the slurry bubble column using the elevated solid loading and reported that the decrease in a gas holdup is due to lower breakup rate, which ultimately reduces the formation of small bubbles and supports the formation of large bubbles in the system. However, Ojima et al. (2014) suggested that the presence of solid phase promotes bubble coalescence hence decreasing the gas holdup. Rabha et al. (2013) showed that both the gas holdup and bubble size distribution change depending on the solid loading. One way to understand such complex phenomena in a slurry bubble column is by using computational fluid dynamics (CFD) tool.

The former has been used by many authors to investigate such multidimensional multiphase flow (Matonis et al. 2002; Gamwo et al. 2003; Rabha, Schubert & Hampel 2013). In literature, the most commonly used framework in CFD is the Eulerian-Eulerian approach because of the lower computational cost when compared to the Lagrangian or the volume of fluid approaches. Slurry bubble columns are often simulated as either pseudo-two-phase or three-phase system (Li & Zhong 2015). The former approach considers liquid and solid as a single continuous phase (slurry) while

the gas is the disperse phase. The density and viscosity of the slurry phase are computed from a correlation that is a function of the solid loading and the phase fraction (Troshko & Zdravistch 2009). This approach assumes that the solid is well dispersed (homogenous) inside the system and it is valid when the particle size is smaller than the bubble size. One of the drawbacks of this approach is that it cannot predict sedimentation, also liquid-solid and particle-particle interactions are neglected (Xu et al. 2014). In the latter approach, fluids are considered as an individual phase, which requires solving one momentum equation for each phase separately. The interactions between phases are defined by the exchange terms in the momentum equations.

The latter includes drag and non-drag forces. The former influences the macroscopic structure of the flow fields and depends on the Reynolds number, Eotvos numbers, terminal velocity of bubbles and turbulent intensity of the continuous phase (Wang & Yao 2016; Giorgio et al. 2017). The non-drag forces commonly include the lift, wall lubrication, and turbulent dispersion. These forces also influence the radial profiles significantly as reported by Yamoah et al. (2015). In case of lift force, the shape of the radial profile may change depending on the sign of the lift coefficient. According to Tomiyama (2004), small bubbles (db <5.8 mm) have a positive lift coefficient and tend to go towards the wall. However, larger bubbles have a negative lift coefficient and tend to stay at the core of bubble column. Zhang et al. (2005 and 2006) suggested that the inclusion of the Tomiyama lift coefficient predicts a better correlation with experimental values. Lucas et al. (2007) also studied the influence of non-drag forces using 1D-model and suggested that the inclusion of the lift and turbulent dispersion forces improve the results when compared with the experimental profiles.

In a three-phase system, the interactions between fluids involve gas-liquid, liquid-solid, and gas-solid. Some authors considered only the gas-liquid and liquid-solid interactions and their results predicted similar trend with experimental values (Matonis et al. 2002; Rampure et al. 2003). However, they considered a constant bubble size which might not be appropriated due to the presence of a large spectrum of bubble sizes. The gas-liquid, liquid-solid and gas-solid interactions have also been reported by some authors (Michele & Hempel 2002; Schallenberg et al. 2005), however, one of the drawbacks of such approach is that it tends to over-estimate the gas holdup (Xu et al. 2014). Furthermore, when the particle size is lower than 587 microns (Stokes number< 1) there is no interaction between the gas and solid phases (Hooshyar et al. 2013). The kinetic

theory of granular flows (KTGF) approach has also been reported in the literature to calculate the local properties of the solid phase in slurry column (Gamwo et al. 2005; Li & Zhong 2015; Zhou et al. 2017). KTGF is a closure model for the transport equation of the solid phase and it is based on the kinetic theory of dense gases. This approach considers the particle-particle interaction and predicts the local solid viscosity, stresses, and pressure.

Laborde-Boutet et al. (2009) focused on a multiphase turbulent model using a k-ε model. Their studies showed that the Renormalization Group (RNG k-ε) predicts higher turbulent dissipation rate as compared to Standard k-ε, which is known to be underestimated (Jakobsen et al. 2005). Most coalescence and breakup kernels depend on the local turbulent dissipation rate. Therefore, the Laborde-Boutet suggested that the RNG k-ε turbulent model should be used for the implementation of a population balance model (PBM). The latter is usually discretized into N-classes to cover the wide spectrum of bubble sizes and is coupled with a two-fluid model. The source terms of PBM are bubble coalescence and breakup kernels and in literature, the most commonly reported kernels are the Luo (1993) coalescence model and Luo & Svendsen (1996) and Lehr et al. (2002) breakage models. The Luo coalescence model depends only on the turbulent parameter and ignores any buoyancy-driven and laminar shear stress collisions. The breakage models (Luo & Svendsen 1996; Lehr et al. 2002) do not require a daughter size distribution, hence the implementation is straightforward. Wang et al. (2003 and 2005) studied the effect of different coalescence and breakup kernels. Their studies show that the Luo breakup (Luo & Svendsen 1996) predicts a lower breakup rate, while the Lehr kernel (Lehr et al. 2002) predicts a higher breakup rate. In both kernels, the key difference is in the estimation of the breakup efficiency. The Luo breakage model includes the energy constraint while ignoring capillary constraint for bubble breakup, meaning that the break-up could only occur if the kinetic energy of the colliding eddy is higher than the surface energy necessary for bubble breakage. However, The Lehr breakage model only considers the capillary constraint, assuming that the interfacial and inertial forces balance each other. The influence of the solid phase on the bubble breakup behavior could be neglected if the particle size is lower than the bubbles size (Ye-Mon Chen & Liang-Shin 1989).

Most of the previous reports studying three-phase system are based on a constant bubble size for gas phase and the KTGF approach for the solid viscosity. The former constant size assumption is non-realistic as mentioned earlier since the heterogeneous regime involves a large spectrum of

bubble sizes. Some reports do involve bubble size distribution using PBM in a slurry bubble column. However, they considered the solid viscosity as either a constant or calculated from the correlations (Thomas 1965; Saxena & Z. D. Chen 1994), ignoring particle-particle interaction.

In this work, a PBM approach was chosen for validation related to the gas phase while the KTGF approach was used for the solid phase. The influence of the different breakage kernels in a three-phase system using different operating conditions (column diameters, superficial velocity, and solid loading) were slightly investigated in the literature. Furthermore, most of the CFD-simulations were performed on a two-phase flow and fewer publications were made on the three phases using the KTGF state-of-the-art modeling approach. Hence, this paper will focus on:

- The influence of the breakup kernels (Luo's and Lehr's models) on the radial profiles of solid axial velocity and the total gas holdup
- The influence of the column diameter
- The sensitivity analysis of the bubble classes
- The dependency of the mesh size on the predicted profiles

All simulations of three-phase bubble column will be performed on a 2D-axisymmetric geometry. The predicted time-averaged solid axial velocity profiles will then be compared with data published by Sannaes (1997). The empirical work involved two column diameters with 0.14 m and 0.26 m operating with superficial gas velocities of 5 cm/s and 8 cm/s using solid loading of 7% and 14%. ANSYS-Fluent v.17.2 was used for all CFD simulations.

5.2 Model Development

5.2.1 Three-Fluid Model and Interphase

In the Table 5-1 and Table 5-2 all the transport equations and the interface momentum transfers between phases (gas, liquid and solid) used in the three-fluid model are shown. The liquid phase was considered as a continuous media while rest of the fluids (gas and solid) were simulated as disperse phase. The closure for the solid phase was modeled by the KTGF approach to compute the local pressure, viscosity, and stresses. The interface momentum transfer between gas and liquid phases involved the drag, lift, and turbulent dispersion forces. The liquid-solid interaction included the drag and turbulent dispersion forces. The turbulence model consisted of Renormalization Group (RNG) k-epsilon model and it was solved for a mixture phase. The population balance approach was considered for the gas phase in order to capture a large spectrum of the bubble sizes and was discretized using the class method. A short descriptions of the interphase forces and population balance model are mentioned below.

5.2.2 Drag Force

The drag force is generated from the slip velocity between phases. For gas-liquid interphase, the drag coefficient involved Ishii model (Ishii & Zuber 1979). The latter considers a wide range of bubble size, in addition, it varies according to the flow regime (viscous, distorted and capped regime). The latter depends on the local Reynolds and Eötvö numbers. The drag force between liquid and solid involves Gidaspow et al. (1992) formulation, which covers a wide range of volume fraction and depending on the flow regime, different drag coefficients are used. Gidaspow's correlation is the combination of the Wen & Yu model and the Ergun equation. If the volume fraction of the solid phase represents less than 20% of the total volume, the Wen & Yu formulation is considered and the latter is based on Stokes drag coefficient using the particle's Reynolds number. If the phase fraction exceeds 20%, the Ergun formulation is used. The latter is derived from packed-bed pressure drop expressions.

5.2.3 Lift Force

In the gas-liquid system, a perpendicular force is applied on the upward rising bubbles, this force is called transverse or lift force. The latter is calculated by taking into account the disperse phase fraction, the density of the continuous phase, the relative velocity between phases, the velocity gradients and the lift coefficient. This lift coefficient plays an integral role in term of the radial

profiles of gas holdup and liquid velocity. The direction of the bubbles changes if the lift coefficient has a positive or negative value. Small bubbles (db <5.8 mm) are known to have a positive lift coefficient and tend to go towards the lowest liquid velocity (i.e. the wall). Larger bubbles, however (db > 5.8 mm) are generally associated with a negative value and tend to stay at the core of bubble column (Tomiyama 2004).

5.2.4 Turbulent Dispersion

The turbulent dispersion force accounts for the interaction between turbulent eddies and the disperse phase. This force transports the disperse phase from the most to the least concentrated regions. The averaging of the instantaneous interface drag force gives mean and the fluctuating component of the drag force. The latter is known as turbulent dispersion force. Yamoah et al. (2015) and Wang & Yao (2016) studied the Simonin & Viollet (1990), Bertodano. (1991) and Burns et al. (2004) turbulent dispersion formulations and found no significant difference in the results. In this study, the dispersion force includes the Simonin formulation.

5.2.5 Population Balance Model (PBM)

In this work, the gas phase was considered as a poly-dispersed fluid considering the wide spectrum of bubble sizes. The PBM was discretized using a class method and a single momentum equation was solved for all bubble classes (homogeneous discrete method). On this aspect, Xu et al. (2013) found no difference in results when using homogeneous and non-homogeneous (with lift force) discrete methods. The bubble sizes were varied due to bubble coalescence and breakup only. In this study Luo's coalescence model (Luo 1993) as well as two different breakup kernels: Luo's and Lehr's model (Luo & Svendsen 1996; Lehr et al. 2002) were studied.

Table 5-1. Three-fluid model equations

Continuity equation $$\frac{\partial(\alpha_q\rho_q)}{\partial t} + \nabla.(\alpha_q\rho_q\boldsymbol{u}_q) = 0$$
Momentum equation (gas/liquid phase) $$\frac{\partial(\boldsymbol{u}_q\rho_q\alpha_q)}{\partial t} + \nabla.(\alpha_q\rho_q\boldsymbol{u}_q\boldsymbol{u}_q - \mu_q\alpha_q(\nabla\boldsymbol{u}_q + (\nabla\boldsymbol{u}_q)^T)) = -\alpha_q.\nabla p + \boldsymbol{F}_{pq} + \alpha_q\rho_q\boldsymbol{g}$$
Momentum equation (solid Phase) $$\frac{\partial(\boldsymbol{u}_s\rho_s\alpha_s)}{\partial t} + \nabla.(\alpha_s\rho_s\boldsymbol{u}_s\boldsymbol{u}_s - \mu_s\alpha_s(\nabla\boldsymbol{u}_s + (\nabla\boldsymbol{u}_s)^T)) = -\alpha_s.\nabla p - \nabla p_s + \boldsymbol{F}_{qs} + \alpha_s\rho_s\boldsymbol{g}$$
Solid phase pressure $$p_s = \alpha_s\rho_s\Theta_s + 2\rho_s(1+e_{ss})\alpha_s{}^2 g_{0,ss}\Theta_s$$
Radial distribution function $$g_{0,ss} = \left[1 - \left(\frac{\alpha_s}{\alpha_{s,max}}\right)^{1/3}\right]^{-1}$$
Solid Shear Stresses $$\mu_s = \mu_{s,collision} + \mu_{s,kinetic} + \mu_{s,frictional}$$
Collision viscosity $$\mu_{s,collision} = \frac{4}{5}\alpha_s\rho_s d_s g_{0,ss}(1+e_{ss})\left(\frac{\Theta_s}{\pi}\right)^{1/2}\alpha_s$$
Kinetic viscosity $$\mu_{s,kinetic} = \frac{\alpha_s\rho_s d_s\sqrt{\Theta_s\pi}}{6(3-e_{ss})}\left[1 + \frac{2}{3}(1+e_{ss})(3e_{ss}-1)\alpha_s g_{0,ss}\right]$$
Frictional viscosity $$\mu_{s,frictional} = \frac{p_s sin\emptyset}{2\sqrt{I_{2D}}}$$
Bulk viscosity $$\lambda_s = \frac{4}{3}\alpha_s{}^2\rho_s d_s g_{0,ss}(1+e_{ss})\left(\frac{\Theta_s}{\pi}\right)^{1/2}$$
Granular temperature $$\frac{3}{2}\left[\frac{\partial(\rho_s\alpha_s\Theta_s)}{\partial t} + \nabla.(\alpha_s\rho_s\boldsymbol{u}_s\Theta_s)\right] = \left(-p_s\bar{\bar{I}} + \bar{\bar{\tau}}_s\right):\nabla\boldsymbol{u}_s + \nabla.\left(k_{\Theta_s}\nabla\Theta_s\right) - \gamma_{\Theta_s} + \emptyset_{qs}$$
Diffusion coefficient for granular energy $$k_{\Theta_s} = \frac{15\alpha_s\rho_s d_s\sqrt{\Theta_s\pi}}{4(41-33\eta)}\left[1 + \frac{12}{5}\eta^2(4\eta-3)\alpha_s g_{0,ss} + \frac{16}{15}(41-33\eta)\eta\alpha_s g_{0,ss}\right]$$
The mixture RNG k-epsilon $$\frac{\partial(\rho_m k)}{\partial t} + \nabla.(\rho_m\boldsymbol{u}_m k) = \nabla.\left(\left(\mu_m + \frac{\mu_{t,m}}{\sigma_k}\right)\nabla k\right) + G_{k,m} - \rho_m\varepsilon$$ $$\frac{\partial(\rho_m\varepsilon)}{\partial t} + \nabla.(\rho_m\boldsymbol{u}_m\varepsilon) = \nabla.\left(\left(\mu_m + \frac{\mu_{t,m}}{\sigma_\varepsilon}\right)\nabla\varepsilon\right) + \frac{\varepsilon}{k}\left(C_{1\varepsilon}G_{\varepsilon,m} - C_{2\varepsilon}\rho_m\varepsilon\right)$$
Population balance model and volume gas fraction $$\frac{\partial}{\partial t}n_i + \nabla.(\boldsymbol{u}_i n_i) = \sum_{d_j=d_i}^{d_{max}}\Omega_B(d_j:d_i) - \Omega_B(d_i) + \sum_{d_j=d_{min}}^{d_i/2}\Omega_C(d_j:d_i-d_j) - \sum_{d_j=d_{min}}^{d_{max}-d_i}\Omega_C(d_j:d_i)$$ $$\alpha_g = \sum_{i=1}^{N} n_i\frac{\pi}{6}d_i^3$$
Luo coalescence kernel $$\Omega_C(d_i:d_j) = c_0(d_i+d_j)^2\left(d_i{}^{2/3} + d_j{}^{2/3}\right)^{1/2}\varepsilon^{1/3}n_i n_j\ exp\left\{-\frac{t_c}{t_f}\right\}$$
Luo breakup kernel $$\Omega_B(d_i:d_j) = 0.9238\varepsilon^{1/3}d_i^{-2/3}\alpha\int_{\xi_{min}}^{1}\frac{(1+\xi)^2}{\xi^{\frac{11}{3}}}exp\left(\frac{12\sigma c_f}{\rho_l\varepsilon^{2/3}d_i^{5/3}}\xi^{-11/3}\right)d\xi$$ $$\Omega_B(d_i) = \int_0^1\Omega_B(d_i:d_j)df$$
Lehr breakup kernel $$\Omega_B(d_i:d_j) = \frac{1.19\sigma}{\rho_l\varepsilon^{1/3}d_i^{7/3}f^{1/3}}\int_{\xi_{min}}^{1}\frac{(1+\xi)^2}{\xi^{\frac{13}{3}}}exp\left(\frac{2\sigma We_{crit}}{\rho_l\varepsilon^{2/3}d_i^{5/3}f^{1/3}}\xi^{-2/3}\right)d\xi$$ $$\Omega_B(d_i) = \int_0^1\Omega_B(d_i:d_j)df$$

Table 5-2 Interphase momentum transfer

Drag forces (gas-liquid)

$$\boldsymbol{F}_{D,pq} = -\frac{3}{4}\alpha_p\alpha_q\rho_q\frac{C_D}{d_p}|\boldsymbol{u}_p - \boldsymbol{u}_q|(\boldsymbol{u}_p - \boldsymbol{u}_q)$$

For viscous regime $[C_{D,dis} < C_{D,vis}]$,

$$C_{D,vis} = \frac{24}{Re}(1 + 0.1Re^{0.75})$$

For distorted regime $[C_{D,vis} < C_{D,dis} < C_{D,cap}]$,

$$C_{D,dis} = \frac{2}{3}d_p\sqrt{\frac{g\Delta\rho}{\sigma}}\left(\frac{1 + 17.67f^{*\frac{6}{7}}}{18.67f^*}\right), \qquad f^* = (1-\alpha_p)^{1.5}$$

For capped regime $[C_{D,dis} > C_{D,cap}]$,

$$C_{D,cap} = \frac{8}{3}(1-\alpha_p)^2$$

Drag forces (liquid-solid)

$$\boldsymbol{F}_{D,qs} = K_{q,s}(\boldsymbol{u}_q - \boldsymbol{u}_s)$$

$$K_{q,s} = \frac{3}{4}\alpha_s\alpha_q\rho_q\frac{C_{D,qs}}{d_s}|\boldsymbol{u}_q - \boldsymbol{u}_s|\alpha_q^{-2.65}, \qquad \alpha_q > 0.8$$

$$C_{D,qs} = \frac{24}{\alpha_q Re_s}\left[1 + 0.15(\alpha_q Re_s)^{0.687}\right]$$

$$K_{q,s} = 150\frac{\alpha_s(1-\alpha_q)\mu_q}{\alpha_q d_s^2} + 1.75\frac{\alpha_s\rho_q|\boldsymbol{u}_q - \boldsymbol{u}_s|}{d_s}, \qquad \alpha_q \le 0.8$$

Lift force (gas-liquid

$$\boldsymbol{F}_L = -C_L\alpha_p\rho_q(\boldsymbol{u}_p - \boldsymbol{u}_q)(\boldsymbol{\nabla}\boldsymbol{u}_q)$$

$$C_L = \begin{cases} \min\left[0.288\tanh(0.121Re, f(Eo')\right], for\ Eo' \le 4 \\ f(Eo'), \qquad for\ 4 \le Eo' \le 10 \\ -0.27 \qquad for\ 10 \le Eo' \end{cases}$$

Turbulent dispersion force

$$\boldsymbol{F}_{td,q} = -\boldsymbol{F}_{td,p} = C_{TD}K_{pq}\frac{D_{t,pq}}{\sigma_{pq}}\left(\frac{\nabla\alpha_p}{\alpha_p} - \frac{\nabla\alpha_q}{\nabla\alpha_q}\right)$$

5.3 Numerical Setup

All simulations were run on a 2D axis-symmetric geometry since experimental data of Hills (1974) and Degaleesan (1997) showed that a time-averaged flow fields produce a stationary axis-symmetric flow pattern. This assumption was also used by other authors (Grevskott et al. 1996; Wang et al. 2006; Liu & Hinrichsen 2014), hence supporting the validity of 2D modeling. Simulations were performed using the experimental data published by Sannaes (1997) as a validation point. The three phases involved in the experiments were air, water, and glass beads.

Two column diameters of 0.14 m and 0.26 m were considered and the mean diameter and density of the glass bead in Sannaes's work were 151 microns and 2965 kg/m^3 respectively. In our studies, the tested superficial gas velocities were of 5 cm/s and 8 cm/s while the solid loading was varied from 7 % to 14% using both column diameters. The static and dynamic heights of the slurry bed and the overview of the experimental cases, which were considered for the simulations is mentioned in Table 5-5. The exact configuration of the experimental inlets are reported in Table 5-3. However, in simulations, the gas is assumed to be introduced uniformly from the bottom of the column a simplification that was also reported by Chen et al. (2005). The boundary conditions for the PBM involve a uniform inlet bubble size that was calculated from Kumar et al. (1976) correlation while the bubble volume of each PBM class was calculated from the following formula:

$$\frac{v_{i+1}}{v_i} = 2^q$$

Where q is the ratio factor and is equal to 1, 2…n. The first order schemes were used to discretize all transport equations and fixed time steps (1E-04 sec) were used and guaranteed that the Courant numbers is lower than 1 to avoid numerical diffusion. The outlet and wall boundary conditions include atmospheric pressure and non-slip condition respectively. The turbulence parameters near the wall involve Launder & B. Spalding (1974) formulation and it is given as:

$$U^* = \frac{1}{k}\ln(Ey^*)$$

Where $U^*, k, E \text{ and } y^*$represents dimensionless mean velocity, Von Karman constant (=0.4187), empirical constant (=9.793) and dimensionless wall distance respectively. The former is calculated from the following correlation as:

$$y^* = \frac{\rho_q C_\mu^{1/4} k_p^{1/2} y_p}{\mu_q}$$

Where $\rho_q, C_\mu, k_p, y_p \text{ and } \mu_q$ represents the density of the continuous phase, constant (=0.09), turbulent kinetic energy at the point P, distance from point P to the wall, and phase viscosity respectively. The point 'P' is the centroid of the cell adjacent to the wall. The log-law correlation is employed when y^*>11.225. The presented results were axially averaged over z/L= 0.5 to 0.8, in order to have a consistent comparison with the experimental data. Here 'L' is the dynamic height

of the slurry. Furthermore, the time-averaged sampling was calculated for 30s, after a statistically steady state was reached.

Table 5-3 Configurations of gas inlet geometries, numbers of holes, hole diameters and patterns, which were considered in the experiments

Column diameter [cm]	Number of holes	Hole diameter [cm]	Pattern
14	61	0.04	3 concentric circle 1.5 cm apart
26	193	0.07	8 concentric circle 1.5 cm apart

5.4 Results and Discussions

5.4.1 Mesh and Number of Bubble Classes (Bins) Sensitivity

A mesh sensitivity was performed, simulating the 0.14 m column diameter and using a 5 cm/s superficial gas velocity at a 14% solid loading. The bubble coalescence and bubble breakup models (Luo and Lehr) were used for the simulations. For the latter three mesh sizes were selected: 3 mm x 3 mm (fine), 4 mm x 4 mm (medium) and 6 mm x 6 mm (coarse) yielding a total number of cells in the fine, a medium and coarse mesh of 10488, 6192, and 2748 respectively. Fig. 5-1 shows that the coarse mesh size predicts a higher solid axial velocity at the core of the bubble column, which might be related to numerical diffusion. This behavior is minimized as the mesh size decreases. In case of finer mesh size, the predicted solid axial velocity is close to experiment, as it is shown in Table 5-4. The area-weighted mean relative difference of solid axial velocity is calculated and compared with experiments and simulations. Results show that the fine mesh predicts the lowest value (4.8%) of relative difference when compared with experiments. Therefore, fine mesh (3mm) is selected for the rest of the simulations.

The sensitivity analysis related to the number of bubble classes (bins) were performed using three different distributions of bubble sizes: 1 mm to 56 mm, 1 mm to 76 mm and 1 mm to 103 mm. These ranges were divided into 15, 16 and 17 classes (bins), respectively. The addition of each bubble class, solves one more partial differential equation, hence making the solution computational expensive. This analysis on number of bubble classes were performed for column diameter of 0.14 m with a solid loading of 7% that used an elevated superficial gas velocity (8 cm/s) in which a large spectrum of bubble sizes is prominent. Fig. 5-2, compares the predicted bubble size distribution (BSD), which is averaged in radius and plotted at a 0.9 m height, using

different number of bubble classes. At the lowest bubble class (15), the BSD is cut and does not take into account the formation of bubbles larger than 56 mm although practically, the BSD should cover all the bubble sizes. One possible solution would be to increase the bubble classes since at the highest bubble class (17), all the possible bubble sizes would be included in the BSD. Fig. 5-3, shows the influence of three different number of bubble classes on the radial profiles of gas holdup and solid axial velocity. Results show that the profiles remain unchanged. One of the reasons for this behavior is related to the Sauter-mean bubble diameter. The predicted area-weighted Sauter-mean bubble diameter in the 15, 16 and 17 bubble classes were 9.98 mm, 10.32 mm and 10.41 mm respectively. Since the average bubble sizes are quite a comparable one to the others, the radial profiles predicted by all three bubble classes are similar.

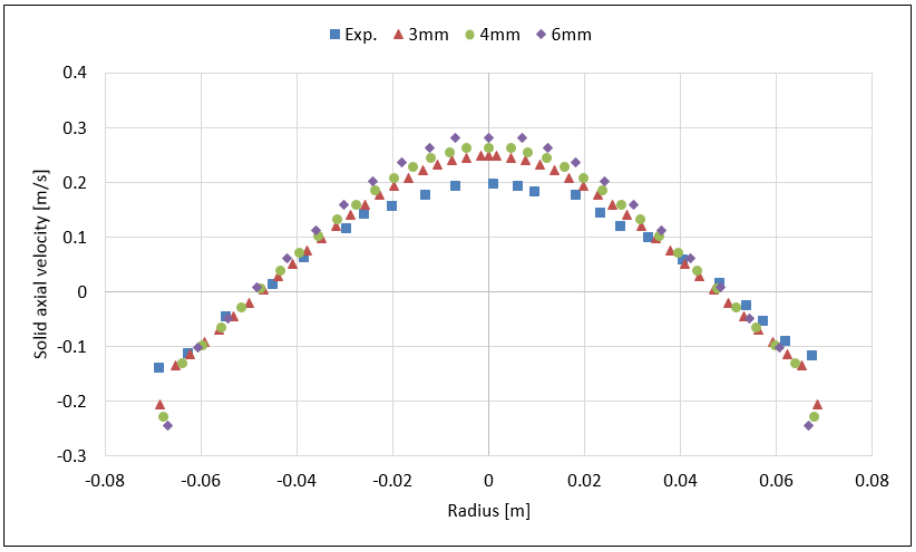

Fig. 5-1. Comparison of the radial profile of solid axial velocity obtained from three different mesh sizes with published data of Sannaes (1997) using a 5 cm/s superficial gas velocity at a 14% solid loading

Table 5-4 Area-weighted mean relative difference between experimental values of Sannaes (1997) and simulations obtained from three different mesh sizes using a 5 cm/s superficial gas velocity at a 14% solid loading

	Mean relative difference %
Exp. vs CFD-3mm	4.85
Exp. vs CFD-4mm	7.35
Exp. vs CFD-6mm	10.92
CFD: 6mm vs 4mm	3.35
CFD: 4mm vs 3mm	2.67
CFD: 3mm vs 6mm	7.73

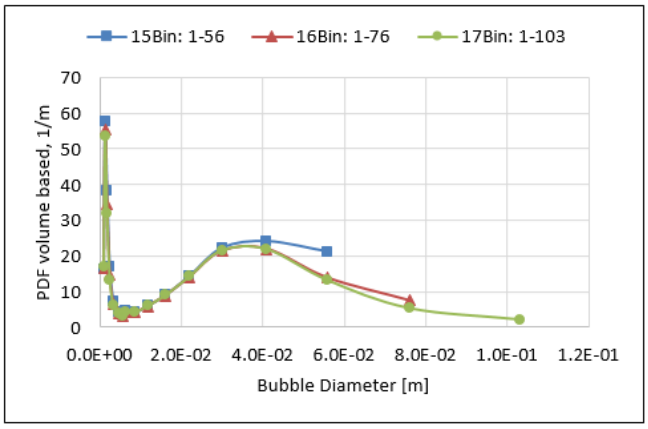

Fig. 5-2. Predicted radial-averaged bubble size distributions using different range of bubble sizes at 8 cm/s superficial gas velocity and 7% solid loading and plotted at 0.9 m height in 0.14 m column diameter

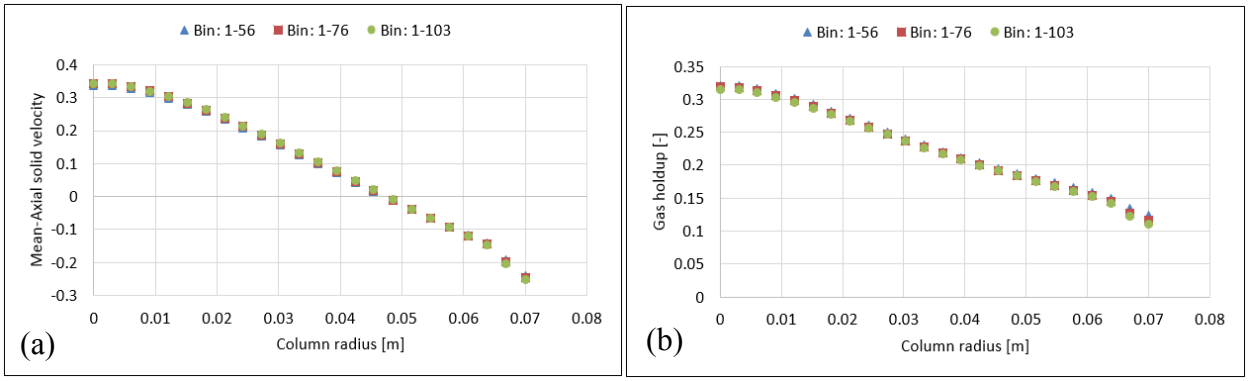

Fig. 5-3. Predicted radial profiles of mean-axial solid velocity (a) and mean-gas holdup (b) using three different range of bubble sizes at 8 cm/s Ug and 7% solid loading, plotted at 0.9 m height

5.4.2 Simulations with Luo's Coalescence and Luo's Breakup Models (Luo-Luo)

The chosen closure equations of the population balance model (PBM) involves the Luo coalescence model (Luo 1993) as well as two different breakup: Luo and Lehr models (Luo & Svendsen 1996; Lehr et al. 2002). In this section, the Luo coalescence and Luo breakup models (Luo-Luo) are discussed and compared with empirical values. Fig. 5-4, shows the comparison of solid axial velocity calculated with the Luo-Luo models and experiments in the 0.14 m column (small column) using 5 cm/s and 8 cm/s superficial gas velocities (Ug) and a 14% and 7% solid loadings respectively. At the highest Ug, the model over-predicts the solid axial velocity at the core of the column. One of the possible reasons is that experimentally, the fully developed regime was observed typically from z/L=0.5 to 0.8 (corresponding to 0.55 m to 0.88 m height). As for the simulations involving the Luo-Luo kernels, the fully developed regime is reached at 0.7 m height and upwards (as shown in Fig. 5-5a) which does not consist with the experiments. This limitation of the model might be related to either an intrinsic behavior of kernels or to the turbulent dispersion

force. The former was previously developed in a two-phase system although the influence of the solid phase on the bubble formations was not studied (Ojima et al. 2014). Furthermore, the bubble collision frequency in the Luo coalescence model only includes turbulent mechanism and ignores bouncy and shear-stress mechanisms (Yeoh et al. 2014). Hence, it produces large size bubbles and ultimately a higher bubble rise velocity. The turbulent dispersion force disperses the bubbles from the highest to the lowest region and influences the radial profiles (Lucas et al. 2007). Large bubbles tend to stay at the core of column due to a negative value of lift coefficient (Tomiyama 2004) hence a turbulent dispersion force is vital in dispersing the bubbles. Many authors (Masood & Delgado 2014; Yamoah et al. 2015; Wang & Yao 2016) have tuned the turbulent dispersion coefficient to match the results with experiments, hence there is no clear-cut coefficient that is well validated with empirical values. However, the evaluation of turbulent dispersion coefficient is not the focus of this study and it is subjected to future work. Fig. 5-6 shows the time-averaged gas volume fraction in the three-phase bubble column. Results show a delayed although fully developed region at the highest Ug value. Fig. 5-7a shows the predicted surface-averaged bubble size distribution (BSD) by Luo-Luo models, which is mono-modal in nature. As the superficial gas velocity increases the BSD moves towards the left-hand side and hence produces more small bubbles. However, an increase in Ug and the presence of solid phase promote the formation of large bubbles (Wang et al. 2006; Rabha, Schubert & Hampel 2013). Hence, the Luo-Luo models failed to produce the correct trend of bubble formations a tendency that was also witnessed by the Wang.

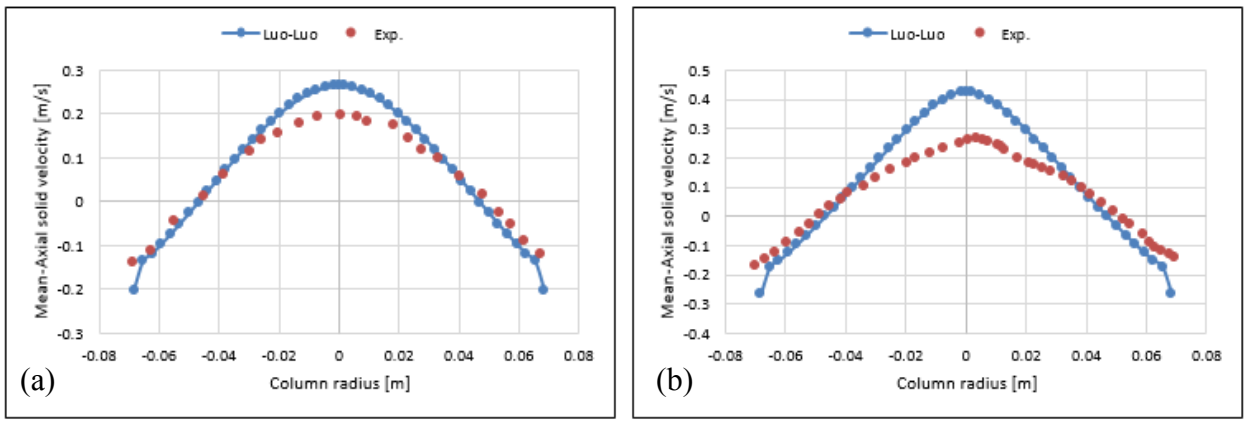

Fig. 5-4. Comparison of the radial profiles of solid axial liquid velocity with experimental data of Sannaes (1997) using (a) 5 cm/s and 14% solid loading; (b) 8 cm/s and 7% solid loading

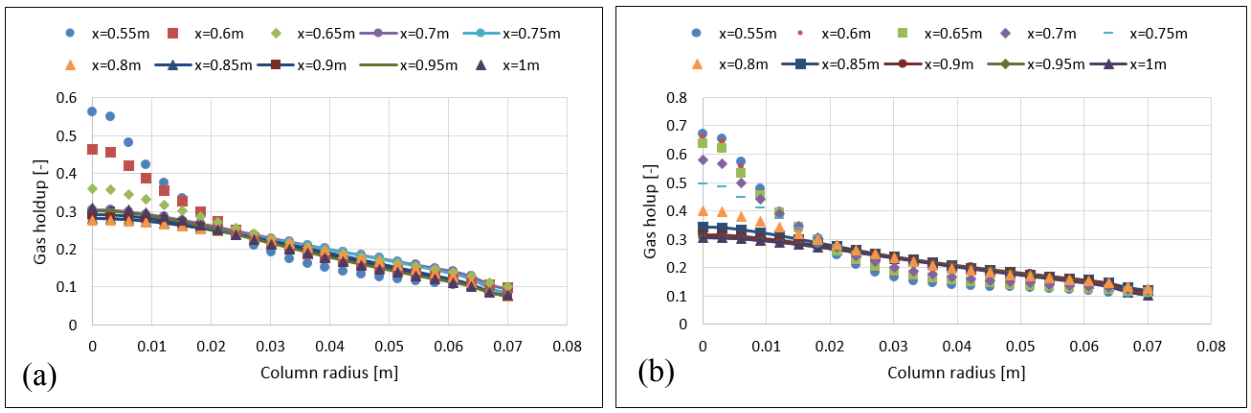

Fig. 5-5. Predicted radial profiles of the gas holdup at different axial positions 'x' using (a) Luo coalescence and Luo breakup models; (b) Luo coalescence and Lehr breakup models

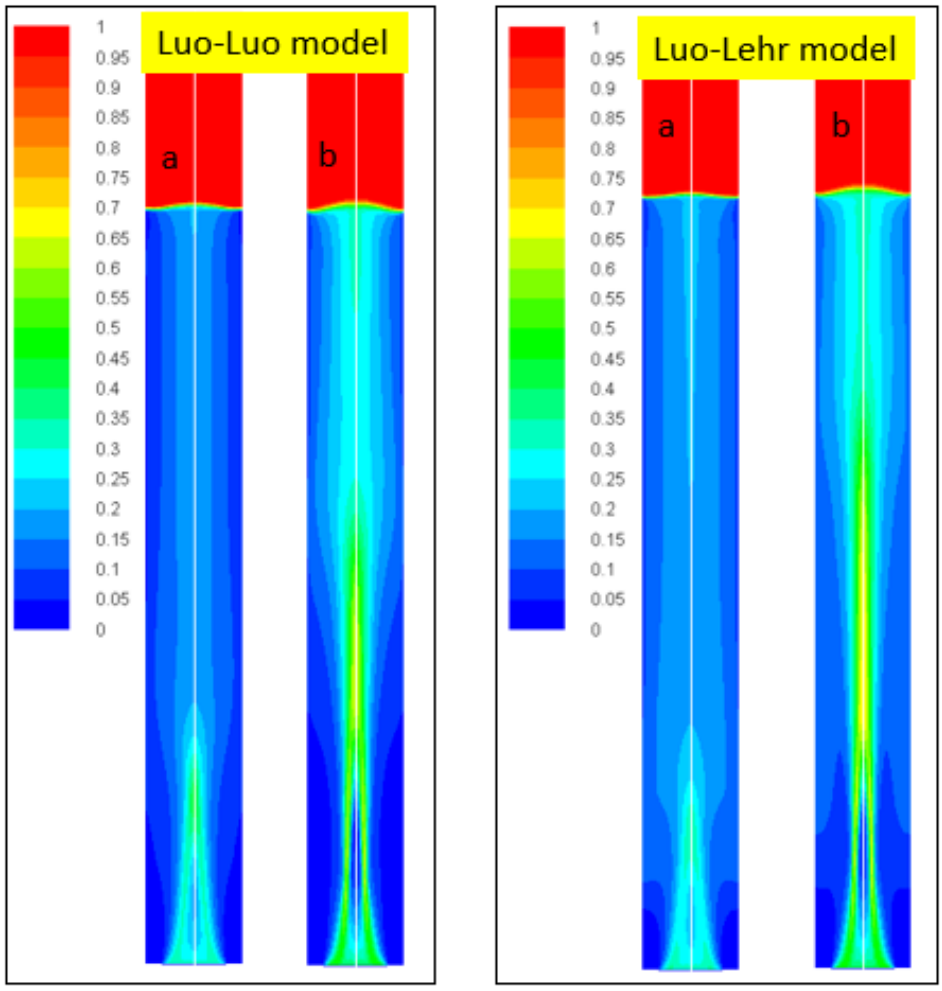

Fig. 5-6. Volume gas fraction simulated with Luo coalescence and Luo breakup models (Luo-Luo) and Luo coalescence and Lehr breakup models (Luo-Lehr) (a) 5 cm/s ug and 14 % solid loading; (b) 8 cm/s ug and 7 % solid loading

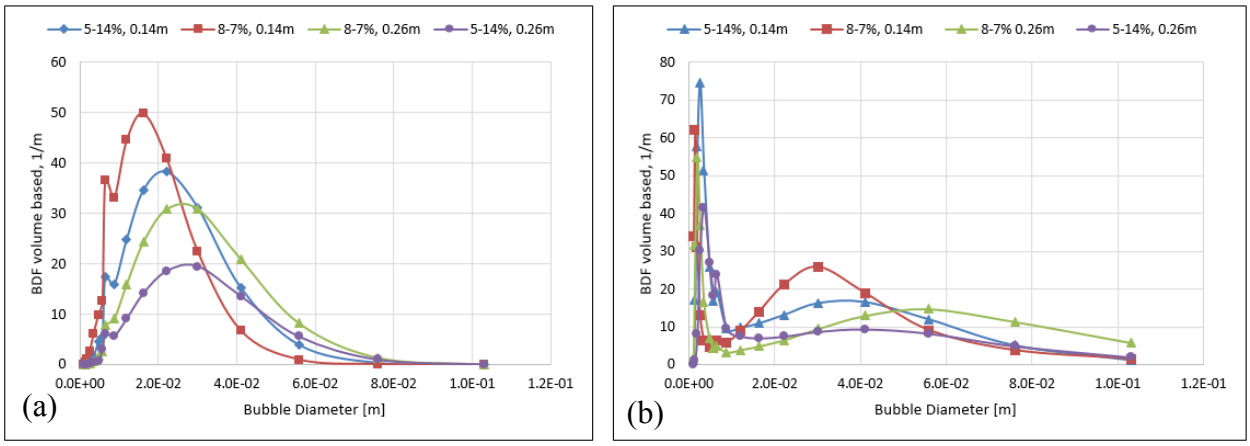

Fig. 5-7. Predicted bubble size distributions in 0.14 m and 0.26 m column diameters using (a) Luo-Luo kernels and (b) Luo-Lehr kernels

5.4.3 Simulations with Luo's Coalescence and Lehr's Breakup Models (Luo-Lehr)

Fig. 5-8 shows the comparison of simulated and measured solid axial velocity in a 0.14 m diameter column using superficial velocities of 5 cm/s and 8 cm/s with solid loadings of 14% and 7%, respectively. The predicted axial solid velocity profile is in good agreement with the experiments at the lowest Ug. However, at the highest Ug, significant discrepancy is observed at the core of the column between the predicted and empirical profiles. As discussed previously, the Luo-Lehr models also do not predict the fully developed region correctly. The fully developed region is reached at 0.85 m and upwards in simulations as shown in Fig. 5-5b and Fig. 5-6. The Lehr model predicts a bi-modal bubble size distribution (see Fig. 5-7b). At 5 cm/s and 8 cm/s Ug in the small column, the distributions show two peaks at the positions of 1.9 mm and 41 mm, and 1.4 mm and 30 mm respectively. Whereas at 8 cm/s Ug in the large column, the predicted position of the two peaks were at 1.9 mm and 56 mm respectively. As the superficial gas velocity increases, the formation of small bubbles decrease and the number of large bubbles increase. This behavior of PSD as well as the position of the peaks (lower and higher) are close to Wang et al. (2005) findings.

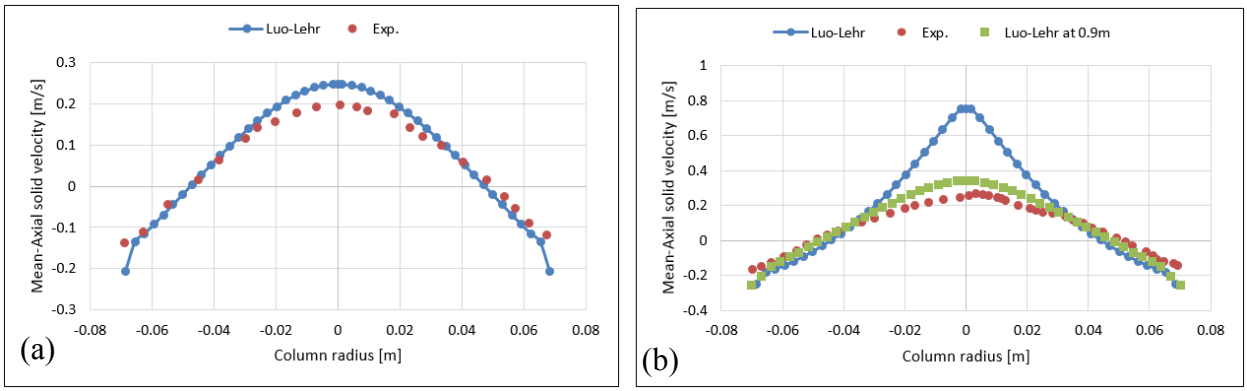

Fig. 5-8. Comparison of the radial profiles of solid axial liquid velocity with experimental data of Sannaes (1997) using (a) 5 cm/s and 14% solid loading; (b) 8 cm/s and 7% solid loading

5.4.4 Effect of Column Diameter

Fig. 5-9 shows the comparison between different axially averaged mean-axial velocity of the solid in a 0.26 m diameter column using combined calculation approaches: Luo coalescence and Luo breakup models (Luo-Luo) and Luo coalescence and Lehr breakup models (Luo-Lehr). At the lowest Ug, both combinations show a slight discrepancy compared to experiments, but overall predict similar velocity profiles trend. At the highest Ug, the predicted solid axial velocity profiles using Luo-Luo and Luo-Lehr models are in good agreement with the experimental values. Fig. 5-10 shows that the bubbles are well dispersed in the large column and the predicted radial profile of axial solid velocity does not change between 0.5 to 0.8 z/L (velocity profiles at different axial heights are not shown here because they were similar to Fig. 5-9), hence the fully developed region is achieved in both combinations and consistent with the experimental observations. This behavior of fully developed regime might be related to the inlet configuration in the 0.26 m diameter column, which involved large inlet size due to eight concentric circles (see Table 5-3), meaning that the bubbles are well dispersed across the column. This reduces the concentration gradient at the core of the column and hence, the model predicts a correct trend of the fully developed region.

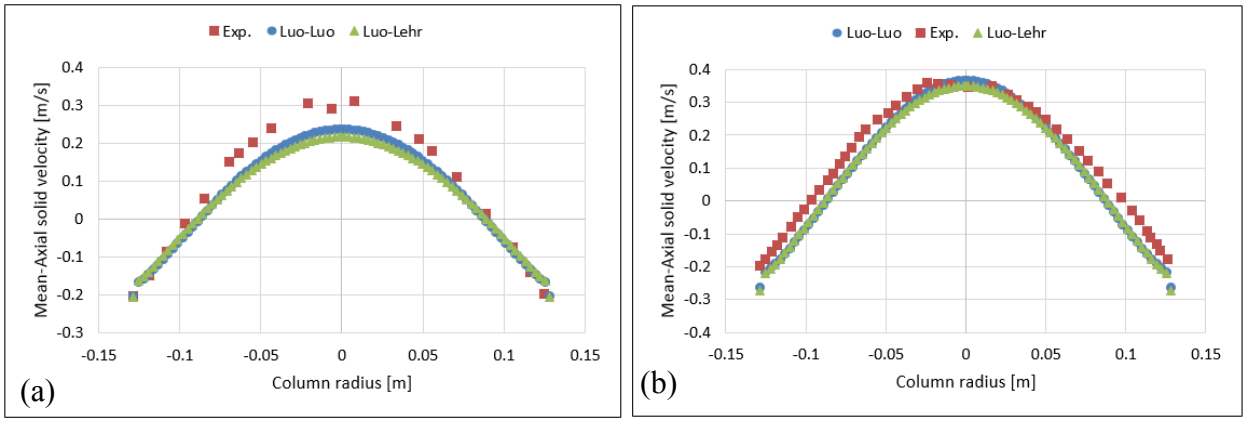

Fig. 5-9. Comparison between the calculated radial profiles of the solid axial velocity when compared to experimental data of Sannaes (1997) using (a) 5 cm/s and 14% solid loading; (b) 8 cm/s and 7% solid loading. The column diameter is 0.26 m

5.4.5 Total Gas Holdup and Predicted Profiles

Table 5-5 shows a comparison of the total gas holdup between experiments and simulations both for the 0.14 m and 0.26 m columns using the superficial gas velocities of 5 cm/s and 8 cm/s with solid loadings of 7% and 14%. The combination of the Luo-Luo models under-estimate the gas holdup (except at the highest Ug in the large column). One of the possible reasons is that the Luo breakup model predicts low breakup rate (Liao & Lucas 2009). The latter promotes the formation of large bubbles and decrease the gas holdup. The combination of the Luo-Lehr models over-estimate the gas holdup. The Lehr model predicts higher breakup rate as compared to the Luo model (Wang et al. 2006), which ultimately reduces the Sauter-mean diameter and increases the gas holdup. The absolute difference of the total gas holdup between the simulations and the empirical values is in the range of 0-3.1% (+/-), which might be acceptable for the large-scale industrial applications. However, precise interactions between phases and the detailed influence of the solid phase on the bubble coalescence and bubble breakup are required. Fig. 5-11., shows the predicted time-averaged radial profiles of the gas holdup in the test cases, that were axially averaged over z/L= 0.5 to 0.8. These profiles also show a similar trend for the higher and lower gas holdup in the Luo-Lehr and Luo-Luo models.

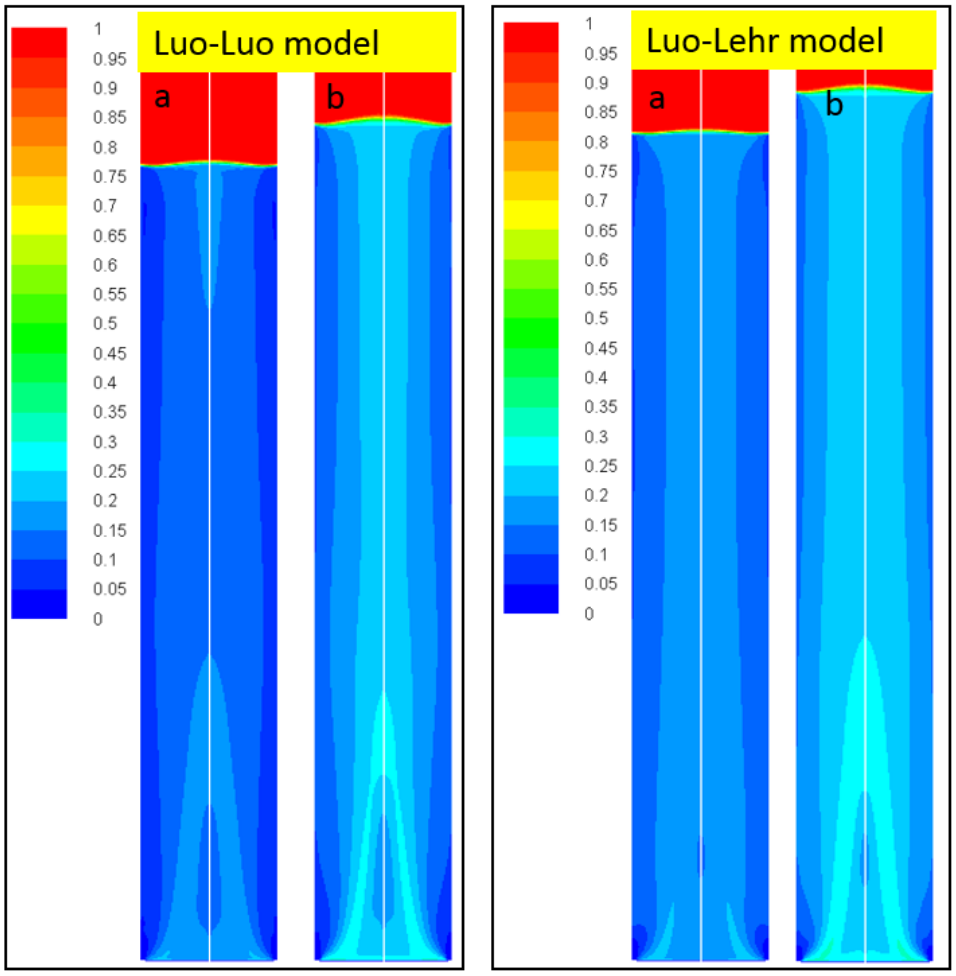

Fig. 5-10. Volume gas fraction simulated with Luo coalescence and Luo breakup models (Luo-Luo) and Luo coalescence and Lehr breakup models (Luo-Lehr) (a) 5 cm/s Ug and 14 % solid loading; (b) 8 cm/s Ug and 7 % solid loading. The diameter of the column is 0.26 m

Table 5-5 Comparison between the calculated and empirical (Sannaes 1997) total gas holdup values using different operation conditions and column diameter

Results	Ug	Loading	Static H	Dynamic H	Gas holdup
	[cm/s]	%	[m]	[m]	[Hd-Hs/Hd] %
Exp. 0.14m	5	14	0.99	1.12 (1.16)	11.60
Luo-Luo	5	14	0.99	1.10	9.75
Luo-Lehr	5	14	0.99	1.14	13.16
Exp. 0.14m	8	7	0.95	1.11 (1.21)	14.40
Luo-Luo	8	7	0.95	1.09	12.84
Luo-Lehr	8	7	0.95	1.13	15.63
Exp. 0.26m	5	14	1.34	1.53	12.40
Luo-Luo	5	14	1.34	1.49	10.07
Luo-Lehr	5	14	1.34	1.55	13.55
Exp. 0.26m	8	7	1.33	1.57	15.30
Luo-Luo	8	7	1.33	1.57	15.29
Luo-Lehr	8	7	1.33	1.63	18.40

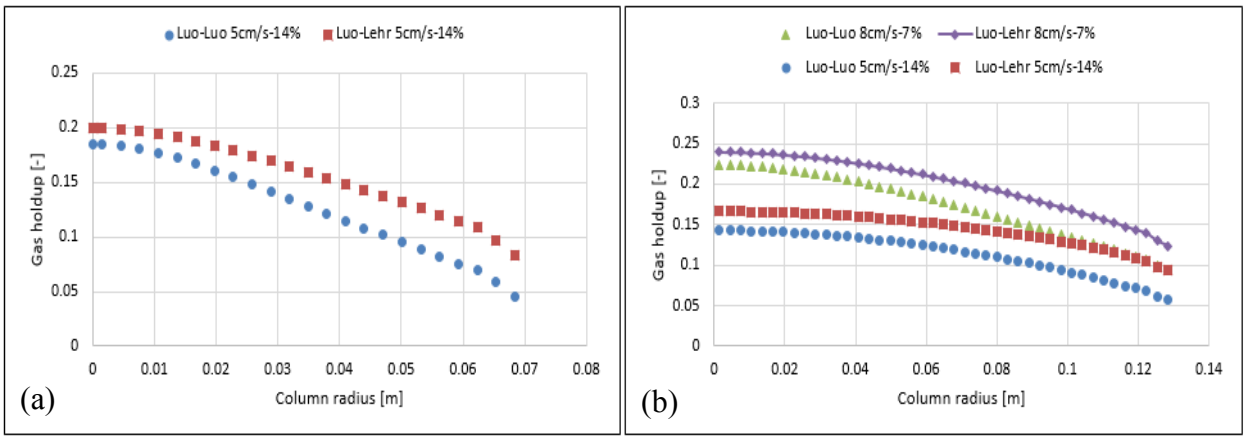

Fig. 5-11. Predicted radial profiles of gas holdup in column diameter of 0.14 m (a) and 0.26 m (b)

5.5 Conclusions

In this work, 2D-axisymmetric simulations of a three-phase bubble column were performed and the simulated time-averaged radial profiles were compared with the empirical data obtained from Sannaes (1997). The investigated superficial gas velocities were 5 cm/s and 8 cm/s for solid loadings of 14% and 7% respectively. Two column diameters were tested: 0.14 m (small) and 0.26 m (large). The developed model consisted of a three-fluid model coupled with a population balance model. The closure for the solid phase included the kinetic theory of granular flows (KTGF) approach in a three-fluid model. Furthermore, the interface momentum transfer consisted of gas-liquid and liquid-solid interactions. The former involves the drag, lift and turbulent dispersion forces. The latter involves the drag and turbulent dispersion forces. The closure for the population balance involves the Luo bubble coalescence model as well as two different bubble breakup models: the Luo and Lehr equations. From this work, the following conclusions were drowned:

A mesh sensitivity analysis was carried out on 3 mm (fine), 4 mm (medium) and 6 mm (coarse) mesh sizes. The first one predicted the axial solid velocity profile closest to the experimental values and therefore, it was selected for the rest of the simulations.

The sensitivity analysis for the discretization of the bubble size distribution was performed using 15, 16 and 17 classes. Results showed that the radial profiles were independent of the number of bubble classes because the Sauter-mean bubble diameter didn't change significantly. However, the highest number of bubble classes (17) cover the largest spectrum of bubbles that were varied from 1 mm to 103 mm hence this value was used for the simulations.

The combination of the Luo coalescence and Luo breakup kernels (Luo-Luo) depicted similar trend of the solid axial velocity with regards to experimental values in both for 0.14 m and 0.26 m diameter columns using 5 cm/s and 8 cm/s superficial velocities and 14% and 7% solid loadings. However, at the highest Ug in the small column, the discrepancy in the results were observed at the core of the column. This might be related to the fact that Luo-Luo models failed to predict the correct position of the fully developed region. The observed bubble size distributions were mono-modal and shifted towards the left-hand side with the increase of gas velocity, which promotes the formation of small bubbles. This behavior is inconsistent with literature data. Results showed that

the total gas holdup was generally under-estimated, which is related to the intrinsic behavior of the Luo's breakup model that predicts a lower breakup rate.

The combination of the Luo's coalescence and Lehr breakup kernels (Luo-Lehr) predicted similar trends for the solid axial velocity when compared to experiments using different column diameters, superficial velocities, and solid loadings. The Luo-Lehr models showed significant discrepancy when using 8 cm/s Ug with a 7% solid loading in the 0.14 m diameter column. This combination also did not predict the fully developed region correctly as compared to empirical values. The predicted bubble size distributions were bi-modal and showed an increase in the formation of large bubbles at elevated Ug. Results showed as well that the total gas holdup was generally over-estimated, which is due to higher breakup rates that decreases the Sauter-mean diameter of bubbles.

6 CFD SIMULATIONS OF AN AIR-WATER BUBBLE COLUMN USING CYLINDRICAL POROUS SPARGER

Abstract

In this work, CFD simulations of an air-water bubbling column were performed and validated with empirical values. Experiments were performed using a cylindrical porous sparger in a transparent glass column (2.1 m height and 0.203 m diameter). The superficial gas velocity was varied from 0.01 m/s to 0.026 m/s, covering the bubbling region only. The population balance model was solved numerically using discrete method and involved the Luo coalescence and Lehr breakup kernels. A Eulerian framework was selected for multi-phase calculations and the interphase momentum transfer included the drag, lift, wall lubrication, and turbulent dispersion terms. The simulated total gas holdup at different superficial velocity showed a similar trend when compared to the experiments. Furthermore, increasing the number of porous spargers affected the dispersion of the bubble plume, however, the gas holdup remained the same as compared to single sparger. The inclusion of a turbulent dispersion term significantly influenced the hydrodynamics of the bubble column as compared to experimental observation. Finally, the influence of the bubble inlet size on the time-averaged radial profiles in the fully developed region was found to be similar.

Keywords: Population balance model (PBM); Single-sized bubble; Bubble size distribution; Bed expansion; Bubble column.

6.1 Introduction

Bubble columns have reportedly been used in the chemical (Deckwer 1992), bioprocesses (Arcuri et al. 1982) and petrochemical (Wender 1996) industries. In a simple bubble column reactors, the gas phase is dispersed into a liquid or a liquid-solid continuous phase. Generally, depending on the superficial velocities and column diameter, the regime inside the bubble column is either bubbly-homogeneous or churn-heterogeneous (Deckwer 1992). In two-phase bubbly flow, bubble size varies due to bubble coalescence and breakup, hence complicating the hydrodynamic behavior inside the system (Liang-Shin & Yang 2003). Therefore, a comprehensive understanding of the fluid dynamics is important for the prediction of mixing, particle settlement, and flow fields in such system.

Computational fluid dynamics (CFD) is commonly used technique to simulate the behavior of bubble column reactors. In CFD, authors have considered constant-sized (Wilkinson 1991), dual-sized (Krishna et al. 1990), and population balance (Wang et al. 2005; Krepper et al. 2008) approaches to predict the hydrodynamics of bubble columns. Krishna et al. (2000) performed both 2D-axisymmetric and 3D simulations using air-water and air-Tellus oil systems. The authors suggested that the bubble size was not constant and involved two sizes (small and larger). Results showed that this assumption (small and large bubbles) was not sufficient enough to correctly predict the gas void fraction. Lucas et al. (2005) performed the experiments in a vertical pipe and measured the bubble size distributions in the homogeneous and heterogeneous regimes. The authors concluded that the bubble size consisted of a spectrum of bubble sizes. This change in bubble size is due to the coalescence and breakup phenomena. A population balance model (PBM) was used to take into account the bubble coalescence and breakup mechanisms and was coupled with a two-fluid model. PBM, in general, discretizes into N-bubble classes hence providing the bubble size distribution directly. A single momentum equation is solved for all bubble classes. However, bubble classes could be divided into multiple sub-velocity groups and the momentum equation can be solved for each subgroup. This approach is called an inhomogeneous multiple-sized group (iMUSIG) model. Krepper et al. (2008) implemented the iMUSIG approach to simulate a gas-liquid bubble column and suggested that two or three sub-velocity groups could be sufficient to capture the hydrodynamics of the column. They concluded that the iMUSIG approach was capable of simulating low to high gas holdup system and showed a similar trend of gas and axial liquid velocity profiles with respect to the experiments. Furthermore, the authors suggested that the discrepancy in the results was limited by bubble coalescence and breakage kernels. Xu et al. (2013) simulated a bubble column using both the homogeneous and inhomogeneous (MUSIG) approaches operated in a churn-turbulent regime. The kernels involved Luo (1993) coalescence and Luo & Svendsen (1996) and the interphase momentum involved both a drag and lift models. The Xu concluded that both the homogeneous MUSIG (with lift force) and the inhomogeneous MUSIG models agreed well with experimental results. Wang et al. (2003 and 2005) studied the influence of different coalescence and breakup kernels and reported that the breakup rate predicted by Lehr et al. (2002) kernel is higher than the other breakup formulations. Moreover, they concluded that the Lehr model has a tendency to predict the large bubble size at elevated superficial velocity.

Tomiyama (1998) developed a lift coefficient that takes into account the bubble size and shape and depends on the Reynolds and modified-Eotvos number. This lift coefficient defines the shape of the radial profiles. The direction of the bubbles changes if the lift coefficient has a positive or negative value. Small bubbles (db <5.8 mm) are known to have a positive lift coefficient and tend to go toward the lowest liquid velocity (i.e. the wall). The larger bubbles (db > 5.8 mm) are associated with a negative value and tend to stay at the core of the bubble column. Zhang et al. (2006) studied the influence of the lift force and concluded that the inclusion of this force improves the dispersion and the shape of the bubble plume. Masood & Delgado (2014) studied the influence of interphase forces and turbulence formulations in the gas-liquid rectangular bubble column. The authors concluded that the Ishii & Zuber (1979) model predicts better flow fields as compared to other empirical formulations. The inclusion of the wall lubrication force increases the vertical liquid velocity at the center since bubbles were pushed towards the center of the column. Furthermore, Renormalization Group (RNG) k-epsilon and RNG k-epsilon (with bubble-induced turbulence) both agreed well with experiments. Wang & Yao (2016) also evaluated the interphase forces and concluded that each model has its limitation related to bubble size, bubble shape, flow regime and operating conditions. Hence, there is no universal model fitting in all the operating conditions. However, the Wang suggested that the inclusion of drag, lift, and wall lubrication forces were necessary to simulate the bubble column. Laborde-Boutet et al. (2009) studied the influence of the k-ε turbulence model using Standard, Renormalization Group (RNG) and Realization formulations. The k-ε model was solved both for the mixture and the liquid phases. The results showed that the RNG k- ε predicts higher dissipation rate as compared to other formulations and was recommended it for the implementation of a population balance model.

In literature, most of the experiments and simulations were performed using inlets such as sintered plate although a few publication (Michele & Hempel 2002) was made in which sparger configuration was considered. In this work, the focus will be put both on the simulations and the experiments using single and multiple porous spargers. The objectives of this paper are given as:

- Study the influence of single and triple porous spargers on the gas holdup and bubble plume
- Study the influence of turbulent dispersion term on the flow fields
- Study the influence of bubble inlet size

The commercial software Ansys-Fluent v.17.2 was used for all CFD simulations using both 2D-axisymmetric and 3D geometries.

6.2 Experiments

The experiments were performed at ambient conditions. The superficial gas velocities (Ug) investigated in this work were of 0.010 m/s, 0.0151 m/s, 0.021 m/s and 0.026 m/s. Gas flow was monitored by a digital flow meter. The static bed height (water level) at rest condition (H_0) was 1.4 m and maintained constant throughout the experiments. The dynamics bed height (H_d) remained linear until a 0.026 m/s value of Ug was reached, corresponding to a homogeneous regime. The total gas holdup is calculated as

$$\alpha_g = \frac{H_d - H_0}{H_d} \tag{6-1}$$

The bubble plume height was observed visually at different velocity. The pressure probes close to the wall were located axially at 0.27 m, 0.58 m, 0.86 m, 1.14 m and 1.41 m and were connected to a high accuracy digital gauge. The test bench included a transparent glass cylinder of 2.1 m height, 0.203 m inner diameter, and 2 mm (+/-1.1 mm) wall thickness. The latter was supplied by Friedrich & Dimmock International. The experiments were performed with a gas inlet consisting of single and triple cylindrical porous spargers. The height, diameter, and pore diameter of the spargers were of 0.1587 m, 0.0254 m and 0.8 μm respectively. The sparger top (see Fig. 6-1) was an opaque stainless steel plate supplied by the Pall Corporation. The experimental setup of the single and triple spargers are shown in Fig. 6-1 and Fig. 6-2 respectively. Each sparger was placed at an angle of 120^0. The distance between the spargers and the glass cylinder centroids was of 0.1016 m.

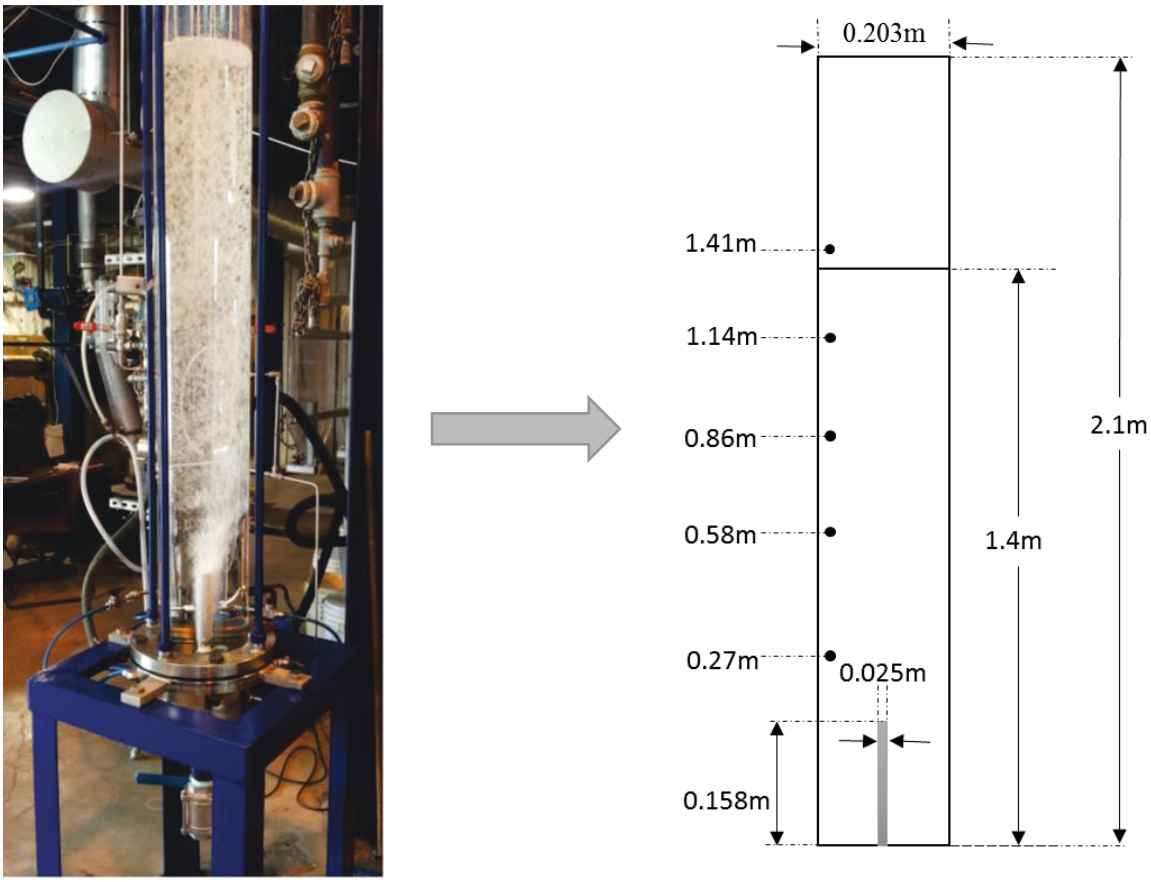

Fig. 6-1. Refers to the setup used with a single sparger

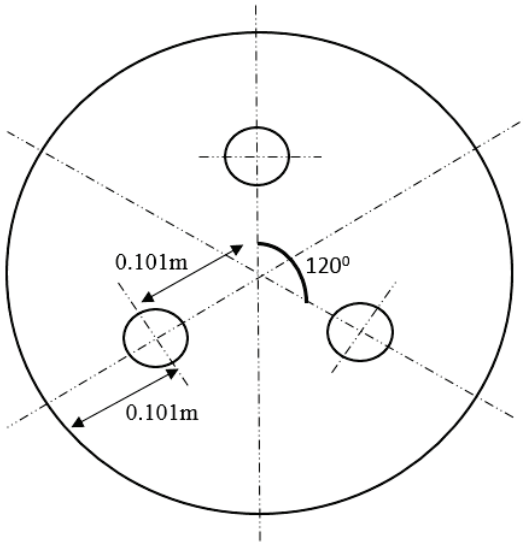

Fig. 6-2. Top view of three sparger geometry setup

6.3 Model & Numerical Setup

The gas-liquid bubbly column was simulated using a two-fluid model, where the gas phase was treated as a dispersed phase and liquid as a continuous phase. The continuity and the momentum equations were solved for each phase. The interphase momentum transfer involved a drag (Ishii & Zuber 1979), lift (Tomiyama 1998), wall lubrication (Antal et al. 1991) and turbulent dispersion (Simonin & Viollet 1990) terms. The Ishii drag coefficient takes into account the shape of the bubble and covers a wide range of superficial velocity. The Tomiyama lift coefficient accounts for the lateral movement of the bubbles and depending on its sign, the direction of the bubbles changes. The Antal wall lubrication coefficient is a lift force, which is applied near the vicinity of the wall pushing bubbles away from it. The Simonin model disperses the bubbles from the highest to the lowest concentration region and is a function of turbulent viscosity. The population balance model (PBM) was used for the gas phase and was discretized using a bubble class method. The kernels included Luo (1993) coalescence and Lehr et al. (2002) breakup models. All the model equations are mentioned in Table 6-1.

Simulations for single and triple spargers were performed using both 2D-axisymmetric and 3D geometries. The assumption of 2D axisymmetric could be reasonable since experimental data reported by Hills (1974) and Degaleesan (1997) showed that the time-averaged flow fields produce a stationary axisymmetric pattern, hence supporting the validity of the 2D model. The 3D-geometry involves 1/6 domain (see Fig. 6-3), assuming that the flow pattern was pseudo-steady. The number of cells in the 2D and 3D geometries were of 23962 and 116451, respectively. The number of bubble classes in PBM involved 14 bins ranging from 1.1 mm to 28.0 mm. The simulations were run with a parallel solver using clusters of up to 40 cores. Fixed time steps (10^{-4} and 10^{-3} sec) were used and guaranteed that the Courant number for air and water velocities <1. The simulations converged well and a pseudo-steady state was achieved (flow patterns were stabilized). The simulations were run for 50s flow time. A time-averaged sampling was calculated after the 30s.

Table 6-1 Model equations

Continuity equation

$$\frac{\partial(\alpha_q\rho_q)}{\partial t} + \nabla.\left(\alpha_q\rho_q\boldsymbol{u}_q\right) = 0$$

Momentum equation

$$\frac{\partial(\boldsymbol{u}_q\rho_q\alpha_q)}{\partial t} + \nabla.\left(\alpha_q\rho_q\boldsymbol{u}_q\boldsymbol{u}_q - \mu_q\alpha_q(\nabla\boldsymbol{u}_q + (\nabla\boldsymbol{u}_q)^T)\right) = -\alpha_q.\nabla p + \boldsymbol{F}_{pq} + \alpha_q\rho_q\boldsymbol{g}$$

Drag forces

$$\boldsymbol{F}_{D,pq} = -\frac{3}{4}\alpha_p\alpha_q\rho_q\frac{C_D}{d_p}|\boldsymbol{u}_p - \boldsymbol{u}_q|(\boldsymbol{u}_p - \boldsymbol{u}_q)$$

For viscous regime $[C_{D,dis} < C_{D,vis}]$,

$$C_{D,vis} = \frac{24}{Re}(1 + 0.1Re^{0.75})$$

For distorted regime $[C_{D,vis} < C_{D,dis} < C_{D,cap}]$,

$$C_{D,dis} = \frac{2}{3}d_p\sqrt{\frac{g\Delta\rho}{\sigma}}\left(\frac{1 + 17.67f^{*\frac{6}{7}}}{18.67f^*}\right), \qquad f^* = (1-\alpha_p)^{1.5}$$

For capped regime $[C_{D,dis} > C_{D,cap}]$,

$$C_{D,cap} = \frac{8}{3}(1-\alpha_p)^2$$

Lift force

$$\boldsymbol{F}_L = -C_L\alpha_p\rho_q(\boldsymbol{u}_p - \boldsymbol{u}_q)(\boldsymbol{\nabla}\boldsymbol{u}_q)$$

$$C_L = \begin{cases} \min\left[0.288\tanh\left(0.121Re, f(Eo')\right)\right], for\ Eo \le 4 \\ f(Eo'), \qquad for\ 4 \le Eo' \le 10 \\ -0.27 \qquad for\ 10 \le Eo' \end{cases}$$

Turbulent dispersion force

$$\boldsymbol{F}_{td,q} = -\boldsymbol{F}_{td,p} = C_{TD}K_{pq}\frac{D_{t,pq}}{\sigma_{pq}}\left(\frac{\nabla\alpha_p}{\alpha_p} - \frac{\nabla\alpha_q}{\nabla\alpha_q}\right)$$

The mixture RNG k-epsilon

$$\frac{\partial(\rho_m k)}{\partial t} + \nabla.(\rho_m\boldsymbol{u}_m k) = \nabla.\left(\left(\mu_m + \frac{\mu_{t,m}}{\sigma_k}\right)\nabla k\right) + G_{k,m} - \rho_m\varepsilon$$

$$\frac{\partial(\rho_m\varepsilon)}{\partial t} + \nabla.(\rho_m\boldsymbol{u}_m\varepsilon) = \nabla.\left(\left(\mu_m + \frac{\mu_{t,m}}{\sigma_\varepsilon}\right)\nabla\varepsilon\right) + \frac{\varepsilon}{k}\left(C_{1\varepsilon}G_{\varepsilon,m} - C_{2\varepsilon}\rho_m\varepsilon\right)$$

Population balance model

$$\frac{\partial}{\partial t}n_i + \nabla.(\boldsymbol{u}_i n_i) = \sum_{d_j=d_i}^{d_{max}}\Omega_B(d_j:d_i) - \Omega_B(d_i) + \sum_{d_j=d_{min}}^{d_i/_2}\Omega_C(d_j:d_i - d_j) - \sum_{d_j=d_{min}}^{d_{max}-d_i}\Omega_C(d_j:d_i)$$

Gas volume fraction

$$\alpha_g = \sum_{i=1}^{N} n_i\frac{\pi}{6}d_i^3$$

Luo coalescence kernel

$$\Omega_C(d_i:d_j) = c_0(d_i + d_j)^2\left({d_i}^{2/3} + {d_j}^{2/3}\right)^{1/2}\varepsilon^{1/3}n_i n_j\ exp\left\{-\frac{t_c}{t_l}\right\}$$

Lehr breakup kernel

$$\Omega_B(d_i:d_j) = \frac{1.19\sigma}{\rho_l\varepsilon^{1/3}d_i^{7/3}f^{1/3}}\int_{\xi_{min}}^{1}\frac{(1+\xi)^2}{\xi^{\frac{13}{3}}}exp\left(\frac{2\sigma We_{crit}}{\rho_l\varepsilon^{2/3}d_i^{5/3}f^{1/3}}\xi^{-2/3}\right)d\xi$$

$$\Omega_B(d_i) = \int_0^1\Omega_B(d_i:d_j)df$$

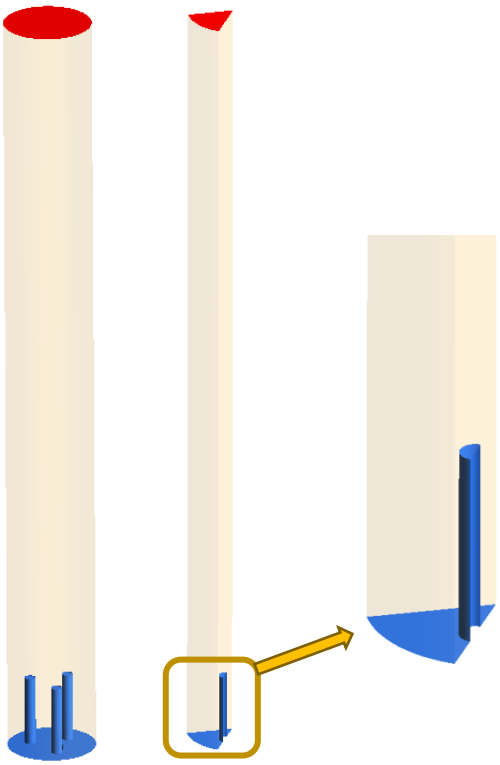

Fig. 6-3 Left complete (transformed) 3D geometry, center actual simulated domain and right zoomed nozzle domain

6.4 Results and Discussions

6.4.1 Experiments Result

The total gas holdup values for single and triple spargers were measured at different superficial gas velocity (U_g), varying from 0.01 m/s to 0.026 m/s (as shown in Fig. 6-4). The total gas holdup values for both single and triple spargers were almost similar. The total gas holdup increases linearly while the system is in the homogeneous regime and the bed top is uniform. At an U_g value of above 0.026 m/s, the transient (churn) regime was observed but, since this was not the purpose of this research, this element will not be discussed. Fig. 6-5 shows the bubble plumes for a single sparger at different velocity. As the Ug increases, the bubble plume height decreases. However, this decrease in plume height was not significant and hard to quantify it with visual observation. Therefore, an average height of bubble plumes is considered that is 0.3 m single sparger, after which both phases were well homogenized. Fig. 6-6 shows that the averaged-bubble plume height in the triple spargers decreases to 0.16 m. The behavior might be related to velocity magnitude. The higher the number of spargers, the lower the velocity magnitude at each sparger and ultimately

the lower the bubble plume height. Fig. 6-7 shows the time-averaged gradient of axial pressure measured at five positions operated at different U_g pressure drops remained unchanged at all operating velocities.

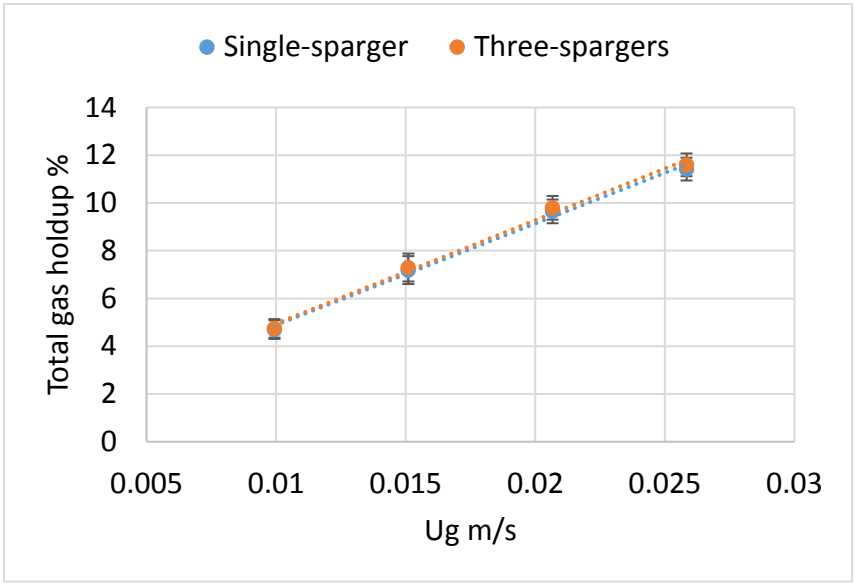

Fig. 6-4 Measured total gas holdup at different superficial gas velocity

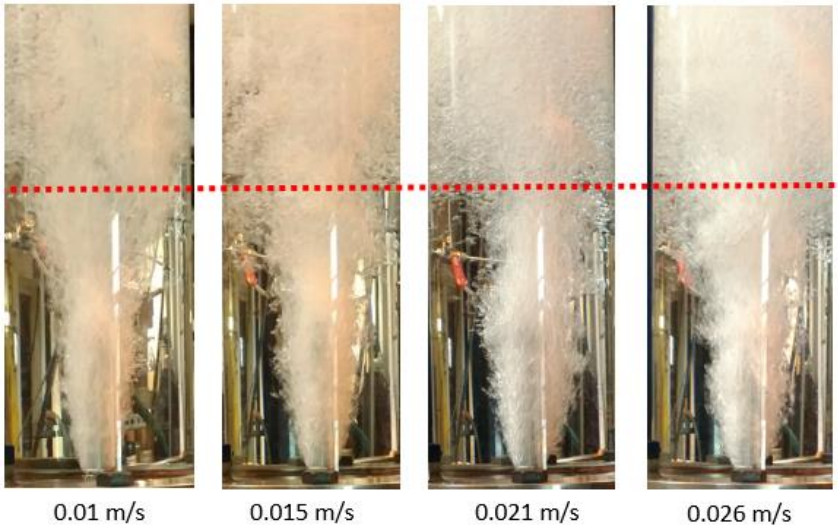

Fig. 6-5 Bubble plume near cylindrical porous sparger, with averaged plume height of 0.3 m (red dotted line)

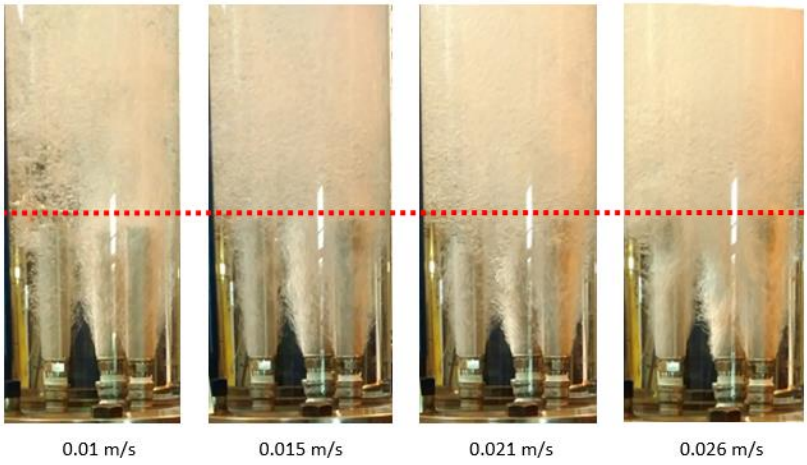

Fig. 6-6 Bubble plume near cylindrical porous sparger, with averaged plume height of 0.16 m (red dotted line)

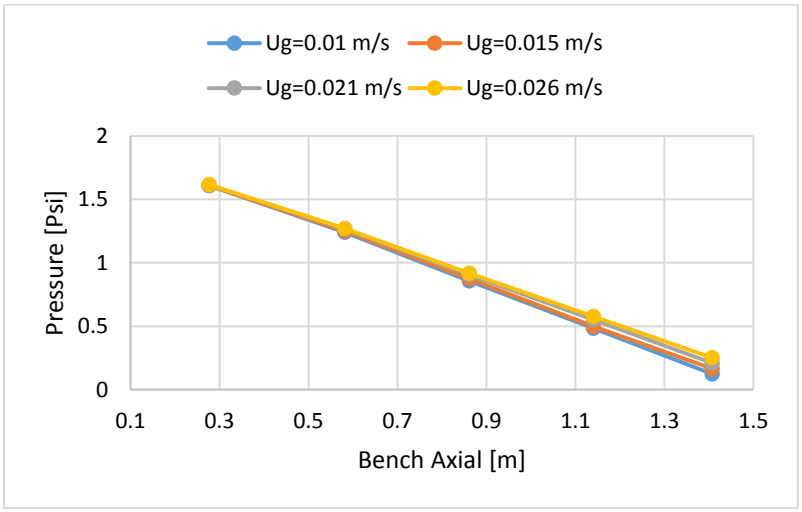

Fig. 6-7 The time-averaged axial pressure drop along the column height

6.4.2 Effect of Inlet Bubble Diameter

The bubble inlet size was calculated from Koide et al. (1968) correlation, which depends on the liquid properties and sparger geometry. The correlation is given as:

$$\bar{d}\left(\frac{g\rho_q}{\delta\sigma}\right)^{1/3} = 1.65\left(\frac{Fr}{We^{0.5}}\right)^{0.160} \tag{6-2}$$

Where $\bar{d}, g, \rho_q, \delta, \sigma, Fr\ and\ We$ are average bubble size, gravitational acceleration, density of the liquid, average pore size, surface tension, and dimensionless numbers (Froude and Weber) respectively. The latter are calculated as

$$Fr = \frac{u_g^2}{\epsilon^2 g\delta} \tag{6-3}$$

$$We = \frac{u_g^2 \delta \rho_q}{\epsilon^2 \sigma} \tag{6-4}$$

Here ϵ is the porosity of the porous plate.

The calculated bubble inlet size at different superficial velocity was in the range of 1.9 mm to 2.1 mm. It is computationally expensive to provide the bubble class of such a small interval. Therefore, the influence of bubble inlet size was tested using 1.6 mm and 2.1 mm bubble sizes at a superficial velocity of 0.015 m/s, as it is shown in Fig. 6-8. The predicted time-averaged radial profiles of gas hold and axial liquid velocity using bubble inlet sizes of 1.6 mm and 2.1 mm are similar to each other. Since no difference is found in the radial profiles, the rest of the simulations were performed using a constant bubble inlet size of 2.1 mm.

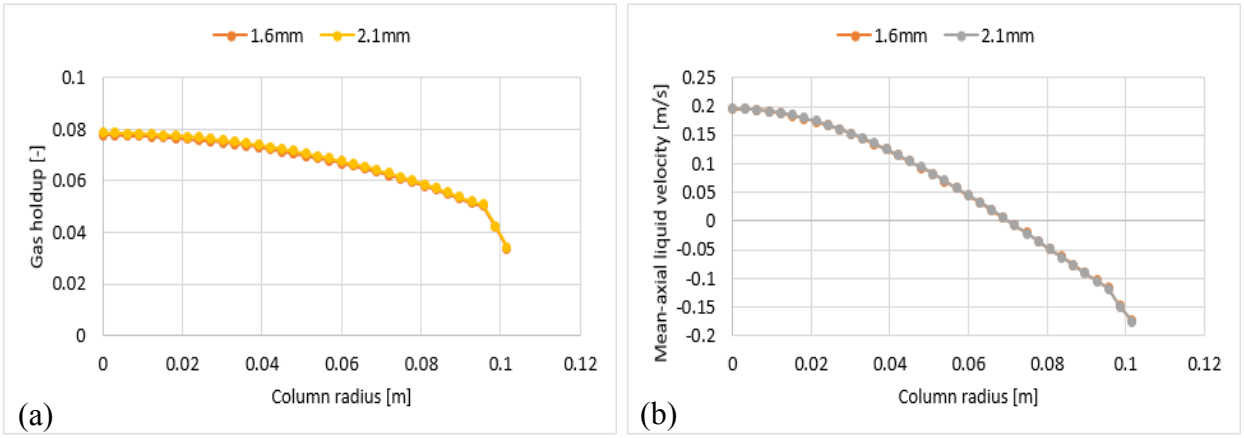

Fig. 6-8. Predicted radial profile of gas holdup (a) and axial liquid velocity (b) using bubble inlet sizes of 1.6 mm and 2.1 mm, plotted at 1.2 m height

6.4.3 Effects of the Turbulent Dispersion Force

The ensemble averaging of the instantaneous interface drag force gives mean drag and the fluctuating component of drag force. The latter component is known as turbulent dispersion force. This force accounts for the interaction between turbulent eddies and disperses phase (bubbles) and transports the disperse phase from the most to the least concentrated regions. Turbulent dispersion force is a function of phase gradients, interphase momentum transfer coefficient, and turbulent kinematic viscosity. The latter viscosity is calculated from the k-epsilon turbulent model. In literature (to our best knowledge), the importance of the dispersion term is not well highlighted

and only publications were made (Lucas et al. 2007; Yamoah et al. 2015; Wang & Yao 2016), in which authors reported that the inclusion of turbulent dispersion improves the radial profiles of gas holdup and liquid velocity. The authors didn't report the significant influence of this term on the hydrodynamics of the bubble column. One of the reasons is that their experiments were performed with flat porous/ perforated plate as a gas inlet, where the cross-sectional area of gas inlet equals to column diameter, hence the bubbles were well dispersed prior to entering the system. In this study, the results show that the influence of the turbulent dispersion term on the hydrodynamics of the bubble column using single porous sparger is very significant, as it is seen in Fig. 6-9. Without the turbulent dispersion term, bubbles tend to accumulate at the core of the column and form a pseudo-slug flow. As the U_g increases, slug behavior dominates the system. This fluid behavior is non-realistic and far from experimental fluid dynamics results. However, when the turbulent dispersion term is included, the bubbles are well dispersed across the column and show similar trend as compared to experiments. Based on simulations, it is observed that results are dependent on the turbulent dispersion force. Hence, in the case of a porous vertical sparger, it is highly recommended to include the turbulent dispersion term for interphase momentum transfer. However, further investigation and validation related with different turbulent dispersion models will be required in the near future.

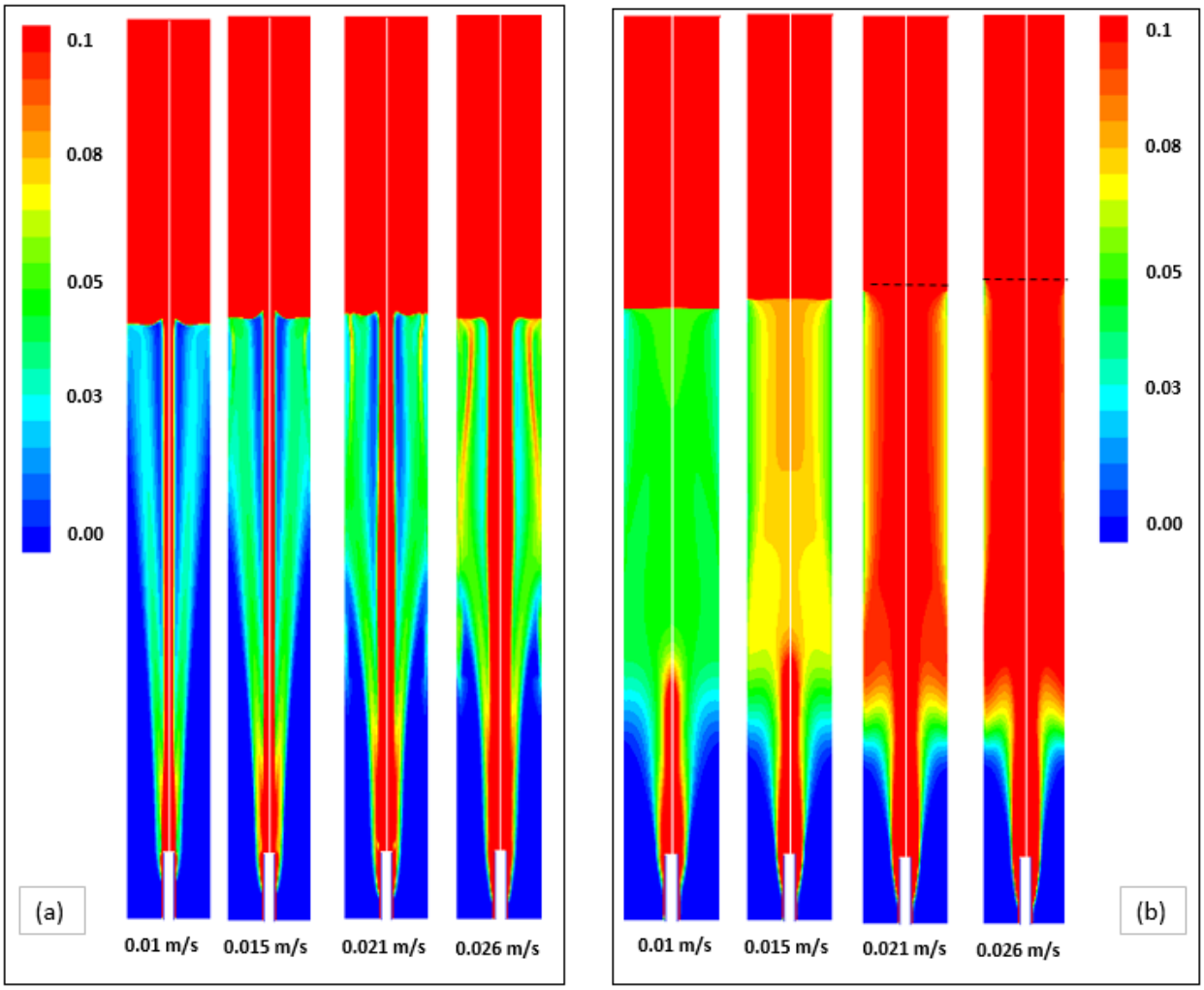

Fig. 6-9. Contours of volume gas fraction, (a) without the inclusion of the turbulent dispersion term and (b) with the inclusion of the turbulent dispersion term

6.4.4 Simulations with a Single Nozzle

Fig. 6-10 shows the comparison of the predicted total gas holdup with the empirical data at different superficial velocity (Ug) varied from 0.01 m/s to 0.026 m/s. At the lowest Ug, the predicted total gas holdup is close to experimental data with a difference of 1.4%. The discrepancy between simulations and experiments increases with increase in Ug, which might be related to isotropic nature of turbulence, the formation of population and inlet configuration. The k-epsilon turbulence model is isotropic but the actual system is anisotropic (Fraga et al. 2016), therefore the large size eddies present in the column could not be captured. The bubble coalescence and bubble breakup rates depend only on turbulence parameter and ignore viscous and wake effect (Xu et al. 2013). This assumption might influence the formation of bubble and predicts larger bubbles, which eventually increase the bubble rise velocity and decrease the gas holdup. The inlet configuration

might have imposed chaotic flow fields due to the formation of very large bubbles (Michele & Hempel 2002), making the flow unstable. The trend of predicted and experimental gas holdup is promising. Fig. 6-11 shows the time-averaged bubble plumes simulated at different superficial velocity. The predicted bubble plume heights were measured by plotting the gas fraction concentration along the wall and selecting the lowest fraction. The bubble plume heights were 0.4 m, 0.38 m, 0.371 and 0.362 m at 0.01 m/s, 0.015 m/s, 0.021 m/s and 0.026 m/s superficial velocities respectively. The bubble plume height decreases with increase in Ug. One of the possible reasons for such behavior is with an increase in Ug, the liquid backflow velocity increases too, which pushes the small bubbles (db<5.8mm) present near the wall downward. The predicted and measured averaged plume heights at different Ug were 0.37 m and 0.3 m, respectively.

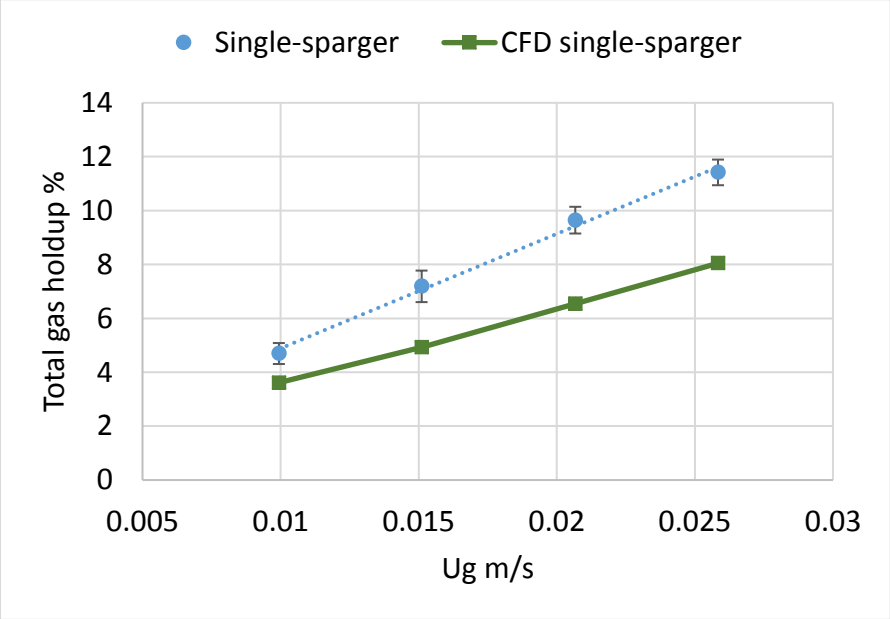

Fig. 6-10. Comparison of predicted total gas with experimental value using single sparger at different superficial velocity

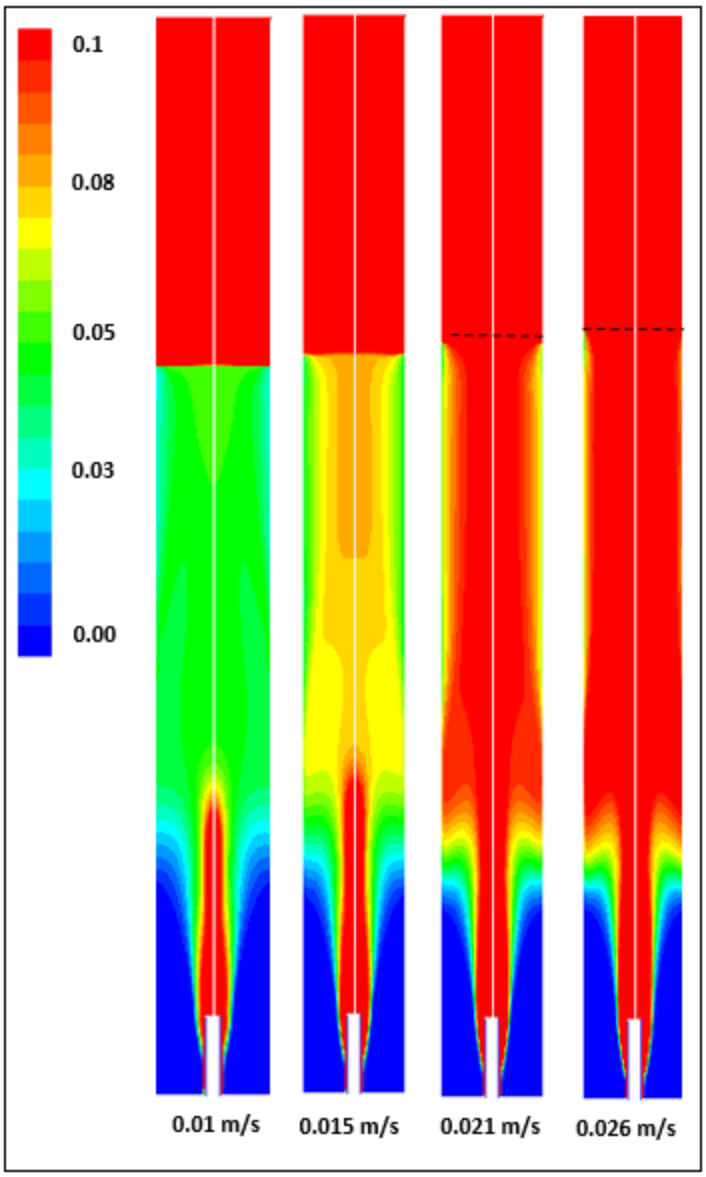

Fig. 6-11. Contour of the gas fractions in a single sparger geometry at different superficial velocity

Fig. 6-12 shows the predicted time-averaged gas holdup profiles plotted at different column height using different superficial velocity. The peak at 0.6 m shows that the flow is under-developed ($dy/dx \neq 0$). This peak is disappeared with the column height and after 1 m and onwards the flow is fully developed ($dy/dx=0$) except at 0.01 m/s. In order to validate this behavior, the experiments might be performed in the near future to measure the local profiles of gas holdup and axial liquid velocity. Fig. 6-13 shows the mean axial velocity of the water plotted at 1.2 m height. The liquid velocity increases with the superficial gas velocity. The predicted maximum value of axial liquid

velocity at the center of the column (r=0) is 0.13 m/s, 0.19 m/s, 0.21 m/s and 0.24 m/s at 0.01 m/s, 0.015 m/s, 0.021 m/s and 0.026 m/s Ug respectively.

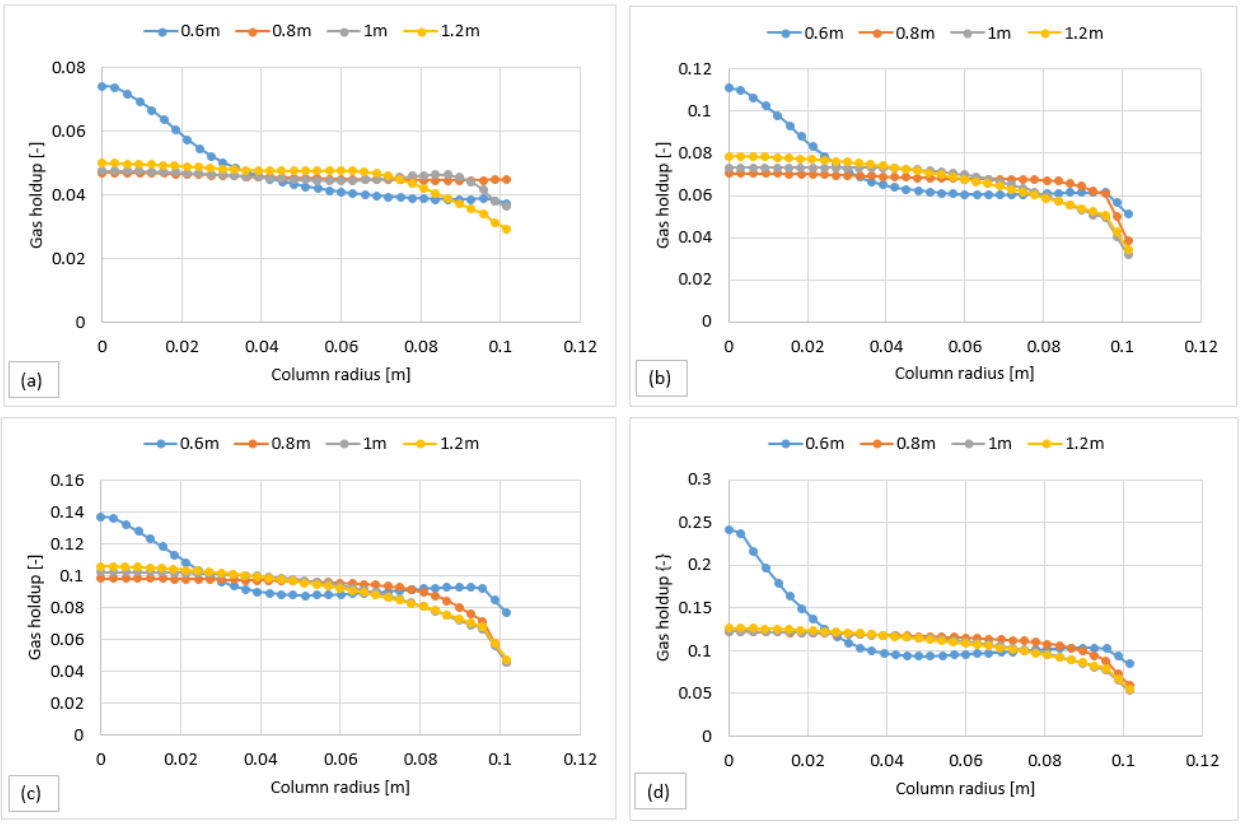

Fig. 6-12. Predicted time-averaged gas holdup profiles at different column height using superficial velocities of 0.01 m/s (a) 0.015 m/s (b) 0.021 m/s (c) and 0.026 m/s (d)

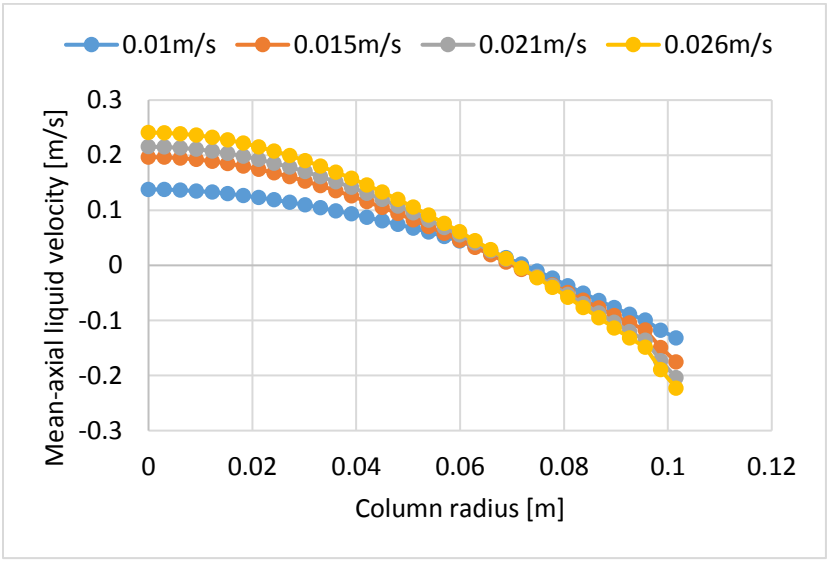

Fig. 6-13. The time-averaged radial profile of axial liquid velocity obtained using different superficial velocity and plotted at 1.2 m height

6.4.5 Effect of Number of Spargers

3D simulations were performed on the triple configurations in order to further validate the developed model and observe the fluid dynamics behavior. As discussed earlier, the simulated 3D geometry involves 1/6 domain (see Fig. 6-3), assuming that the flow pattern was pseudo-steady. 1/6 domain was transformed into complete geometry for better graphical representation purpose. Fig. 6-14 shows the comparison of the total gas holdup between single and triple spargers with the empirical values. Simulated gas holdup values in both single and triple setups were similar as expected since mass flow rates were identical. However, a slight improvement in a gas holdup is seen with triple spargers, which might be related to 3D-geometry. Fig. 6-15 shows the time-averaged height of the bubble plume in triple spargers configuration, which was lowered down due to lower velocity magnitude. The predicted bubble plume heights were 0.25 m, 0.24 m, 0.22 and 0.2 m at 0.01 m/s, 0.015 m/s, 0.021 m/s and 0.026 m/s superficial velocity respectively. The averaged plume height at different Ug in triple spargers was 0.22 m, which was close to experimental value (0.16 m). The bubble plume gave useful information related with fluid dynamics behavior in single and triple configurations. The triple spargers confirmed the reliability of the model and supported this work.

Fig. 6-16 shows the predicted time and radial averaged gas holdup profiles in triple spargers at different column height using different superficial gas velocity. The gas flow fields along the column were steadier than the single sparger and no peak was found at 0.6 m height. One of the possible reasons for this behavior is that the bubbles were well distributed in triple spargers due to high surface area of the inlets as compared to single sparger. The fully developed regime was found at 1 m and onwards (except Ug=0.01 m/s), which was similar to single sparger. Fig. 6-17, shows the time and radial averaged axial velocity of the water plotted at 1.2 m height. The predicted maximum values of axial liquid velocity at the center of the column (r=0) were 0.15 m/s, 0.17 m/s, 0.22 m/s and 0.23 m/s at 0.01 m/s, 0.015 m/s, 0.021 m/s and 0.026 m/s Ug respectively. These maximum values of velocity were almost identical to single sparger. Results show no significant influence of the inlet configurations in the fully developed region. However, the increasing number of spargers significantly affect the bubble plume height and dispersion of the bubbles at the bottom of the column.

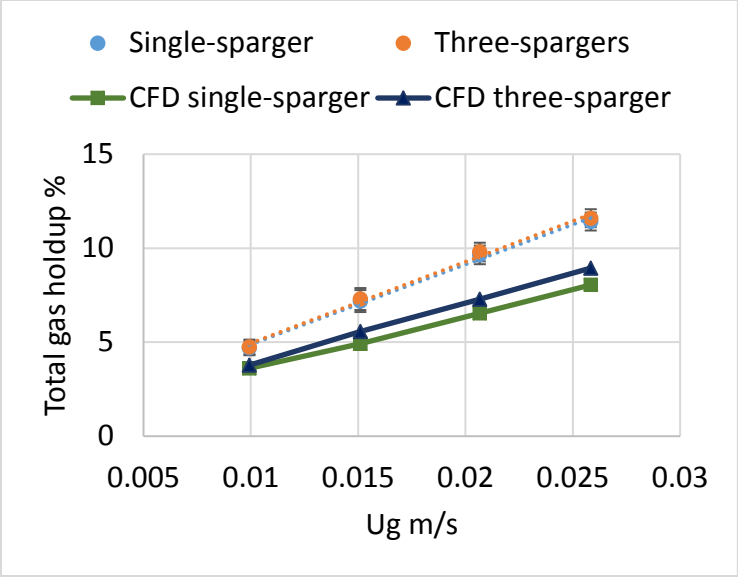

Fig. 6-14 Validation of CFD model in single and triple configurations with experimental values of gas holdup

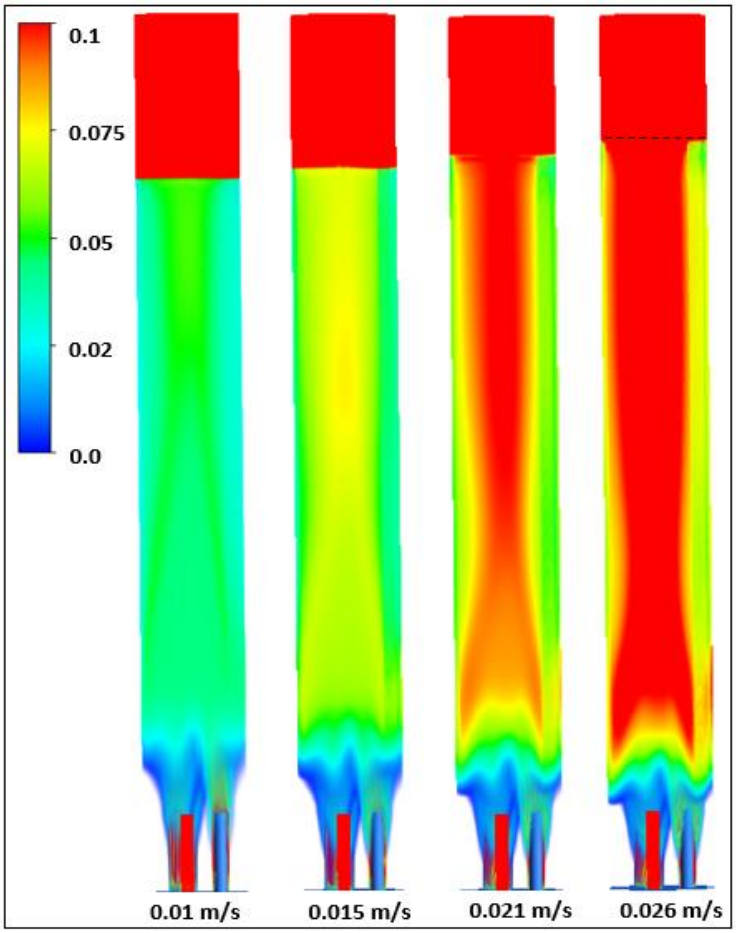

Fig. 6-15 Contours of the volume gas fraction simulated for the triple spargers at different superficial gas velocity.

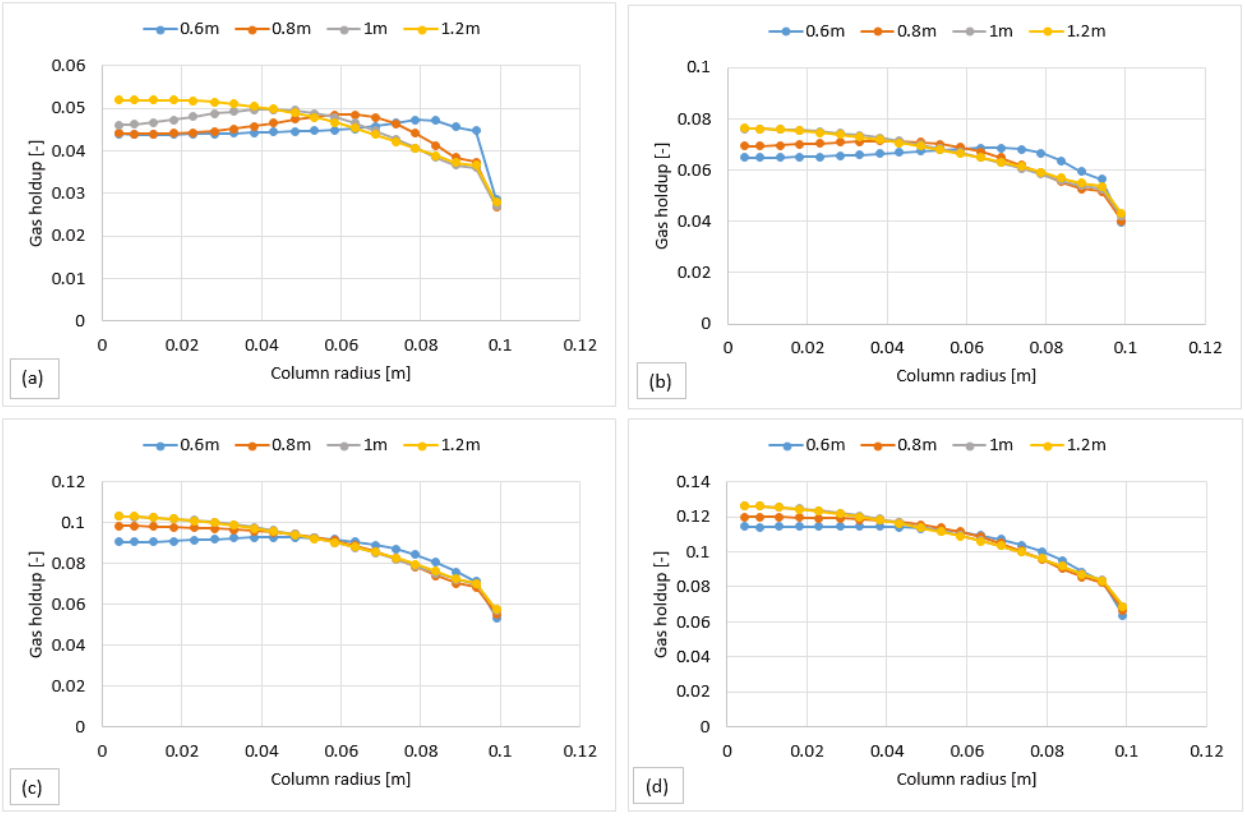

Fig. 6-16. Predicted time and radial averaged gas holdup profiles in triple spargers at different column height using superficial velocity of 0.01 m/s (a) 0.015 m/s (b) 0.021 m/s (c) and 0.026 m/s (d)

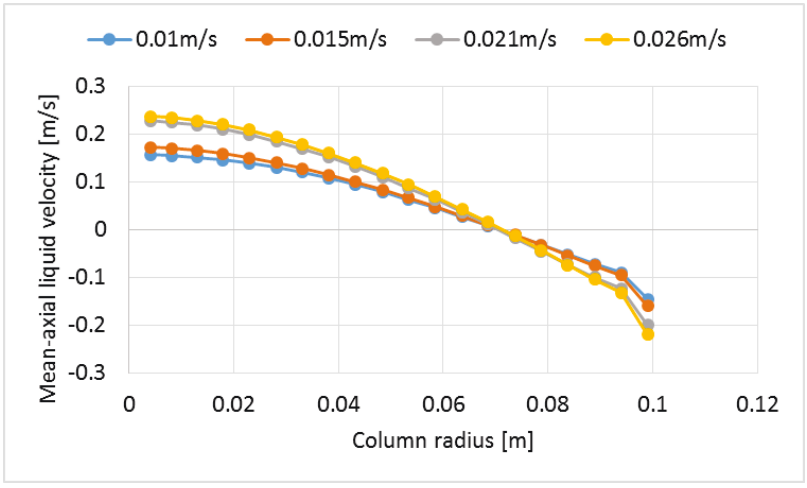

Fig. 6-17. Time and averaged radial profile of the axial liquid velocity in triple spargers using different superficial velocity plotted at 1.2 m height

6.5 Conclusions

In this work, empirical values were compared to CFD-simulations using single and triple spargers. The experiments were performed using air and liquid phases. Superficial gas velocity varied in a range between 0.01 m/s and 0.026 m/s. The developed model consisted of the two-fluid model coupled with population balance model, which was discretized using the bubble class method. The kernels involved Luo coalescence and Lehr breakup. RNG k-epsilon turbulent model was solved for the mixture phase. The interphase consisted of drag, lift, wall lubrication, and turbulent dispersion forces. From this work, the following conclusions could hence be formulated:

- The measured total gas holdup values both in the single and triple spargers were similar. The averaged-pressure drop values along the column height were found insensitive to superficial velocity. The averaged-plume height in single sparger was higher than the triple spargers (0.3 m and 0.16 m).
- The influence of the bubble inlet size was tested using 1.6 mm and 2.1 mm bubble size at 0.015 m/s Ug. Results showed no difference in the time-averaged radial profiles of axial liquid velocity and gas holdup.
- The Influence of the turbulent dispersion term was studied in different superficial velocity and the results showed that without the inclusion of turbulent dispersion term, the hydrodynamic behavior of the bubble column was far away from the experimental observations. The inclusion of turbulent dispersion term was found significantly important.
- The predicted time-averaged total gas holdup in single and triple spargers showed similar trends with the experiments. The predicted averaged bubble plume heights in the single and triple spargers were 0.37 and 0.22 m.
- The fully developed region in the single and triple spargers was found at 1 m height and onwards (except Ug=0.01 m/s). A peak in the gas holdup profile was found at 0.6 m height in the single sparger, which disappeared along with the column height. However, in the triple spargers, no such behavior (peak) was seen. The maximum values of axial liquid velocity at the core of the column (r=0) were similar both in the single and triple spargers.

7 GENERAL CONCLUSIONS AND FUTURE WORK

In this work, CFD simulations were performed in two- and three-phase bubble columns, hence covering both homogeneous and heterogeneous regimes. In addition, results were validated with published data and using a bench-scale system. The disperse phases included gas and glass beads, whereas the continuous phase involved water. A two- and three-fluid Eulerian approach was adopted solving momentum equation for each phase often what the model was coupled with a population balance model (PBM). The latter consists of different bubbles breakup and coalescence kernels which allow predicting an averaged bubble size locally, which later goes into drag formulation to calculate the interphase momentum transfer between phases. This interphase also included the lift, wall lubrication, and turbulent dispersion terms. The solid stress was calculated from the Kinetic Theory of Granular Flows (KTGF) to predict the solid viscosity and the solid-added pressure locally. The following key conclusions were drawn from this work:

- Results showed that the time-averaged radial profiles of the gas holdup, axial liquid velocity, solid axial velocity and the total gas holdup using 2D-axisymmetric geometry predict trend that are similar to experimental results. However, at a higher superficial velocity, the discrepancy between the CFD simulations and experiments were observed.
- In the two-phase flow, it was shown that the coalescence parameter (scaling factor) in the Luo coalescence kernel needed to be reduced in combination with the Luo breakup kernel to improve the gas holdup with regard to the empirical values. This modification of the coalescence parameter was done by user-defined functions and implemented into the Ansys-Fluent software environment. The combination of the Luo coalescence and Lehr breakup (Luo-Lehr) kernels required no such modification. Furthermore, the combination of Luo coalescence and Luo breakup (Luo-Luo) kernels under-predicted the gas holdup as compared to the Luo-Lehr kernels with regards to the empirical data.
- In the three-phase flow, both combinations (Luo-Luo and Luo-Lehr kernels) predict similar time-averaged axial solid velocity with regards to experimental values. However, the former combination often under-predicts the gas holdup as compared to the Luo-Lehr kernels. This behavior of the gas holdup in the three-phase system is similar to the two-phase system. Both

combinations (Luo-Luo and Luo-Lehr kernels) predict the correct trend of fully developed in the large column (0.26 m) when compared to empirical data. However, in the small column (0.14 m), the discrepancy was observed in the fully developed region at elevated superficial velocity and solid loading with regards to empirical data.

- Bench results showed that without the inclusion of a turbulent dispersion term, the hydrodynamic behavior of the bubble column is far from experimental observations. The inclusion of turbulent dispersion term is found significantly important in case of a single tubular sparger.

The discrepancy between CFD-simulations and experiments might be related to following possible reasons:

- The $k-\varepsilon$ turbulence model is isotropic in nature, however, the actual/real system is generally chaotic and anisotropic. This model was originally developed from the liquid phase experiments. The influence of the disperse phase on the turbulence model is later introduced by the correlation, which is still in the developing stage and there is no clear cut model that correctly accounts this additional turbulence induced by bubbles/particles. Furthermore, the $k-\varepsilon$ turbulence model considers that the energy dissipation rate is a function of only small-sized eddies and ignores the influence of large eddies, hence the dissipation rate is under-predicted. This lower value of energy dissipation rate affects both the coalescence and breakup kernels.

- The collision frequency $\omega_C(d_i: d_j)$ of the bubble coalescence kernel, see equation 2-64, and eddy-bubble collision $\omega_B(d_i: d_j)$ of bubble breakup kernel, see equation 2-75, are directly proportional to the energy dissipation rate. If the energy dissipation rate is under-predicted, the bubble coalescence rate increases and bubble breakup rate decreases, promoting the formation of large bubbles in the system. Furthermore, the proposed coalescence and breakup kernels are function of the turbulence parameter only and ignore the viscous shear, interfacial stability and shear-off phenomena, which might influence bubble formation. Lastly, these kernels were developed using experimental observations of two-phase flow and the influence of the solid particle was ignored.

- The physics of the interphase momentum transfer is not well developed in the two- and three-phase system. The hydrostatic pressure decreases along the column height, which increases the volume of the rising bubble. This behavior is ignored in all the previously discussed drag coefficients. Generally, the influence of the pressure on the rising bubbles is a parameter fitted with experiments, using a try-and-error approach. All the previously discussed solid-liquid drag coefficients were developed either from the gas-liquid or the gas-solid system and none was derived from an actual slurry system. The shape of the radial profiles are influenced by the turbulent dispersion term and depend on the turbulent viscosity, which is calculated from the $k - \varepsilon$ turbulence model.

In the light of these observations, any future work could include that:

- The developed model must be tested using the large-eddy simulation (LES) approach in the 3D geometry, along with the robust and well-validated bubble-induced turbulence.
- A new bubble coalescence and breakup kernels are required, which should be developed from the three-phase experimental data that is operated in the heterogeneous regime.
- A unified drag coefficient for gas-liquid and liquid-solid interactions are required, which have to be tested in a wide range operating conditions and geometries and must be validated with experiments. Generally, in literature, these drag coefficients are often tuned and validated with the empirical values using a narrow range of superficial velocity.
- Kinetic parameters as well as heat/mass transfer are needed to be implemented in this developed model and must be validated with the empirical values.
- An attempt to simulate the Enerkem industrial and pilot scale bubble reactors are required to test if the developed model could predict correct trend of the time-averaged radial profiles with the industrial-scale data.

CONCLUSIONS GÉNÉRALES ET TRAVAUX FUTURS

Dans ce travail de recherche, des simulations CFD ont été réalisées sur des systèmes bi et tri-phasique dans des colonnes à bulles couvrant les régimes homogènes et hétérogènes et validés avec des données publiées dans la littérature ainsi qu'obtenu d'un banc d'essai. Les phases dispersées comprennent le gaz et les billes de verre, alors que la phase continue implique de l'eau. L'approche eulérienne à deux et trois fluides est adoptée, résolvant les équations de quantité de mouvement pour chaque phase, couplée au modèle de bilan de population (PBM). Ce dernier consiste en différents modèles noyaux de coalescence et de rupture de bulles et prédit localement la taille des bulles, ce qui permet de calculer les transferts de forces interphase. Le transfert de quantité de mouvement comprend également les forces de trainé, de portance, de lubrification en proche parois et de dispersion par turbulence. Les contrainte dans la phase solide sont calculées à partir de la théorie cinétique des écoulements granulaires (KTGF) pour prédire localement la viscosité solide et la pression induite par le solide. Les conclusions clés suivantes sont tirées de ce travail:

- Les résultats montrent que les profils radiaux moyenné dans le temps pour la concentration de gaz, la vitesse axiale du liquide, la vitesse axiale solide et la rétention total du gaz utilisant la géométrie axisymétrique 2D prédisent une tendance similaire avec les données expérimentales. Cependant, à une vitesse superficielle plus élevée, on a observé un écart entre les simulations CFD et les expériences, qui est discuté plus loin.
- En écoulement bi-phasique, il est démontré que le noyau de coalescence Luo doit être réduit en combinaison avec le noyau de rupture Luo. Cette modification dans le noyau de coalescence Luo se fait par des fonctions définies par l'utilisateur et implémentées dans l'environnement logiciel Ansys-Fluent. Cependant, la combinaison des noyaux de coalescence Luo et de rupture Lehr (Luo-Lehr) ne nécessite pas de telles modifications. En outre, la combinaison des noyaux de coalescence Luo et de rupture Luo (Luo-Luo) sous-prédit la rétention de gaz par rapport aux noyaux Luo-Lehr avec les données empiriques.
- En écoulement triphasé, les deux combinaisons des noyaux Luo-Luo et Luo-Lehr prédisent correctement la vitesse solide axiale moyennée dans le temps par rapport aux valeurs

expérimentales. Cependant, la combinaison précédente sous-prédit souvent la rétention de gaz par rapport aux noyaux de Luo-Lehr avec les données empiriques. Cette tendance de la rétention du gaz dans un système triphasé est similaire au système à deux phases. Les deux combinaisons (noyaux Luo-Luo et Luo-Lehr) ne permettent pas de prédire la tendance correctement de la région entièrement développée à une vitesse superficielle élevée et avec un chargement solide par rapport aux données empiriques.

- Les résultats du banc d'essai montrent que sans tenir compte du terme de dispersion par turbulence, le comportement hydrodynamique de la colonne à bulles est loin des observations expérimentales. Tenir compte de ce terme se révèle significativement important dans le cas d'un diffuseur tubulaire en solo.

L'écart entre les simulations CFD et les expériences pourrait être lié aux raisons suivantes:

- Le modèle de turbulence k-ε est de nature isotrope, mais le système réel est généralement chaotique et anisotrope. Ce modèle fut à l'origine développé à partir des expériences en phase liquide. L'influence des phases dispersées sur le modèle de turbulence est ensuite introduite par les corrélations, qui est encore en phase de développement et il n'existe pas de modèle clair qui reflète correctement cette turbulence supplémentaire induite par les bulles et particules. En outre, le modèle de turbulence k-ε considère que le taux de dissipation d'énergie est une fonction seulement des tourbillons de petite taille et ignore l'influence des gros, d'où le taux de dissipation est sous-prédit. Cette valeur inférieure du taux de dissipation d'énergie affecte à la fois les noyaux de coalescence et de rupture.

- La fréquence de collision $\omega_C(d_i: d_j)$ du noyau de coalescence de bulle, voir l'équation 2-64 et la collision tourbillonnaire $\omega_B(d_i: d_j)$ du noyau de rupture de bulle, voir l'équation 2-75, sont directement proportionnelles au taux de dissipation d'énergie. Si le taux de dissipation d'énergie est sous-prédit, le taux de coalescence des bulles augmente et le taux de rupture des bulles diminue, ce qui favorise la formation de grandes bulles dans le système. En outre, les noyaux de coalescence et de rupture proposés sont fonction du paramètre de turbulence seulement et ignore le cisaillement visqueux, la stabilité interfaciale et les phénomènes de cisaillement, ce qui pourrait influencer les formations bulles. Enfin, ces noyaux ont été

développés à l'aide d'observations expérimentales d'écoulement biphasé et l'influence de la phase particulaire a été ignorée.

- La phénomène de transfert de quantité de mouvement interphasique n'est pas bien modélisé pour les systèmes à deux et trois phases. La pression hydrostatique diminue le long de la hauteur de la colonne, ce qui augmente le volume de la bulle montante. Ce comportement est ignoré dans tous les coefficients de traînée décrits précédemment. Généralement, l'influence de la pression sur les bulles montante est un paramètre ajusté avec des expériences utilisant une approche d'essai-erreur. Tout les coefficients de force de traînée solide-liquide précédemment discutés sont développés à partir de systèmes gaz-liquide ou gaz-solide et aucun n'est dérivé d'un système à suspension réelle. La forme des profils radiaux est influencée par le terme de dispersion par turbulence et dépend de la viscosité turbulente, qui est calculée à partir du modèle de turbulence k-ε.

Le travail futur comprend:

- Le modèle développé doit être testé à l'aide de l'approche des simulations des grandes échelles (LES, de l'anglais *Large-Eddy Simulation*) dans la géométrie 3D, en combinaison avec un model robuste et valide de turbulence induite par les bulles.
- De nouveaux noyaux de coalescence et de rupture de bulle sont nécessaires, qui devraient être développés à partir des données expérimentales triphasées qui fonctionnent dans le régime hétérogène.
- Un coefficient de trainé universelle pour les interactions gaz-liquide et liquide-solide est nécessaire, qui doit être testé dans une large gamme de conditions d'opération et de géométries avec des expériences. Généralement, dans la littérature, ce coefficient de traînée est souvent ajusté et validé avec les valeurs empiriques en utilisant une gamme étroite de vitesse superficielle.
- Le paramètres cinétiques et de transfert de chaleur/masse doivent être implanté dans le présent modèle développé et doivent être validés avec les valeurs empiriques.
- Il est nécessaire de tenter de simuler les réacteurs à bulles industriels et pilotes Enerkem (avec et sans composantes internes) afin de tester si le modèle développé pourrait prédire les

tendances correctement des profils radiaux moyennés dans le temps avec les données de l'échelle industrielle.

REFERENCES

Ansys, 2016a. *Ansys Fluent Theory Guide*, Technical Report, Canonsburg, USA.

Ansys, 2016b. *Ansys Fluent User's Guide*, Technical Report, Canonsburg, USA.

Antal, S.P., Lahey, R.T. & Flaherty, J.E., 1991. Analysis of phase distribution in fully developed laminar bubbly two-phase flow. *International Journal of Multiphase Flow*, 17(5), pp.635–652.

Arcuri, E.J., Slaff, G. & Greasham, R., 1982. Continuous production of thienamycin in immobilized cell systems. *Biotechnology and bioengineering*, 28(6), pp.842–849.

B.A, K. & W.b Vanderheyden, 1998. An extended k-epsilon turbulence model for multiphase flow. In *U.S. National Congress of Applied Mechanics*.

Bannari, R. et al., 2008. Three-dimensional mathematical modeling of dispersed two-phase flow using class method of population balance in bubble columns. *Computers and Chemical Engineering*, 32(12), pp.3224–3237.

Baten, J.M. van, 2000. *CFD: A design and scale-up tool for multiphase reactors*. Ph.D. Thesis, University of Amsterdam, Netherlands.

Bertodano., M.L. de, 1991. *Turbulent bubbly flow in a triangular duct*. Ph.D Thesis, Rensselaer Polytechnic Institute, Troy, USA.

Brennen, C., 2005. *Fundamentals of Multiphase Flows*, New York, USA: Cambridge University Press.

Brilman, W., Garcia Alba, L. & Veneman, R., 2013. Capturing atmospheric CO2 using supported amine sorbents for microalgae cultivation. *Biomass and Bioenergy*, 53, pp.39–47.

Bunner, B. & Tryggvason, G., 1999. Direct numerical simulations of three dimensional bubbly flows. *Physics of Fluids*, 11(8), pp.1967–1969.

Bunner, B. & Tryggvason, G., 2002. Dynamics of homogeneous bubbly flows Part 1. Rise velocity

and microstructure of the bubbles. *Journal of Fluid Mechanics*, 466(1), pp.17–52.

Burns, A.D. et al., 2004. The favre averaged drag model for turbulent dispersion in eulerian multi-phase flows. *Fifth International Conference on Multiphase Flow, ICMF, Yokohama, Japan, May 30- June 4*.

Buwa, V. V., Deo, D.S. & Ranade, V. V., 2006. Eulerian-Lagrangian simulations of unsteady gas-liquid flows in bubble columns. *International Journal of Multiphase Flow*, 32(7), pp.864–885.

Buwa, V. V. & Ranade, V. V., 2002. Dynamics of gas – liquid ow in a rectangular bubble column : experiments and single/multi-group CFD simulations. *Chemical Engineering Science*, 57, pp.4715–4736.

Chen, P., 2004. *Modeling the fluid dynamics of bubble column flows*. Ph.D. Thesis, Washington University, USA.

Chen, P., Sanyal, J. & Duduković, M.P., 2005. Numerical simulation of bubble columns flows: effect of different breakup and coalescence closures. *Chemical Engineering Science*, 60, pp.1085–1101.

Chesters, A.K., 1991. The modeling of coalescence processes in fluid–liquid dispersions. *Transactions of the Institution of Chemical Engineers*, 69, pp.259–270.

Chiesa, M. et al., 2005. Numerical simulation of particulate flow by the Eulerian-Lagrangian and the Eulerian-Eulerian approach with application to a fluidized bed. *Computers and Chemical Engineering*, 29(2), pp.291–304.

Choi, Y.D. & Chung, M.K., 1983. Analysis of turbulent gas-solid suspension flow in a pipe. *Journal of Fluids Engineering*, 105(5), pp.329–334.

Chung-Hur Lee, L.. E. and L.. G., 1987. Bubble breakup and coalescence in turbulent gas-liquid dispersions. *Chemical Engineering Communications*, 59(1–6), pp.65–84.

Deckwer, W.-D., 1992. *Bubble Column Reactors*, New York, USA: John Wiley and Sons.

Deen, N.G., van Sint Annaland, M. & Kuipers, J.A.M., 2004. Multi-scale modeling of dispersed gas-liquid two-phase flow. *Chemical Engineering Science*, 59(8–9), pp.1853–1861.

Degaleesan, S., 1997. *Fluid dynamic measurement and modeling of liquid mixing in bubble column*. Ph.D. Thesis, Washington University, USA.

Delnoij, E. et al., 1997. Dynamic simulation of dispersed gas-liquid two-phase flow using a discrete bubble model. *Chemical Engineering Science*, 52(9), pp.1429–1458.

Delnoij, E., Kuipers, J.A.M. & Swaaij, W.P.M. Van, 1999. A three-dimensional CFD model for gas-liquid bubble columns. *Chemical Engineering Science*, 54(13–14), pp.2217–2226.

Ding Jianmin & Gidaspow, D., 1990. A bubbling fluidization model using kinetic theory of granular flow. *American Institute of Chemical Engineers Journal*, 36(4), pp.523–538.

Ekambara, K., Dhotre, M.T. & Joshi, J.B., 2005. CFD simulations of bubble column reactors: 1D, 2D and 3D approach. *Chemical Engineering Science*, 60, pp.6733–6746.

Ekambara, K. & Joshi, J.B., 2005. Computational fluid dynamics simulations in bubble-column reactors: Laminar and transition regimes. *Industrial and Engineering Chemistry Research*, 44(5), pp.1413–1423.

Ellenberger, J. & Krishna, R., 1994. A unified approach to the scale-up of gas-solid fluidized bed and gas-liquid bubble column reactors. *Chemical Engineering Science*, 49(24, Part 2), pp.5391–5411.

Ergun, S., 1952. Fluid flow through packed columns. *Chemical Engineering Progress*, 48(2), pp.89–94.

Fan, L.-S., 1989. *Gas-Liquid-Solid Fluidization Engineering* H. Brener, ed., Stoneham, USA: Butterworth.

Fan, L.-S. et al., 1999. Some aspects of high-pressure phenomena of bubbles in liquids and liquid–solid suspensions. *Chemical Engineering Science*, 54, pp.4681–4709.

Fan, R., Marchisio, D.L. & Fox, R.O., 2004. Application of the direct quadrature method of moments to polydisperse gas-solid fluidized beds. *Powder Technology*, 139(1), pp.7–20.

Farouk, B. & Shah, Y.T., 1997. Hydrodynamic modeling of three-phase flows through a vertical column. *Chemical Engineering Science*, 52(24), pp.4485–4497.

Farzpourmachiani, A. et al., 2011. Eulerian-Lagrangian 3-D simulations of unsteady two-phase

gas-liquid flow in a rectangular column by considering bubble interactions. *International Journal of Non-Linear Mechanics*, 46(8), pp.1049–1056.

Fraga, B. et al., 2016. A LES-based Eulerian-Lagrangian approach to predict the dynamics of bubble plumes. *Ocean Modelling*, 97, pp.27–36.

Frank, T., Shi, J. & Burns, D., 2004. Validation of eulerian multiphase flow models for nuclear safety applications. *3rd International Symposium on Two-Phase Flow Modelling and Experimentation, Pisa, Italy, September 22-24*.

Fu, X.Y. & Ishii, M., 2002. Two-group interfacial area transport in vertical air-water flow I. Mechanistic model. *Nuclear Engineering and Design*, 219, pp.143–168.

Gamwo, I.K. et al., 2003. CFD models for methanol synthesis three-phase reactors: Reactor optimization. *Chemical Engineering Journal*, 93, pp.103–112.

Gamwo, I.K., Gidaspow, D. & Jung, J., 2005. Optimum catalyst size for slurry bubble column reactors. *Industrial and Engineering Chemistry Research*, 44(16), pp.6393–6402.

Gandhi, B., Prakash, A. & Bergougnou, M.A., 1999. Hydrodynamic behavior of slurry bubble column at high solids concentrations. *Powder Technology*, 103(2), pp.80–94.

Ge, W. & Li, J., 2002. Physical mapping of fluidization regimes—the EMMS approach. *Chemical Engineering Science*, 57(18), pp.3993–4004.

Gidaspow, D., Bezburuah, R. & Ding, J., 1992. Hydrodynamics of circulating fluidized beds, kinetic theory approach. In *Fluidization VII, Proceedings of the 7th Engineering Foundation Conference on Fluidization*. New York, USA, pp. 75–82.

Giorgio, B. et al., 2017. Computational Fluid-Dynamic modeling of the pseudo-homogeneous flow regime in large-scale bubble columns. *Chemical Engineering Science*, 160(May 2016), pp.144–160.

Grevskott, S. et al., 1996. Liquid circulation, bubble size distributions, and solids movement in two- and three-phase bubble columns. *Chemical Engineering Science*, 51(10), pp.1703–1713.

Heydorn, E.C., Diamond, B.W. & Lilly, R.D., 2003. *Commercial-scale demonstration of the liquid phase methanol (LPMEOH) process*, Technical Report, Allentown, USA.

Hills, J.H., 1974. Radial non-uniformity of velocity and voidage in a bubble column. *Transactions of the Institution of Chemical Engineers*, 52, pp.1–9.

Hooshyar, N. et al., 2013. Dynamics of single rising bubbles in neutrally buoyant liquid-solid suspensions. *Physical Review Letters*, 110(24), pp.1–5.

Hosokawa, S. et al., 2002. Lateral migration of single bubbles due to the presence of wall. *ASME 2002 Fluids Engineering Division Conference, Montreal, Canada, July 14-18*.

Howarth, W.J., 1964. Coalescence of drops in a turbulent flow field. *Chemical Engineering Science*, 19(1), pp.33–38.

Hu, G. & Celik, I., 2008. Eulerian-Lagrangian based large-eddy simulation of a partially aerated flat bubble column. *Chemical Engineering Science*, 63(1), pp.253–271.

Ishii, M. & Hibiki, T., 2011. *Thermo-Fluid Dynamics of Two-Phase Flow* Second., New York, USA: Springer Science and Business Media.

Ishii, M. & Zuber, N., 1979. Drag coefficient and relative velocity in bubbly, droplet or particulate flows. *American Institute of Chemical Engineers Journal*, 25(5), pp.843–855.

Jakobsen, H.., 2003. Numerical convection algorithms and their role in eulerian CFD reactor simulations. *International Journal of Chemical Engineering*, 1, pp.1–15.

Jakobsen, H.A., 2008. *Chemical Reactor Modeling* First., Berlin, Germany: Springer-Verlag.

Jakobsen, H.A., Lindborg, H. & Dorao, C.A., 2005. Modeling of bubble column reactors: Progress and limitations. *Industrial and Engineering Chemistry Research*, 44(14), pp.5107–5151.

Johnson, A.A. & Tezduyar, T.E., 1997. 3D simulation of fluid-particle interactions with the number of particles reaching 100. *Computer Methods in Applied Mechanics and Engineering*, 145, pp.301–321.

Joshi, J.B., 1980. Axial mixing in multiphase contactors - a unified correlation. *Transactions of the Institution of Chemical Engineers*, 55, pp.155–165.

Kitagawa, A., Murai, Y. & Yamamoto, F., 2001. Two-way coupling of Eulerian-Lagrangian model for dispersed multiphase flows using filtering functions. *International Journal of Multiphase Flow*, 27(12), pp.2129–2153.

Kocamustafaogullari, G. & Ishii, M., 1995. Foundation of the interfacial area transport equation and its closure relations. *International Journal of Heat and Mass Transfer*, 38(3), pp.481–493.

Koide, K. et al., 1968. Bubbles generated from porous plate. *Journal of Chemical Engineering of Japan*, 1(1), pp.51–56.

Krepper, E. et al., 2005. Inhomogeneous MUSIG Model - a Population Balance Approach for Polydispersed Bubbly Flows. In *Proceedings of the International Conference "Nuclear Energy for New Europe*. Bled, Slovenia, pp. 5–8.

Krepper, E. et al., 2008. The inhomogeneous MUSIG model for the simulation of polydispersed flows. *Nuclear Engineering and Design*, 238, pp.1690–1702.

Krishna, R. et al., 2001. Design and scale up of a bubble column slurry reactor for Fischer–Tropsch synthesis. *Chemical Engineering Science*, 56(2), pp.537–545.

Krishna, R. et al., 1999. Influence of scale on the hydrodynamics of bubble columns operating in the churn-turbulent regime: experiments vs. Eulerian simulations. *Chemical Engineering Science*, 54, pp.4903–4911.

Krishna, R., Van Baten, J.M. & Urseanu, M.I., 2000. Three-phase Eulerian simulations of bubble column reactors operating in the churn-turbulent regime: A scale up strategy. *Chemical Engineering Science*, 55(16), pp.3275–3286.

Kumar, A. et al., 1976. Bubble swarm characteristic in bubble column. *The Canadian Journal of Chemical Engineering*, 54, pp.503–508.

Kumar, S. & Ramkrishna, D., 1996. On the solution of population balance equations by discretization—I. A fixed pivot technique. *Chemical Engineering Science*, 51(8), pp.1311–1332.

Laborde-Boutet, C. et al., 2009. CFD simulation of bubble column flows: Investigations on turbulence models in RANS approach. *Chemical Engineering Science*, 64(21), pp.4399–4413.

Lahey, R.T., 1990. The analysis of phase separation and phase distribution phenomena using two-

fluid models. *Nuclear Engineering and Design*, 122, pp.17–40.

Lain, S. et al., 2002. Modelling hydrodynamics and turbulence in a bubble column using the Euler-Lagrange procedure. *International Journal of Multiphase Flow*, 28(8), pp.1381–1407.

Launder, B.E. & B. Spalding, D., 1974. The numerical computation of turbulent flows. *Computer Methods in Applied Mechanics and Engineering*, 3, pp.269–289.

Lee, D.. & Liang-Shin, F., 2002. Bubble column reactors. In S. Furusaki, J. Garside, & L.-S. Fan, eds. *The Expanding World of Chemical Engineering*. New York, USA: Taylor and Francis, pp. 157–184.

Lee, S., 1996. *Alternative fuels* First., Washington, USA: Taylor and Francis.

Lee, S., Speight, J.G. & Loyalka, S.K., 2007. *Handbook of alternative fuel technologies* First., Boca Raton, USA: Taylor and Francis Group.

Lehr, F., Millies, M. & Mewes, D., 2002. Bubble-Size distributions and flow fields in bubble columns. *American Institute of Chemical Engineers Journal*, 48(11), pp.2426–2443.

Li, J. et al., 1999. The EMMS model — its application, development and updated concepts. *Chemical Engineering Science*, 54(22), pp.5409–5425.

Li, W. & Zhong, W., 2015. CFD simulation of hydrodynamics of gas-liquid-solid three-phase bubble column. *Powder Technology*, 286, pp.766–788.

Liang-Shin, F. & Yang, G., 2003. Gas-liquid-solid three-phase fluidization. In *Handbook of Fluidization and Fluid-Particle Systems*. pp. 765–810.

Liao, Y. & Lucas, D., 2009. A literature review of theoretical models for drop and bubble breakup in turbulent dispersions. *Chemical Engineering Science*, 64(15), pp.3389–3406.

Liao, Y. & Lucas, D., 2010. A literature review on mechanisms and models for the coalescence process of fluid particles. *Chemical Engineering Science*, 65(10), pp.2851–2864.

Liu, K., Song, C. & Subramani, V., 2010. *Hydrogen and syngas production and purification technologies*, Hoboken, USA: John Wiley and Sons.

Liu, Y. & Hinrichsen, O., 2014. Study on CFD-PBM turbulence closures based on k-ε and

Reynolds stress models for heterogeneous bubble column flows. *Computers and Fluids*, 105, pp.91–100.

Lucas, D., Krepper, E. & Prasser, H.M., 2005. Development of co-current air-water flow in a vertical pipe. *International Journal of Multiphase Flow*, 31(12), pp.1304–1328.

Lucas, D., Krepper, E. & Prasser, H.M., 2007. Use of models for lift, wall and turbulent dispersion forces acting on bubbles for poly-disperse flows. *Chemical Engineering Science*, 62(15), pp.4146–4157.

Lun, C.K.K. et al., 1984. Kinetic theories for granular flow: Inelastic particles in couette flow and slightly inelastic particles in a general flow field. *Journal of Fluid Mechanics*, 140(223–256).

Luo, H., 1993. *Coalescence, breakup and liquid circulation in bubble column reactors*. Ph.D. Thesis, Norwegian University of Science and Technology, Trondheim, Norway.

Luo, H. & Svendsen, H.F., 1996. Theoretical model for drop and bubble breakup in turbulent dispersions. *American Institute of Chemical Engineers Journal*, 42(5), pp.1225–1233.

Malalasekera, W. & Versteeg, H.K., 1995. *An introduction to computational fluid dynamics: The finite volume method* First., London, UK: Longman Scientific and Technical.

Martinez-Bazan, Montanes, J.L. & Lasheras, J.C., 1999a. On the breakup of an air bubble injected into a fully developed turbulent flow. Part 1: Breakup frequency. *Journal of Fluid Mechanics*, 401, pp.157–182.

Martinez-Bazan, Montanes, J.L. & Lasheras, J.C., 1999b. On the breakup of an air bubble injected into a fully developed turbulent flow. Part 2. Size PDF of the resulting daughter bubbles. *Journal of Fluid Mechanics*, 401, pp.183–207.

Martinez-Bazan, Montanes, J.L. & Lasheras, J.C., 1999c. On the breakup of an air bubble injected intoa fully developed turbulent flow. Part 2. Size PDF of the resulting daughter bubbles. *Journal of Fluid Mechanics*, 401, pp.183–207.

Masood, R.M.A. & Delgado, A., 2014. Numerical investigation of the interphase forces and turbulence closure in 3D square bubble columns. *Chemical Engineering Science*, 108, pp.154–168.

Matonis, D., Gidaspow, D. & Bahary, M., 2002. CFD simulation of flow and turbulence in a slurry bubble column. *American Institute of Chemical Engineers Journal*, 48(7), pp.1413–1429.

Mattson, M.D. & Mahesh, K., 2012. A one-way coupled, Euler-Lagrangian simulation of bubble coalescence in a turbulent pipe flow. *International Journal of Multiphase Flow*, 40, pp.68–82.

McGraw, R., 1997. Description of aerosol dynamics by the quadrature method of moments. *Aerosol Science and Technology*, 27(2), pp.255–265.

Michele, V. & Hempel, D.C., 2002. Liquid flow and phase holdup - Measurement and CFD modeling for two-and three-phase bubble columns. *Chemical Engineering Science*, 57(11), pp.1899–1908.

Morsi, S.. & Alexander, A.., 1972. An investigation of particle trajectories in two-phase flow system. *Journal of Fluid Mechanics*, 55(2), pp.325–332.

Ojima, S., Hayashi, K. & Tomiyama, A., 2014. Effects of hydrophilic particles on bubbly flow in slurry bubble column. *International Journal of Multiphase Flow*, 58, pp.154–167.

Olah, G.A., 2005. Beyond oil and gas: The methanol economy. *Angewandte Chemie International Edition*, 44(18), pp.2636–2639.

Olah, G.A., Goeppert, A. & Prakash, G.K.S., 2009. *Beyond oil and gas: The methanol economy* Second., Weinheim, Germany: Wiley-VCH.

Olmos, E. et al., 2001. Numerical simulation of multiphase flow in bubble column reactors. Influence of bubble coalescence and break-up. *Chemical Engineering Science*, 56(21–22), pp.6359–6365.

Panneerselvam, R., Savithri, S. & Surender, G.D., 2009. CFD simulation of hydrodynamics of gas-liquid-solid fluidised bed reactor. *Chemical Engineering Science*, 64(6), pp.1119–1135.

Pfleger, D. et al., 1999. Hydrodynamic simulations of laboratory scale bubble columns fundamental studies of the Eulerian-Eulerian modelling approach. *Chemical Engineering Science*, 54(21), pp.5091–5099.

Pfleger, D. & Becker, S., 2001. Modelling and simulation of the dynamic flow behaviour in a

bubble column. *Chemical Engineering Science*, 56, pp.1737–1747.

Prince, M.J. & Blanch, H.W., 1990. Bubble coalescence and break-up in air-sparged bubble columns. *American Institute of Chemical Engineers Journal*, 36(10), pp.1485–1499.

Rabha, S., Schubert, M., Wagner, M., et al., 2013. Bubble Size and Radial Gas Hold-Up Distributions in a Slurry Bubble Column Using Ultrafast Electron Beam X-Ray Tomography. *American Institute of Chemical Engineers Journal*, 59(5), pp.1709–1722.

Rabha, S., Schubert, M. & Hampel, U., 2013. Intrinsic flow behavior in a slurry bubble column: A study on the effect of particle size. *Chemical Engineering Science*, 93, pp.401–411.

Ramkrishna, D., 2000. *Population balances theory and application to particulate systems in engineering*, San Diego, USA: Academic Press.

Rampure, M.R., Buwa, V. V & Ranade, V. V, 2003. Modelling of gas-liquid/gas-liquid-solid flows in bubble columns: Experiments and CFD simulations. *The Canadian Journal of Chemical Engineering*, 81(August), pp.692–706.

Rzehak, R. et al., 2017. Unified modeling of bubbly flows in pipes, bubble columns, and airlift columns. *Chemical Engineering Science*, 157, pp.147–158.

Sada, E., Kumazawa, H. & C.H. Lee, 1986. Influences of suspended fine particles on gas holdup and mass transfer characteristics in a slurry bubble column. *American Institute of Chemical Engineers Journal*, 32, pp.853–856.

Safoniuk, M. et al., 1999. Use of dimensional similitude for scale-up of hydrodynamics in three-phase fluidized beds. *Chemical Engineering Science*, 54(21), pp.4961–4966.

Sannaes, B.., 1997. *Solid movement and concentration profiles in slurry reactors*. Ph.D. Thesis, Norwegian University of Science and Technology, Trondheim, Norway.

Sato, Y. & Sekogushi, K., 1975. Liquid velocity distribution in two-phase bubbly flow. *International Journal of Multiphase Flow*, 2, pp.79–95.

Saxena, S.C. & Z. D. Chen, 1994. Hydrodynamics and heat transfer of baffled and unbaffled bubble. *Reviews in Chemical Engineering*, 10, pp.319–400.

Scardovelli, R. & Zaleski, S., 1999. Direct numerical simulation of free-surface and interfacial

flow. *Annual Review of Fluid Mechanics*, 31(1), pp.567–603.

Schaefer, D.G., 1987. Instability in the evolution equations describing incompressible granular flow. *Journal of Differential Equations*, 66(1), pp.19–50.

Schallenberg, J., Enß, J.H. & Hempel, D.C., 2005. The important role of local dispersed phase hold-ups for the calculation of three-phase bubble columns. *Chemical Engineering Science*, 60(22), pp.6027–6033.

Schiller, L. & Naumann, Z., 1933. Über die grundlegenden Berechungen bei der Schwerkraft-aufbereitungitle. *Zeitschrift des Vereiner der Deutscheutschen Ingenieur*, 77, pp.318–320.

Selma, B., Bannari, R. & Proulx, P., 2010. Simulation of bubbly flows: Comparison between direct quadrature method of moments (DQMOM) and method of classes (CM). *Chemical Engineering Science*, 65(6), pp.1925–1941.

Shah, Y.T. et al., 1982. Design parameters estimations for bubble column reactors. *American Institute of Chemical Engineers Journal*, 28(3), pp.353–379.

Shaikh, A. & Al-Dahhan, M., 2013. Scale-up of bubble column reactors: A review of current state-of-the-art. *Industrial and Engineering Chemistry Research*, 52(24), pp.8091–8108.

Simon, C.A., 2007. *Alternative energy: Political, economic, and social feasibility* First., Lanham, USA: Rowman and Littlefield.

Simonin, O. & Viollet, P.L., 1990. Modeling of turbulent two-phase jets loaded with discrete particles. *Phenomena in Multiphase Flows*, pp.259–269.

Smith, J.S., Valsaraj, K.T. & Thibodeaux, L.J., 1996. Bubble column reactors for wastewater treatment. 1. Theory and modeling of continuous countercurrent solvent sublation. *Industrial and Engineering Chemistry Research*, 35(5), pp.1688–1699.

Smith, M. & Matsoukas, T., 1998. Constant-number Monte Carlo simulation of population balances. *Chemical Engineering Science*, 53(9), pp.1777–1786.

Soo, S.L., 1990. *Multiphase Fluid Dynamics*, Beijing, China: Science Press and Gover Technical.

Sungkorn, R., Derksen, J.J. & Khinast, J.G., 2011. Modeling of turbulent gas-liquid bubbly flows using stochastic Lagrangian model and lattice-Boltzmann scheme. *Chemical Engineering*

Science, 66(12), pp.2745–2757.

Swart, J.W.A. De, Vliet, R.E. Van & Krishna, R., 1996. Size, structure and dynamics of "large" bubbles in a two-dimensional slurry bubble column. *Chemical Engineering Science*, 51, pp.4619–4629.

Syamlal, M., 1985. *Multiphase hydrodynamics of gas-solid flows*. Ph.D. Thesis, Illinois Institute of Technology, Chicago, USA.

Syamlal, M., Rogers, W. & O'Brian, T.J., 1993. *MFIX Documentation theory guide*, Technical Report, Morgantown, USA.

Thomas, D.G., 1965. Transport characteristics of suspension: VIII. A note on the viscosity of Newtonian suspensions of uniform spherical particles. *Journal of Colloid Science*, 20(3), pp.267–277.

Tomiyama, A. et al., 1995. A simple numerical method for solving an incompressible two-fluid model in a general curvilinear coordinate system. *Amsterdam society of petroleum engineers*, pp.241–252.

Tomiyama, A., 2004. Drag, lift and virtual mass forces acting on a single bubble. In *3rd, International symposium on two-phase flow modelling and experimentation*. Pisa, Italy.

Tomiyama, A., 1998. Struggle with computational bubble dynamics. *Third International Conference on Multiphase Flow, Lyon, France*, June 8-12.

Troshko, A.A. & Hassan, Y.A., 2001. A two-equation turbulence model of turbulent bubbly flows. *International Journal of Multiphase Flow*, 27(11), pp.1965–2000.

Troshko, A.A. & Zdravistch, F., 2009. CFD modeling of slurry bubble column reactors for Fisher-Tropsch synthesis. *Chemical Engineering Science*, 64(5), pp.892–903.

Tryggvason, G. et al., 2006. Direct numerical simulations of gas/liquid multiphase flows. *Fluid Dynamics Research*, 38(9), pp.660–681.

Wang, Q. & Yao, W., 2016. Computation and validation of the interphase force models for bubbly flow. *International Journal of Heat and Mass Transfer*, 98, pp.799–813.

Wang, T., Wang, J. & Jin, Y., 2006. A CFD-PBM coupled model for gas-liquid flows. *American*

Institute of Chemical Engineers Journal, 52(1), pp.125–140.

Wang, T., Wang, J. & Jin, Y., 2003. A novel theoretical breakup kernel function for bubbles/droplets in a turbulent flow. *Chemical Engineering Science*, 58(20), pp.4629–4637.

Wang, T., Wang, J. & Jin, Y., 2005. Population balance model for gas-liquid flows: Influence of bubble coalescence and breakup models. *Industrial and Engineering Chemistry Research*, 44(19), pp.7540–7549.

Wen, C.Y. & Yu, Y.H., 1966. Mechanics of fluidization. *The Chemical Engineering Progress Symposium Series*, 62, pp.100–111.

Wender, I., 1996. Reactions of synthesis gas. *Fuel Processing Technology*, 48(3), pp.189–297.

Wiemann, D. & Mewes, D., 2005. Calculation of flow fields in two and three-phase bubble columns considering mass transfer. *Chemical Engineering Science*, 60, pp.6085–6093.

Wilkinson, P.M., 1991. *Physical aspects and scale-up of high pressure bubble columns*. Ph.D. Thesis, University of Groningen, Netherlands.

Wu, Q., Kim, S. & Ishii, M., 1998. One-group interfacial area transport in vertical bubbly flow. *International Journal of Heat and Mass Transfer*, 41(8–9), pp.1103–1112.

Xu, L. et al., 2014. Application of Population Balance Model in the Simulation of Slurry Bubble Column. *Industrial and Engineering Chemistry Research*, 53(12), pp.4922–4930.

Xu, L. et al., 2013. Numerical Simulation of Bubble Column Flows in Churn-Turbulent Regime: Comparison of Bubble Size Models. *Industrial and Engineering Chemistry Research*, 52(20), pp.6794–6802.

Yamoah, S. et al., 2015. Numerical investigation of models for drag, lift, wall lubrication and turbulent dispersion forces for the simulation of gas-liquid two-phase flow. *Chemical Engineering Research and Design*, 98, pp.17–35.

Yang, N. et al., 2007. Explorations on the multi-scale flow structure and stability condition in bubble columns. *Chemical Engineering Science*, 62(24), pp.6978–6991.

Yang, W.-C., 2003. *Handbook of Fluidization and Fluid-Particle Systems*, New York, USA: Marcel Dekker Inc.

Ye-Mon Chen & Liang-Shin, F., 1989. Bubble breakage mechanisms due to collision with a particle in liquid medium. *Chemical Engineering Science*, 44(1), pp.117–132.

Yeoh, G.H., Cheung, D.C.P. & Tu, J., 2014. *Multiphase Flow Analysis Using Population Balance Modeling*, Oxford, UK: Butterworth-Heinemann.

Yuan, C., Laurent, F. & Fox, R.O., 2012. An extended quadrature method of moments for population balance equations. *Journal of Aerosol Science*, 51, pp.1–23.

Zhang, D., Deen, N.G. & Kuipers, J.A.M., 2005. Numerical simulation of dynamic flow behavior in a bubble column: Comparison of the bubble-induced turbulence models in the k - ε model. *Fourth International Conference on CFD in the Oil and Gas, Metallurgical and Process Industries*, (June), pp.1–9.

Zhang, D., Deen, N.G. & Kuipers, J.A.M., 2006. Numerical simulation of the dynamic flow behavior in a bubble column: A study of closures for turbulence and interface forces. *Chemical Engineering Science*, 61(23), pp.7593–7608.

Zhang, X. & Ahmadi, G., 2005. Eulerian-Lagrangian simulations of liquid-gas-solid flows in three-phase slurry reactors. *Chemical Engineering Science*, 60(18), pp.5089–5104.

Zhou, R., Yang, N. & Li, J., 2017. CFD simulation of gas-liquid-solid flow in slurry bubble columns with EMMS drag model. *Powder Technology*, 314, pp.466–479.

Zhu, Z. et al., 2009. On the coupled solution of a combined population balance model using the least-squares spectral element method. *Industrial and Engineering Chemistry Research*, 48(17), pp.7994–8006.

Zun, I., 1980. Transverse migration of bubbles influenced by walls in vertical bubbly flow. *International Journal of Multiphase Flow*, 6, pp.583–588.